Faculteit Industriële Ingenieurswetenschappen

master in de industriële wetenschappen: nucleaire technologie

Masterthesis

Gamma-ray spectrometry: Development, testing and validation of computer models by using the simulation package EGSnrc

Lander Poppe

Scriptie ingediend tot het behalen van de graad van master in de industriële wetenschappen: nucleaire technologie, afstudeerrichting nucleair en medisch

PROMOTOR :
Prof. dr. Wouter SCHROEYERS

PROMOTOR :
Dr. Mikael HULT

COPROMOTOR :
Dhr. Gerd MARISSENS
Dhr. Heiko STROH

Gezamenlijke opleiding UHasselt en KU Leuven

Universiteit Hasselt | Campus Diepenbeek | Faculteit Industriële Ingenieurswetenschappen | Agoralaan Gebouw H - Gebouw B | BE 3590 Diepenbeek

Universiteit Hasselt | Campus Diepenbeek | Agoralaan Gebouw D | BE 3590 Diepenbeek
Universiteit Hasselt | Campus Hasselt | Martelarenlaan 42 | BE 3500 Hasselt

2022
2023

Faculteit Industriële Ingenieurswetenschappen

master in de industriële wetenschappen: nucleaire technologie

Masterthesis

Gamma-ray spectrometry: Development, testing and validation of computer models by using the simulation package EGSnrc

Lander Poppe

Scriptie ingediend tot het behalen van de graad van master in de industriële wetenschappen: nucleaire technologie, afstudeerrichting nucleair en medisch

PROMOTOR :
Prof. dr. Wouter SCHROEYERS

PROMOTOR :
Dr. Mikael HULT

COPROMOTOR :
Dhr. Gerd MARISSENS
Dhr. Heiko STROH

UHASSELT KU LEUVEN

Acknowledgments

First of all, I would like to express my deepest gratitude towards my mentor dr. Mikael Hult for the continuous guidance, expertise, enthusiasm and of course the many fun facts you happily shared with me. On top of everything you helped me with, you are a genuinely warm person and I could not have wished for a better mentor during my stay at the JRC. I would also like to take this opportunity to thank my internal supervisor prof. dr. Wouter Schroeyers for providing me with lots of valuable information and well-appreciated feedback.

Next, I would like to thank everyone that I came in contact with during my stay at the JRC. I truly enjoyed working in this friendly, amusing, yet very professional work environment and that is to the credit of all of you. Gerd and Heiko, thanks a lot for everything you did for me! Whenever I had a question, you were always prepared to take action. Without your help I would not have been able to deliver this thesis. You are both very amusing people and made me feel very welcome when I first arrived at the JRC. I wish you all the best! Raf, thank you! Not only for all the support, professional advice (and crash course in Word) you provided me with, but also for the many enjoyable conversations we had. You are a fantastic guy and I wish you all the best with your work, personal live and cycling challenges (at this pace, I will see you riding the Tour de France soon!). Linde, thanks a lot for all the support, special tips and of course the numerous pleasant conversations. Never doubt yourself, you are a wonderful person and I wish you all the best with the continuation of your PhD. Jan, despite not having been able to share more time with you, you are a great person and your amusing remarks (or telephone sounds) always uplifted the mood in the room. Petya, in the short time we met I could tell you are a very sweet and caring person! I wish you all the best. Stefaan and Krzysztof, thank you both for helping me whenever I was stuck and for broadening my view by sharing life experiences or by giving me a tour through your working field. You are both very smart people far beyond your working field.

I can only hope to have such great friends/colleagues like all of you in my next challenge.

Finally, I would like to thank my family and friends for helping me grow to the person I am today. You supported me not only throughout my studies but during my whole life and I cannot thank you enough for that. Herewith, I would specifically like to show my deepest gratitude towards my loving parents, brother and Willy. Thank you so much for everything you have done for me! From giving live advice, providing me with distraction when I most needed it, helping out with daily tasks, to even keeping me from forgetting things… Nothing was ever too much for you and thus from the bottom of my heart, thank you for everything! You all mean so much to me and I feel truly blessed having you in my life.

Table of contents

List of Tables

List of Figures

List of symbols

(1) $$E_\gamma = E_{\gamma 0}\left[1 + \frac{E_{\gamma 0}}{m_0 c^2}(1 - \cos\theta)\right]^{-1}$$

- E_Y: Energy of the scattered photon
- E_{Y0}: Energy of the incoming photon
- m_0c^2: Rest mass energy
- θ: Scattering angle

(2) $$n_i = A \cdot T^{3/2} \cdot e^{-\frac{E_g}{2kT}}$$

- n_i: The number of electron-hole-pairs at thermal equilibrium
- A: Material constant
- T: Temperature in Kelvin
- E_g: The Bandgap (at 0 K)
- k: Boltzmann constant (8.617 * 10^{-5} eV/K)

(3) $$A = \frac{C_{TOT} - C_{Peak}^{Bkg} - C_{Continuum}}{\varepsilon_{REF}^{Exp}\frac{\varepsilon_{Sample}^{MC}}{\varepsilon_{REF}^{MC}} P_\gamma} e^{\lambda t_d} \frac{\lambda}{(1 - e^{-\lambda t_m})} K_1 K_2 K_3$$

- A: Activity of radionuclide
- $C_{TOT} – C^{Bkg}_{Peak} – C_{Continuum}$: counts under peak
- ε^{Exp}_{REF}: Experimental efficiency of reference source
- $\varepsilon^{MC}_{Sample} / \varepsilon^{MC}_{REF}$: Correction factor from MC calculation
- λ: Decay constant
- t_d: Decay time (to a reference date)
- t_m: Measurement live time
- K_1: Summing correction / K_2: Branching correction / K_3: Equilibrium correction
- P_Y: Gamma-ray emission probability

(4) $$\varepsilon = \frac{C}{A * t * P}$$

- ε: Full Energy Peak efficiency
- c: Counts in the spectra under the gamma-peak of the radionuclide
- A: Activity of the concerning source
- t: Measurement time
- P_Y: Gamma-ray emission intensity

(5) $\varepsilon_{sample} = \varepsilon^{exp}_{ref} = (\varepsilon^{MC}_{sample} / \varepsilon^{MC}_{ref})$

- ε_{sample}: Efficiency of sample measurement
- ε^{exp}_{ref}: Experimental efficiency of reference source measurement
- $\varepsilon^{MC}_{sample}$: MC efficiency of sample measurement
- ε^{MC}_{ref}: MC efficiency of reference source measurement

Abstract

High Purity Germanium (HPGe) detectors are used in gamma-ray spectrometry for analysing samples containing gamma-ray emitting radionuclides. To calculate the activities (in Bq) from measured samples, calibration of the Full Energy Peak (FEP) efficiency of the HPGe detector is necessary. Therefore, the efficiency transfer method is used, which is based upon a computer model of the detector. This thesis aims to optimise and validate the computer models of a coaxial HPGe detector, the Ge-T10, and an HPGe well-detector, the Ge14.

To optimise and validate computer models of both detectors, calibration sources are measured to acquire experimental data of the efficiency at different energies. The same radionuclides and FEPs are then simulated using the model. To minimise the difference between the model and experimental data, the model is adjusted by varying four parameters: crystal position, thickness of the endcap, and thickness of the top and side deadlayer. The optimised model is then validated at three different source-detector distances and for four volume sources.

An optimised and validated model for both detectors was constructed and can be used for sample analysis. The results show that the optimal starting point for an efficiency calibration is at higher source-detector distance in order to minimise the impact of factors such as bad alignment, incorrect coincidence correction, etc. Finally, the validated model of the Ge-14 detector was used to determine the distribution of radiocaesium in the organs of large wild mammals.

Abstract (in Dutch)

Hoogzuivergermaniumdetectoren (HPGe) worden gebruikt in gammaspectrometrie voor het analyseren van stalen die gammastralen uitzenden. Om de activiteiten van gemeten stalen te berekenen, is er kalibratie van de FEP-efficiëntie (Full Energy Peak) van de HPGe-detector nodig. Hiervoor wordt gebruik gemaakt van de efficiëntieoverdrachtsmethode, die gebaseerd is op een computermodel van de detector. Deze thesis optimaliseert en valideert de computermodellen van één coaxiale HPGe-detector, de Ge-T10, en één HPGe-well-detector, de Ge14.

Kalibratiebronnen worden gemeten om experimentele gegevens over de efficiëntie te verkrijgen. Dezelfde radionucliden en FEP's worden vervolgens gesimuleerd met het computermodel. Om het verschil tussen het model en de experimentele data te minimaliseren wordt het model aangepast door vier parameters te laten variëren: kristalpositie, dikte van de eindkap en dikte van de bovenste en laterale dode laag. Het geoptimaliseerde model wordt vervolgens gevalideerd op drie verschillende afstanden en voor vier volumebronnen.

Een geoptimaliseerd en gevalideerd model voor beide detectoren is geconstrueerd en kan gebruikt worden voor stalenanalyse. Uit de resultaten blijkt dat een efficiëntiekalibratie het best start bij een hogere bron-detectorafstand om de invloed van factoren zoals een slechte uitlijning van de bron, onjuiste coïncidentiecorrectie, enz. te minimaliseren. Het gevalideerde Ge14-model werd ten slotte gebruikt om de distributie van radiocaesium in de organen van grote wilde zoogdieren te bepalen.

1 Introduction

In March 1957, the Euratom treaty was signed which regulates the cooperation between the different Member States of the European Union (EU) in order to ensure a peaceful use of nuclear energy. The Joint Research Centre (JRC), set up under Article 8 of the Euratom Treaty, is the science and knowledge service of the European Commission (EC), which provides independent scientific advice and support to EU policy. It consists of different facilities spread across different EU countries each with a specific purpose. One of them is the JRC facility in Geel, JRC-Geel, which was founded in 1960. It brings together multi-disciplinary expertise for developing and testing new measurement methods, production of reference materials and promoting standardisation and harmonisation across the European Union with the ultimate goal to stimulate innovation and to protect consumers and citizens [1].

The RadioNuclide metrology team (RN) of JRC-Geel is responsible for establishing international equivalence for radioactivity measurements and verifying the quality of measurements performed in the member states radioactivity monitoring laboratories. For this purpose, it operates numerous instruments for measuring radioactivity in a wide range of different materials. The most common laboratory technique used for analysing samples containing gamma-ray emitting radionuclides in any radiometric laboratory is called gamma-ray spectrometry. The key instruments are the High Purity Germanium (HPGe) detectors because of their exceptional resolution. The RN operates 10 such detectors in the above ground laboratory called RADMET located on the site of JRC-Geel. In addition, the RN rents a space in the underground research facility HADES, located at the site of SCK CEN in Mol, where another 10 HPGe-detectors are in operation. The JRC lab is located in HADES to minimise the amount of background radiation induced by cosmic rays. These circumstances made it possible to carry out specialised research applications in a wide range of scientific fields [1], [2].

Before applying gamma-ray spectrometry to various projects it is important to calibrate the Full Energy Peak (FEP) efficiency of the HPGe detector used. This allows the operator to evaluate the radioactivity of unknown samples correctly. The efficiency transfer method is the most accurate method to determine FEP efficiency. Besides experimental reference source measurements, computer simulations are required to employ the efficiency transfer method. Therefore, an optimised and validated computer model is developed for each detector. The optimal model is developed comparing measured and simulated FEP efficiencies of reference sources and adjusting different dimensions of the detector in the model until a good agreement is reached [3].

This Master Thesis aims to optimise and validate the computer models of one detector located in the above ground (RADMET) lab, the Ge-T10 detector and one in the underground research facility HADES, the Ge14 detector.

The optimised and validated model for the Ge14 will thereafter be used in an application project (Named ROWAN) linked to determining the distribution of radiocaesium in large wild mammals (wolves and bears) in collaboration with the Ruder Boskovic institute in Zagreb, Croatia. The project stems from the recommendations in ICRP (International Commission on Radiological Protection) document 103 that calls for studies to better understand the dose-effect relations in flora and fauna. These recommendations have influenced the new Basic Safety Standards from 2013 (Council Directive 2013/59 EURATOM) that highlights the need for radioprotection of the environment. There is very little data on how anthropogenic radionuclides distribute inside large mammals, which the ROWAN project seeks to address. The use of detector Ge-14 is essential as the samples are small and the activities very low.

The Ge-T10 model will then be used to create simulated spectra of samples for nuclear decommissioning with a specific radionuclide vector. That work will be performed in collaboration with the nuclear energy operator Engie.

2 JRC: organisation and infrastructure

This chapter gives a general introduction about the JRC and certain assets important to situate the topic of this thesis.

In March 1957, the Euratom treaty was signed which regulates the cooperation between the different Member States of the European Union (EU) in order to ensure a peaceful use of nuclear energy. The Joint Research Centre (JRC), set up under Article 8 of the Euratom Treaty, is the science and knowledge service of the European Commission (EC), which provides independent scientific advice and support to EU policy. It consists of different facilities spread across different EU countries each with a specific purpose. One of them is the JRC facility in Geel, JRC-Geel, which was founded in 1960. It brings together multi-disciplinary expertise for developing and testing new measurement methods, production of reference materials and promoting standardisation and harmonisation across the European Union with the ultimate goal to stimulate innovation and to protect consumers and citizens

2.1 RadioNuclide metrology (RN) team

The RadioNuclide metrology team (RN) of JRC-Geel is responsible for establishing international equivalence for radioactivity measurements and verifying the quality of measurements performed in the member states' radioactivity monitoring laboratories. For this purpose, it operates numerous instruments for measuring radioactivity in a wide range of different materials. The most common laboratory technique used for analysing samples containing gamma-ray emitting radionuclides in any radiometric laboratory is called gamma-ray spectrometry. The key instruments are the High Purity Germanium (HPGe) detectors because of their exceptional resolution. The RN operates 10 such detectors in the above ground laboratory called RADMET located on the site of JRC-Geel. In addition, the RN rents a space in the underground research facility HADES, located at the site of SCK CEN in Mol, where another 10 HPGe-detectors are in operation [1], [2].

2.1.1 The HADES underground research facility and the JRC low-level laboratory

a) Waste management

Nuclear waste is defined as any waste (whatever its physical form (gaseous, liquid, solid)), remaining from any practice or intervention, that contains, or is contaminated with, radionuclides at concentrations or activities greater than clearance levels established by the regulatory body. These clearance levels depend on the type of radionuclide, its chemical form and the application or circumstances it is active in. Nuclear waste is divided into different categories depending on their activity and half-life time. In figure 1, the classification of radioactive waste (RAW) in Belgium is presented (differs from the IAEA classification) [4].

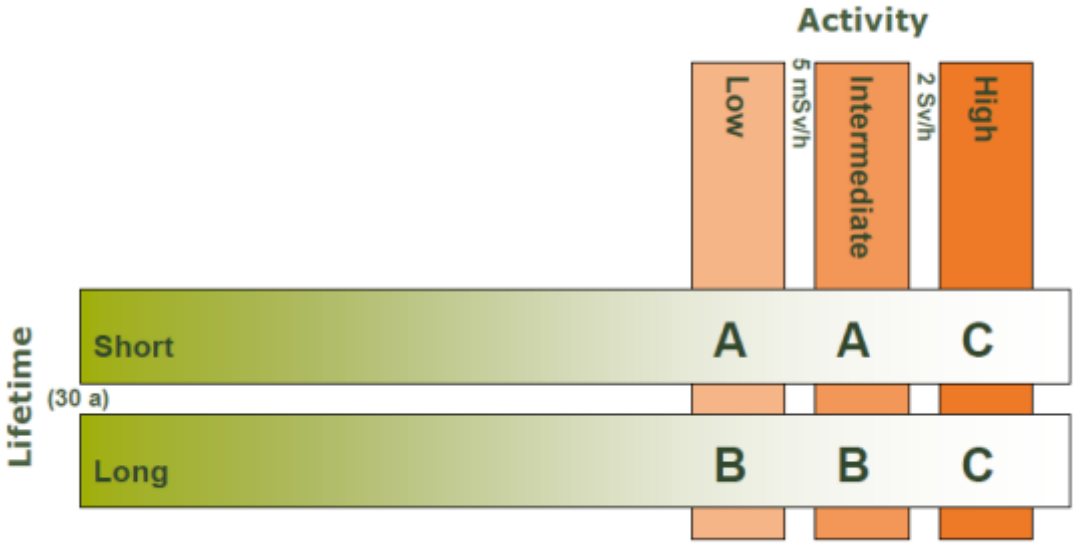

Figure 1: National classification of nuclear waste [4, p. 226]

The Low level radioactive material will be stored in the future surface storage in Dessel. Since the contents of the category B and C are higher in activity and half-life time compared to contents of category A, the three parameters (containment, isolation and multiple safety barriers) are fulfilled in other, stricter ways. This results in the concept of deep geological disposal (following the IAEA definition: a disposal is 'the emplacement of radioactive waste into a facility or location with no intention of retrieving the waste') for category B and C. In Belgium, The probable option of disposal in the 'Boomse klei lagen' is being investigated by the Euridice research project at the underground research facility HADES in Mol. HADES is situated at a depth of 225m and was created in order to develop and study methods for geological disposal of radioactive waste. A view in one of the access paths to Hades is given in figure 2. Different materials and building techniques were used to reach such depths and to build a tunnel structure, mimicking a future disposal facility. It offers the opportunity to investigate the differences in difficulty, cost price and disposal capacities of the different techniques and materials used [2], [4].

Figure 2: The way to HADES: Looking down shaft 2 [2, p.12]

b) JRC practices in HADES

To study all variables, techniques and material properties for the final geological disposal of the category B and C nuclear waste, the HADES research facility is situated at a depth of 225 m underground. These special circumstances create opportunities for the exploitation of alternative research practices (which rely on being so deep underground). The Joint Research Centre at Geel (JRC-Geel) operates a laboratory for low-background gamma-ray spectrometry and testing. The foundation for the international activities of JRC-Geel in Hades is the Euratom Treaty, signed in 1957. The JRC's lab (shown in figure 3) is located underground in HADES to minimise the amount of background radiation induced by cosmic rays. Compared with above-ground radioactivity measurements, the instrumental background count-rate is extremely low, in some cases representing as little as 0.02% of the normal reading above ground. These circumstances have made it possible to carry out specialised research in a wide range of projects spread over different scientific research areas, a few of which are: Tracer studies by using emissions from Fukushima to trace currents in the Pacific Ocean, determining the nature of the neutrino, neutron cross-section measurements, etc. [2], [5], [6].

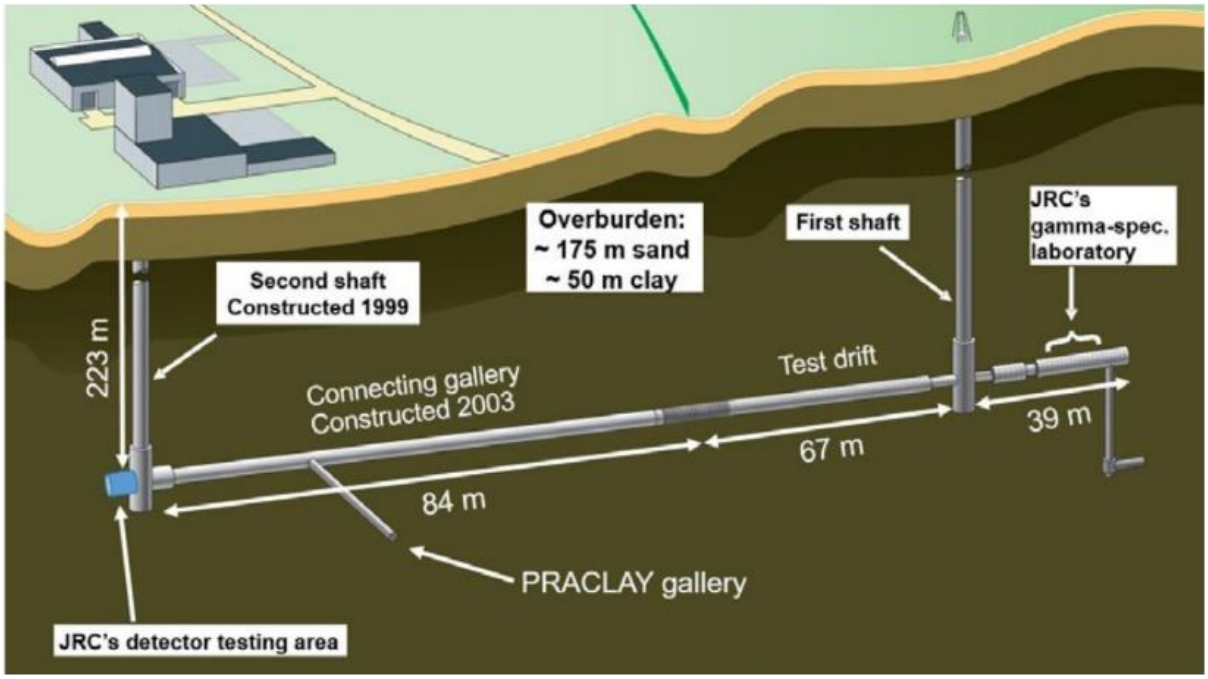

Figure 3: Schematic view of the HADES Underground Research Facility [2, p. 16]

c) Impact on gamma-ray spectrometry

Gamma-ray spectrometry is the most frequently used analytical method in radiometric laboratories today. At present, the radioactive laboratory that JRC-Geel operates inside HADES uses 12 HPGe detectors, including three well detectors and two dual-detector systems.

The goal of this subsection is to clearly elucidate the impact and importance of the underground location on the application of gamma-ray spectrometry. As already mentioned, this has many applications in different scientific fields, but will also play an important role in this master thesis research since one of the detectors that needs to be validated (Ge-14) is

located at the HADES URF. An important factor that impacts an ordinary, above ground obtained gamma-ray spectrum is the background radiation originating from natural radioactivity in materials all around us (for example ^{40}K and radium in building materials, ^{210}Pb in lead shielding) and the contribution of cosmic rays which are caused by solar particle events and supernova's. Cosmic rays produced by these two events mainly consist of high energy protons and a smaller portion of alpha-particles and to an even lesser degree of heavier nuclides and electrons. It is only when these protons enter our atmosphere that other highly energetic particles are produced by all types of interactions with air molecules, this is referred to as the particle shower illustrated in figure 5. In figure 4 the variation of the cosmic radiation because of these interactions is presented as a function of altitude [2], [5], [7].

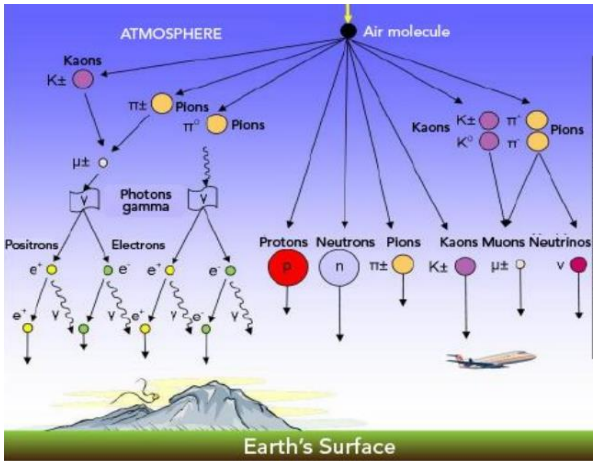

Figure 5: Secondary cosmic ray particles [5, p. 301]

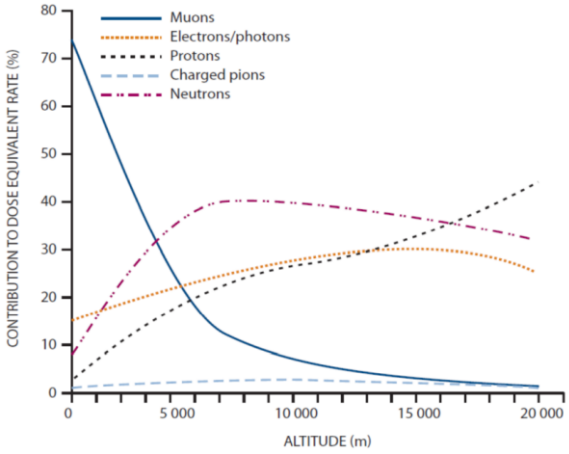

Figure 4: Cosmic ray particles to altitude [5, p. 303]

Besides the production of different types of energetic particles, cosmogenic radionuclides can also be the result of these interactions with different types of molecules in our atmosphere. This leads to the formation of radionuclides as: ^{3}H, ^{7}Be, ^{14}C and ^{22}Na which contribute to the annual collective effective dose $^{14}C \rightarrow 12$ Sv $^{22}Na \rightarrow$ 0,15 Sv $^{7}Be \rightarrow 0{,}03$ Sv $^{3}H \rightarrow 0{,}01$ Sv. All this translates in the so-called background in a gamma-ray spectrum which is visible as a continuum across all different energies in the spectrum. By being 225m underground these background values are present to a much lesser extent because of this thick, natural 'shielding' (mainly by the reduction of the neutron flux). As already mentioned the instrumental background count-rate is extremely low, in some cases representing as little as 0.02% of the normal reading above ground. This also enables the operator to implement thicker layers of lead and copper to shield the inside of the detector even more, resulting in even lower background. Enlarging shielding above ground is also desired, but limited because of the leading disruption caused by the creation of secondary particles/radiation by interaction of the cosmic rays with this shielding. Lead is for example a neutron multiplier and copper is easily activated. In HADES these interactions are strongly reduced as explained thus enabling such acts [5], [6].

These effects are visualised in figure 6 where a gamma-ray spectrum of three different detectors are compared to each other. B lowers the continuum of A because of its design with radio-pure materials. C shows a decrease in continuum by an order of magnitude around 10^3 compared with detector B [2].

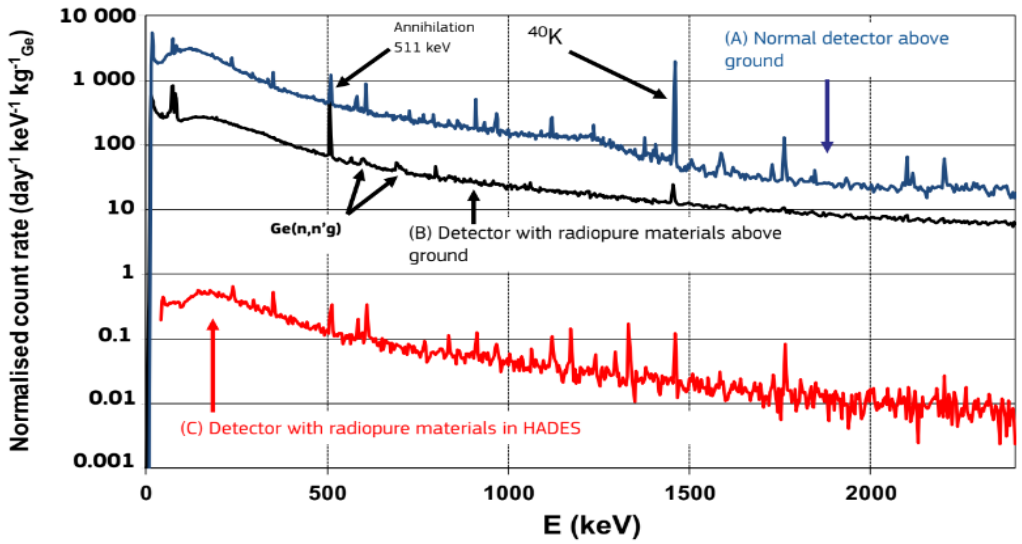

Figure 6: Normalised background spectra from three HPGe detectors. (A) Normal detector above ground. (B) Detector built using radio pure materials, and therefore many of the peaks seen in A have disappeared. (C) Located in HADES and therefore the continuum level is several orders of magnitude lower [2, p. 17]

d) Utility and application of underground gamma-ray spectrometry

The reduction in the background of a gamma-ray spectrum opens up the use of spectrometry for different types of new practical applications. Its utility lies in the fact that low activity samples are now measurable. When measuring an extremely low activity sample (for a certain application) in an above ground detector the values would not stand out due to the background contribution of natural radioactivity and cosmic rays. In the spectrum for detector A in figure 6, it can be seen that this problem more often is the case for low gamma energy emitting radionuclides since the background scatter is higher at low energy levels, thus making it harder to detect the low energy gamma-rays (albeit the inherent efficiency of the detector is higher at lower energies). In HADES it is easier to detect low activity samples because of the reduction in the background. This results in many practical applications, one of which is tracing the currents in the Pacific Oceans and will be briefly explained here as an example [2].

The 11th of March 2011 the Fukushima accident happened in Japan. In spite of all adverse effects of this catastrophic event, this accident provided a unique opportunity for marine biologists and oceanographers to observe and map sea currents. Due to the Fukushima accident, anthropogenic radionuclides were released into the Pacific Ocean whereby this site acted as a well-defined point source for input to the Pacific Ocean. The radionuclides were carried away from the point source by sea currents, which are not fully understood and mapped to this day. By being transported through the ocean, the radionuclides diluted as it moved further away from the point source. Samples were collected at different locations at different distances from the point source, as shown in figure 7. The amount of radioactivity present in a sample provides valuable information about these sea currents, used for mapping the food transport for marine life in the Pacific Ocean and therefore predicting the movement of schools of fish in certain directions or to help with modelling global warming. More obviously, it was also possible to make a better estimation of the total release of radioactivity from Fukushima. Performing such measurements would be pointless above ground because of the

low values in activity (because of dilatation). Typically 1 mBq per litre water and typical samples were about 2 litres [2], [8].

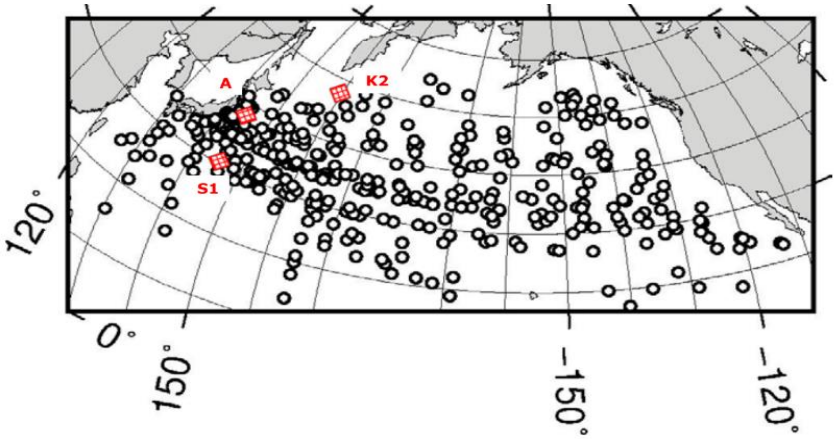

Figure 7: Map of the Pacific Ocean with the 2011 and 2012 locations for surface sampling of water (black circles). Three locations for sampling plankton and particulate matter (red squares) are also given [2, p.43]

2.1.2 RADMET laboratory (above ground)

The RadioNuclide metrology team (RN) was the first operational team of JRC-Geel. Already in 1959 RN started operation at the premises of SCK CEN in Mol. When the first building of JRC-Geel (The main building, 010) was erected in 1960, the group moved there and started to set up a laboratory. The initial tasks were focused on working on establishing international equivalence and measuring decay data. For this reason, many new unique instruments were conceived and realised. The reason for developing instruments is that each radionuclides decay in a different way with different set of decay parameters. So, one can think of designing certain instruments optimised for measuring certain radionuclides, like $4\pi\beta$–γ-coincidence detector systems and the 4π-CsI–detector. With such detectors, the RN performs so-called primary standardisation. This refers to techniques of measuring activity without having to rely on an efficiency calibration. It is physics and the design of the detector that enables the scientist to come up with very accurate activity values. Such measurements are performed in so-called key comparisons organised by the Consultative Committee for Ionising Radiation (CCRI) at the International bureau for weights and measures (BIPM) that is in charge of realising and maintaining the unit Bq. As the key comparison reference value (by which all SI-traceable radioactivity measurements compare) is defined as a weighted mean of the laboratories taking part in a key comparison, one can say that certain instruments at JRC-Geel contribute to establishing the world reference for certain radionuclides [2], [9].

Over the years, the number of applications and work programmes have grown due to needs from member states and steering of the JRC work programme. For example, after the Chernobyl accident in 1986, the low-level group of the RN was formed. It began to look at low-level measurements and work on producing reference materials for environmental radioactivity measurements. In 1992, the RN put its first HPGe-detector in HADES. This was an exploratory project carried out by the low-level group to see how much was to gain. It turned out that a lot was to be gained and since 2000 the ultra-low-level measurements carried out in HADES are an essential part of the RN's many detectors. They serve to support many projects and programmes [1], [9].

In 2003 the RN organised its first European scale proficiency test (PT), the so-called REM PT. REM (Radioactivity Environmental Monitoring) is a JRC programme to support member states and DG ENER in realising Article 35 and 36 of the Euratom Treaty. The treaty says that member states shall monitor radioactivity in the environment and report to the Commission. It also says that the Commission, supported by the JRC, shall verify these operations. RN does so by producing radioactive reference materials and characterise these both with regards to radioactive content and chemical characteristics. These materials are sent out to circa 100 laboratories that measure and report back to RN who then collates data and writes reports about the status of monitoring. Many of the above ground detectors serve to characterise these reference materials. When new type materials (i.e. radioactive environmental matrices that have never been produced on-site before) like hay, maize, building materials and berries are produced it is also necessary to carry out many radiometric tests to ensure the quality of the material (homogeneity, stability, suitable level of radionuclides etc.) [1], [9].

The RN is also a key laboratory in the world for certifying reference materials from international producers, like the IAEA and many national metrology organisations [1], [9].

Finally, The RN is still involved in developing new instruments. At the moment two new instruments are being commissioned: A conversion electronic spectrometer and a time-of-flight alpha-particle spectrometer. Both may serve to significantly improve decay data for important radionuclides [9].

3 Gamma-ray spectrometry

The most common laboratory technique used for analysing samples containing gamma-ray emitting radionuclides in any radiometric laboratory is called gamma-ray spectrometry. The key instruments are High Purity Germanium (HPGe) detectors, used because of their exceptional energy resolution. The germanium crystal is supported with required electronic components to convert radiation interaction in the sensitive part of the detector to a digital signal suitable for establishing the spectrum [3], [7].

3.1 Interactions with media

In order to understand future obtained spectra, it is important to elucidate different types of gamma interactions and to explain different phenomena in the eventual spectra (sum peak, Compton background, etc.). The basic understanding of these concepts are not only required to analyse and interpret obtained spectra, but they form the essence of being able to detect radiation (and obtain spectra) in the first place. More specifically, a detector perceives radiation because of the ability of ionising radiation to interact with a medium. Since gamma-ray spectrometry is based upon the interaction of gamma-rays, the fundamentals of these types of interactions are further discussed in this paragraph. In general there are four main types of interactions that may occur when a photon beam hits material: the photoelectric effect, Compton scattering, pair production and Thompson and Rayleigh scattering. In paragraph 3.1.5 Special occurring phenomena in a gamma spectrum, the manifestation of these different types of interactions in the gamma-ray spectrum is discussed alongside other prominent phenomena that occur in gamma spectra [7], [10].

First of all, it is important to understand the fundamental behaviour of photon particles before analysing photon interaction patterns. Gamma radiation or thus photon particles can be emitted as a follow-up to alpha or beta decay. When a nuclide is unstable (radionuclide), it seeks to get rid of its surplus of energy to attain a more stable state. Therefore, the radionuclide emits particles such as an ^{4}He (alpha), electron (beta-) or positron (beta+) particle. Different types of radiation are in competition with each other and can occur simultaneously, the dominant way to become more stable and thus emit a certain type of radiation depends on the unstable nuclide itself. After the radionuclide decays, it can be at its ground state or at an excited state. In the case of the latter, the excited nuclide makes the transition to its ground state by emitting gamma-rays, neutrons, etc. depending on the available energy of the excited state compared to the ground state. Now it is very common for a radionuclide to have different excited states and thus different values of energy of the emitted gamma-radiation. An example is the decay of ^{60}Co to ^{60}Ni by emitting electrons (Beta- particles or also called negatrons) which is shown in figure 8. In this case there are two possible excited states to go to which results in the emission of three different gamma energies to finally arrive at the ground state. Later on, in paragraph 3.1.5 Special occurring phenomena in a gamma spectrum and 3.4 Gamma-ray spectrometry calibration, it will be discussed how these decay schemes are transformed into a gamma-ray spectrum by using gamma-ray spectrometry (by measuring with an HPGe) [11].

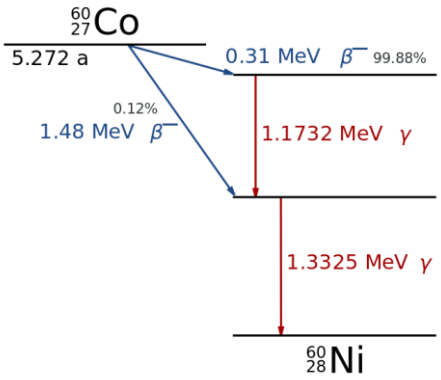

Figure 8: Decay scheme of ^{60}Co [12, p. 3042]

The emphasis here is on the difference in origin between decay radiation types such as alpha and beta radiation and gamma radiation. Besides that, photon particles behave in a completely different way in comparison with alpha and beta particles. First of all gamma-rays penetrate much deeper into matter than charged particles of comparable energy. When a photon beam travels through matter, it behaves as follows: a photon particle is not slowed down in its passage through matter, only the intensity I of the photon beam is reduced, this is called attenuation and is presented as dI/dx (instead of dE/dx for energy loss of charged particle beams). As long as the photon does not interact, it keeps all of its energy. When an interaction does happen, the photon particle disappears from the beam and its energy is transferred to the matter with which it interacts [10], [13]–[16].

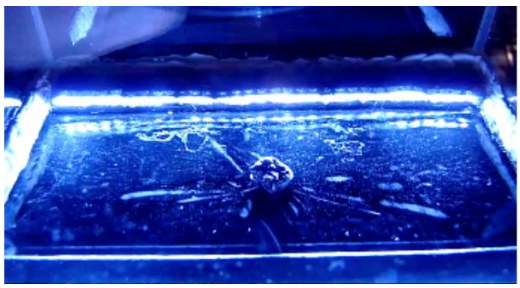

Figure 9: 5 MeV Alpha particles form ^{238}U visualised in a cloud chamber [10, p. 17]

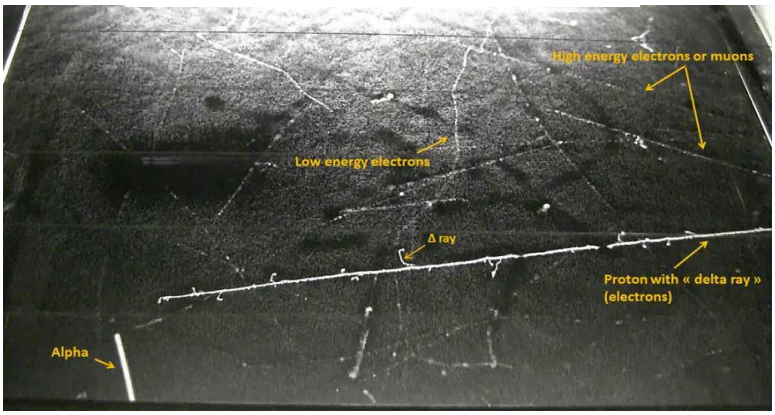

Figure 10: Visualisation of different types of radiation in a cloud chamber [10, p. 1]

Figure 9 and 10 show that alpha and beta particles lose their energy in a continuous way (dE/dx) alongside their track through matter, resulting in a visible track in the cloud chamber. Since an alpha particle has higher ionisation density, it will show as a thicker track in the chamber compared to the electron (beta particle) track. The alpha particle track is shorter because of its higher reaction capacity (bigger particle). Figure 11 visualises the fact that the interaction of a photon is completely different compared to the interaction of alpha and beta particles. They interact at specific singular points of the cloud chamber and even at low energies they penetrate way deeper into matter making it more difficult to visualise compared to alpha and beta particles [10], [13], [17].

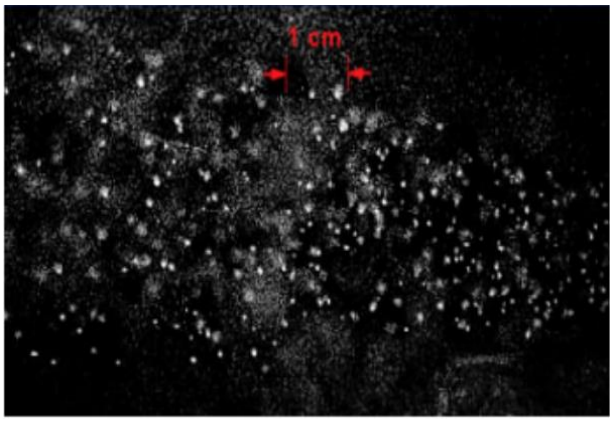

Figure 11: 5.9 keV photons from ^{55}Fe visualised as dots in a cloud chamber [10, p. 17]

3.1.1 Photoelectric effect

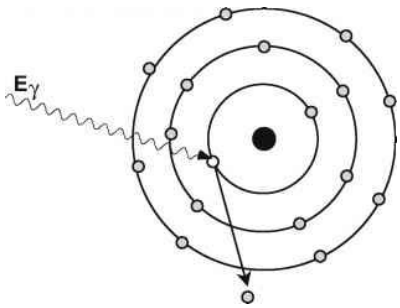

Figure 12: Photoelectric effect resulting in the emission of an orbital electron [18, p. 1]

A first type of interaction photons may undergo is the photoelectric effect. The incoming photon interacts with a bounded atomic electron on which it transfers its energy, resulting in the emission of this electron. This interaction is shown in figure 12. In order for this to take place, the gamma energy needs to be higher than the binding energy of the electron. The value of the binding energy of the electron depends on which shell the electron is located in, in the atomic configuration. The further away from the nucleus, the lower the binding energy, thus the easier it is for the photoelectric effect to take place. The higher the energy of the incoming photon, the more electrons are able to be emitted. It is important that the concerned electron is bound since there would not be preservation of momentum if the electron was a free electron. This type of reaction results in the disappearance of the photon which transfers all of its energy to the electron. Since the electron was originally bound, its kinetic energy after this

interaction is lower than the original energy of the incoming photon (a part was invested in breaking the bound). The cross-section of this interaction is directly proportional to the following statement: $\sigma_{fe} \sim \frac{Z^{4-5}}{E_\gamma^{3.5}}$. This shows that this interaction is dominant for heavier nuclides since they have higher electron density. In case a construction aims to stop gammas effectively, heavier materials such as lead are preferred [10], [19]–[22].

Besides the emission of the photoelectron, there is the possibility for secondary radiation to emerge as shown in figure 13. If the photoelectric effect takes place and the photoelectron is emitted, a hole (where the electron was originally located) appears. Since the whole purpose of the electron configuration of an atom is to achieve the lowest energy state possible, higher placed electrons will fill up this hole, leaving a hole in their original location in the configuration. By doing this, the electron moves to a position of lower energy and therefore this surplus of energy is emitted in the shape of X-rays. Another possibility is that this X-ray in its turn interacts with an atomic electron causing this electron to be emitted (this is only the case when the X-ray has more energy left than the binding energy of this particular atomic electron), this is then called an Auger electron [10], [23], [24].

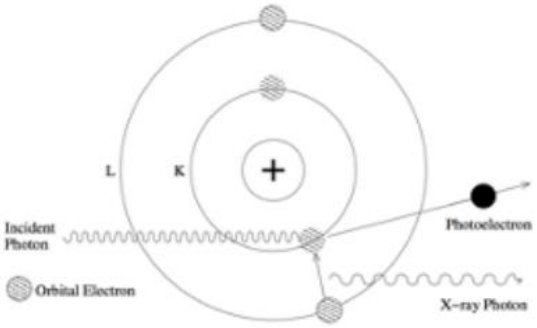

Figure 13: Representation of secondary radiation after the photo-electron effect [10, p. 23]

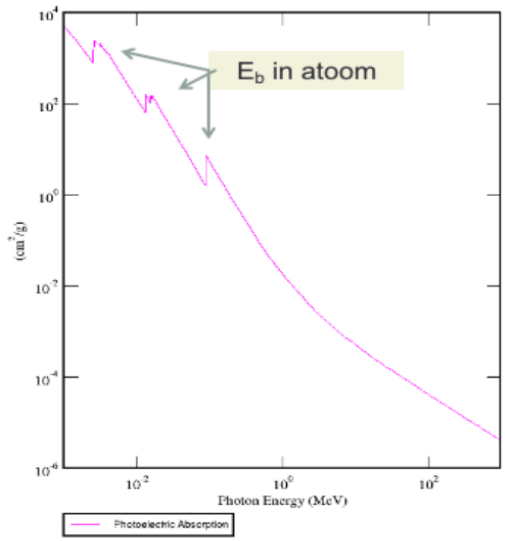

Figure 14: Cross section of photoelectric absorption (in cm^2/g) in function of the photon energy (in Mev) in lead [10, p. 23]

A remarkable effect can be observed when taking a closer look at the representation of cross-section in function of increasing photon energy, shown in figure 14. As indicated by the formula of this interaction it is expected for the cross-section values to decrease when the energy of the incoming photon increases. This is the case, but for the exception of a staircase pattern in the graph. These are called absorption edges. They cease to exist at certain photon energies that correspond to the different binding energies of the electrons in the atom. Thus, every time a photon has enough energy to ionise electrons in the next atomic shell, the cross-section increases since there are more electrons to interact with. This feature is used for different application purposes such as increasing contrast when imaging with X-rays. For example, if one is looking for the presence of lead in an object, this technique may be used. A picture of the object is taken with a photon energy just under the K-absorption edge of lead (the photons have just less energy than necessary to emit electrons in the K-shell via the photon-electric effect). Another picture is taken with incoming photon energy just above this K absorption edge of lead. If lead is present, the contrast is completely different in those two pictures. If lead is not present in the objects, the two pictures are alike, contrast wise [10], [25].

3.1.2 Compton scattering

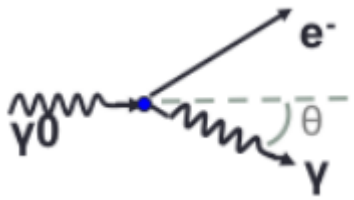

Figure 16: Compton scattering [10, p. 26]

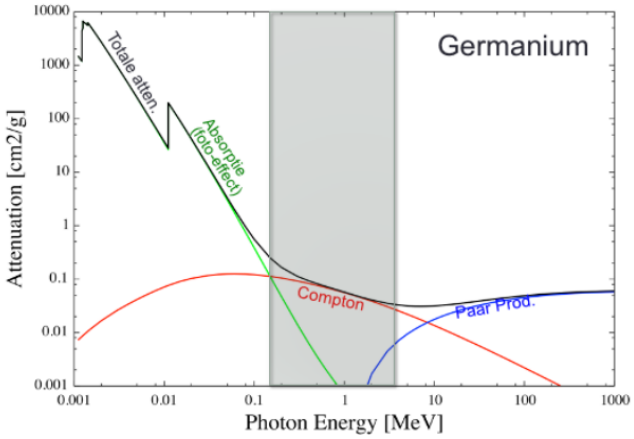

Figure 15: Probability of different gamma interaction types in function of incoming photon energy in germanium [10, p.25]

Another prominent interaction between gamma radiation and matter is the Compton scattering visualised in figure 16. Figure 15 shows that this type of interaction is of more importance at higher photon energies (it is the dominant interaction between 0.1 and 10 MeV photon energy in Germanium). Compton scattering is the inelastic scattering of a photon when colliding with an electron. Therefore, the photon loses some initial energy, transferred to the electron which is emitted. The remaining energy is carried by the scattered photon. Based on the laws of conservation of momentum and energy, the relationship between the initial energy of the photon and the energy of the scattered photon is given by the equation 1, called the Compton equation. This equation indicates that it is not possible to transfer the full energy of the incoming photon to the electron in a single Compton scattering, even if the binding energy is negligible. The maximum energy transfer is obtained when the incoming angle, thèta, is 180° (head-on collision). This phenomenon leads to the existence of Compton background and broader peaks in the spectrum of an HPGe detector. These peaks are called Compton edges and are alongside other phenomena discussed in paragraph 3.1.5 [23], [26]–[29].

$$E_\gamma = E_{\gamma 0}\left[1 + \frac{E_{\gamma 0}}{m_0 c^2}(1 - \cos\theta)\right]^{-1} \quad (1)$$

3.1.3 Pair production

Besides the existence of the photon-electric effect and the Compton scattering there is third common observed interaction that may take place when a photon beam passes a medium, pair production (visualised in figure 10). As shown in figure 17, this interaction is dominant for high energy photon beams. Because of this condition, pair production interactions are not often detected in gamma-spectrometry applications. Only when the use of accelerators come into view such as in radiotherapy treatment facilities or research facilities, these interactions often appear and should be taken into account [10], [23], [30].

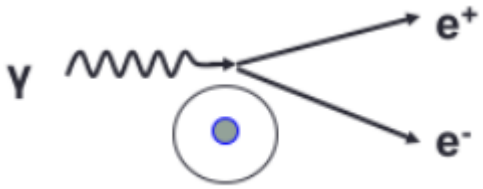

Figure 17: Pair production interaction [10, p. 36]

Pair production alludes to the disappearance of the incoming photon particle which is 'replaced' by an electron-positron pair. Thus in order for this interaction to take place, at least two times the resting mass in the form of energy is needed for the incoming photon. The surplus of energy is then (not always equally) divided to both the electron and the positron. The occurrence of pair production is proportional to Z^2 of the target, meaning it is more likely to take place in heavier nucleuses [10].

Even though it is not easy to observe this effect, figure 18 shows the occurrence of a pair production interaction in a cloud chamber. A magnetic field was constructed so the produced electron and positron become visible by rotating in circular orbits until their energy is dissipated. The radius of the particle's orbit is proportional to the velocity of the particle. Because of their difference in charge, both orbit in a different direction making it possible to distinguish them from each other. The ability of this interaction to take place originates from the relativity theory. Explaining this is beyond the scope of this thesis [10].

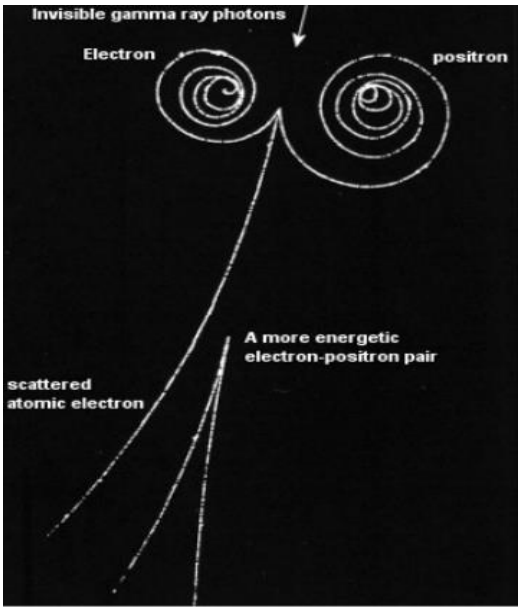

Figure 18: Pair production and triplet production in the cloud chamber [10, p. 37]

A consequence of pair production is the occurrence of annihilation of antimatter. When a particle meets an anti-particle, annihilation takes place allowing both particles to disappear and new particles to exist. In this case, the positron is the anti-particle of the electron. It behaves identically as the electron, but it carries an opposite, positive charge. There is no minimum energy needed for annihilation to take place. At lower energies, two gamma particles both at an energy of 511 keV (in order to respect conservation of energy) occur when electron-positron annihilation takes place, emitted in the opposite direction when both the electron and positron are at rest at the moment of interaction (in order to respect conservation of momentum). At higher energies, other particles (such as the Z-boson) may occur, but explaining this is again beyond the scope of this thesis. Pair production and the annihilation effect can be observed in a gamma-spectrum which is also discussed in paragraph 3.1.5 [10], [24].

3.1.4 Thompson & Rayleigh scattering

Another process photons may undergo is Thompson or Rayleigh scattering. Thompson scattering is seen as Compton scattering in its ‘classic limit’. The interaction is similar to Compton scattering, but it differs from scattering in the energy of the incoming photon being less than the resting energy of the electron. Practically, this results in the need for other formulas to describe the cross section. Rayleigh scattering is the scattering of the photon particle at the atom as a whole instead of an electron. This results in the electrons moving coherently. Since the cross section for this type of scattering is so low, it is negligible in most cases. For both processes there is no energy transfer between the incoming and the outgoing photon, there is neither excitation nor ionisation. Only a change in direction of the photon can be observed [10], [24].

3.1.5 Special occurring phenomena in a gamma spectrum

Figure 19 pictures a typical energy spectrum of ^{60}Co, measured with a germanium detector. A spectrum is a histogram visualising the number of counts registered by the detector for the different measured energies intervals. Earlier, the Compton scattering effect was explained, but how does this impact the spectrum? A photon can undergo Compton scattering multiple times, but as long as all scatterings and the final absorption are in the sensitive area of the detector, the whole energy of the photon is measured as desired. Such a full energy measurement is called a full energy peak (FEP) or a photopeak and is of great interest for this project. This can be seen as a sharp peak in the energy spectrum and corresponds to the energy difference between two excited states or an excited state and the ground state. For this specific example of ^{60}Co, two different peaks can be spotted: one at 1.173 MeV and one at 1.332 MeV. Another possibility is that the scattered photon after a Compton scattering disappears out of the detector. This results in an incomplete observation of the original total energy; such events have a high probability to take place and form the so-called 'Compton background' of the spectrum. Thus, this explains counts at all different energies. Another phenomenon takes place at the maximum energy that can be transferred by one Compton scattering (when the interaction angle is 180°). At higher energy photons, the scattered photon then has an energy of 255 keV and is often not detected after by the detector since it now moves back (180°). In the spectrum this manifests itself by an increase over the Compton background at around 255 keV below the two photopeaks. This is called 'the Compton edge'. Similarly, when a high energy photon is scattered outside the detector back into the sensitive region of the detector, an energy of 255 keV is registered by the detector. This is called the 'backscatter peak'. These special interactions are visualised in figure 20 [10], [31], [32].

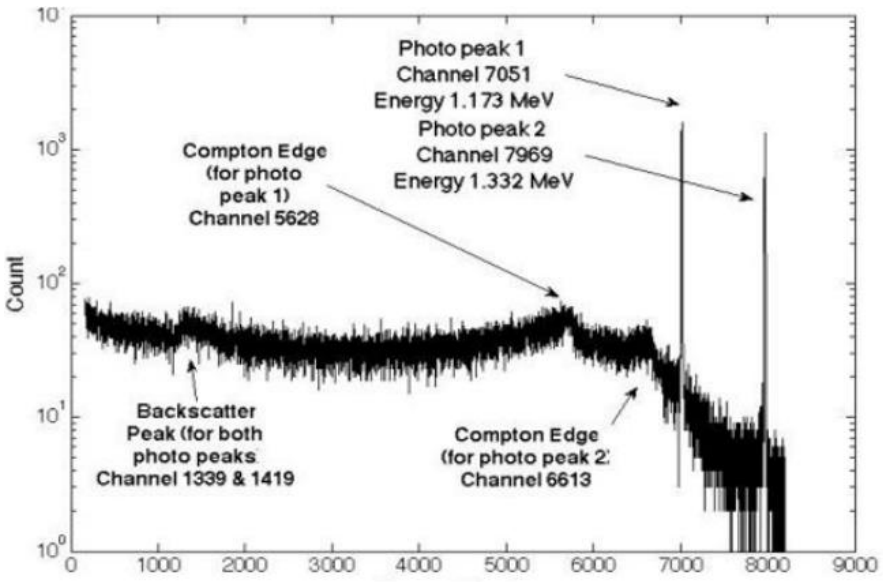

Figure 19: Compton phenomena in the energy spectrum of ^{60}Co [10, p. 29]

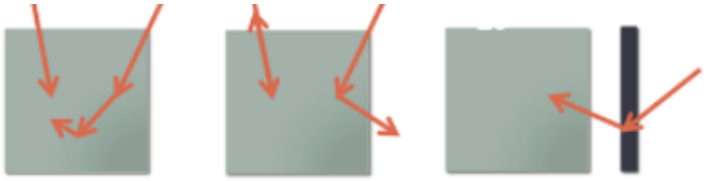

Figure 20: Representation of photopeak, Compton background and backscatter [10, p. 29]

Another prominent interaction at higher photon energies is pair production. When a photon interacts this way, there are also different ways in how this is projected in the spectrum which can be seen in figure 21. As discussed in paragraph 3.1.3 Pair production, a part of the energy is used to create an electron and a positron. Thus, if only the energy of the particles is registered and not the particles itself, this would mean that 1022 keV is not registered by the detector. Fortunately, the positron and electron annihilate at which 2 photons of both 511 keV are created. If both interact, the full energy peak of the original photon is then registered resulting in the photopeak. If only one out of these two photons is not registered in the detector by leaving the sensitive area without any interaction. 511 keV of the total energy misses, resulting in the 'single escape peak' in the spectrum. When both photons escape, 1022 keV is missing and thus a 3rd peak is present in the spectrum: 'the double escape peak'. It is important to keep in mind that such peaks are only present when the sample contains radionuclides with gamma-energies above the threshold of 1022 keV. Another possibility is that the annihilation takes place outside of the sensitive region in the detector. In that case, if one of those two photons then interacts in the detector, a peak of 511 keV is seen in the spectrum [31]–[33].

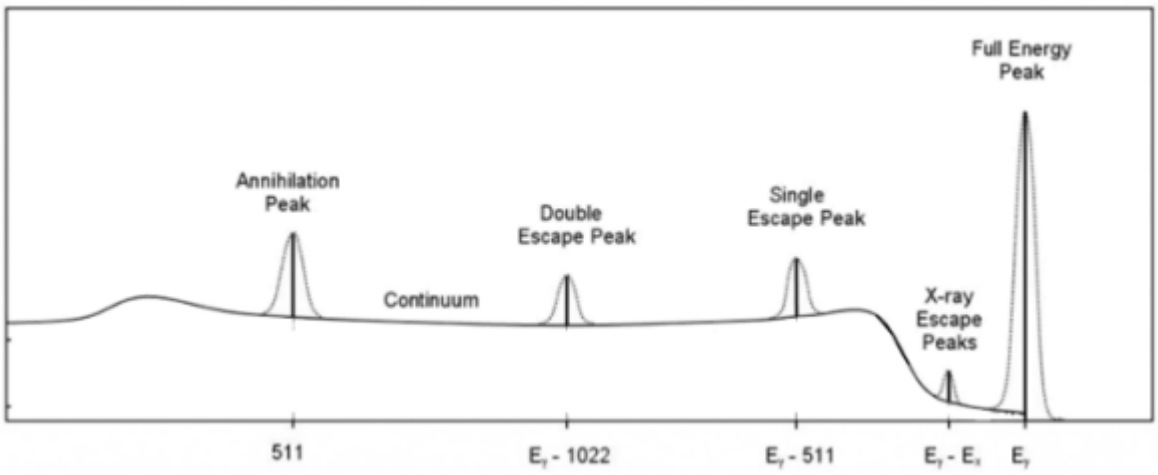

Figure 21: Pair production phenomena in the gamma-ray energy spectrum [10, p. 41]

Last but not least, there is another phenomenon that is visible in some spectra and plays a major role in this project work. When looking back at the spectrum of ^{60}Co, another peak is visible at around 2.5 MeV. However, there is not a single energy level in the decay scheme of ^{60}Co that corresponds with this specific energy. The reason this occurs is due to the fact that both disintegrations (1.17 MeV and 1.33 MeV) take place and result in gamma's that interact and thus deposit their energy at the same time in the crystal. If the time interval between both energy depositions is low, the detector is then not able to tell the difference. This proves the presence of 'the sum peak' in some spectra which is at an energy corresponding to the sum of different gamma-disintegration energies. The sum peak can be seen in figure 22. In paragraph 3.5 Calibration of HPGe detectors, the impact of this phenomenon on this project is further explained alongside other important factors [26], [34].

.

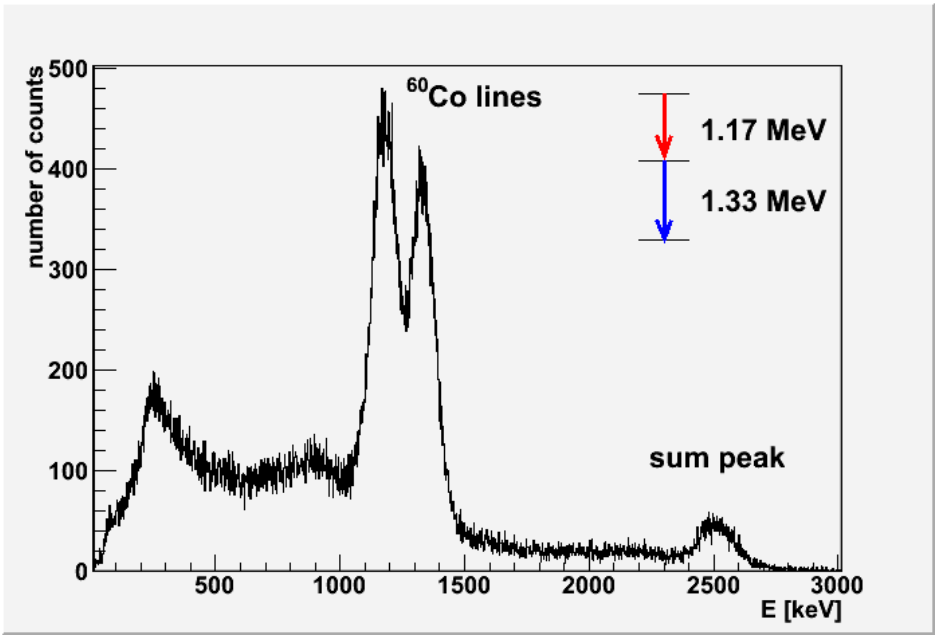

Figure 22: ^{60}Co spectrum with the presence of 'the sum peak' (note that there is a weak gamma-ray directly from the 2505 keV level to the ground state that interferes with the sum-peak). [35, p. 1].

3.2 Decay data

In order to evaluate and test the constructed computer models of the Ge-T10 and Ge14 HPGe detectors, simulations of these models need to be executed. In addition, the spectra from the experimental measurements of the reference sources need to be fitted and analysed. After that, the simulation results are compared with the experimental data using the software GLysis. All these operations need specifications of the used radionuclides like absolute activity and decay parameters like half-life and emission probabilities for carrying out the process of calibration. For example, the shell file for executing simulations needs specifying of which radionuclides and peaks should be simulated. Besides that, correct information about half-lives and gamma-emission probabilities for the different peaks are needed. The accuracy of this information is critical in order to have an as low as reasonably achievable deviation between the real dimensions and the dimensions used in the simulations. Incorrect modelling of these values will generate unacceptable large divergence when validating the model.

Therefore, all values are imported from the database of the international DDEP (Decay Data Evaluation Project), which is presently hosted and maintained online by the French national radionuclide metrology laboratory: Laboratoire National Henri Becquerel (LNHB). Furthermore, when evaluating the results and comparing experimental results with simulated results other sources are used which are often more complete but less accurate. Decay schemes are taken from: "Table of isotopes (seventh edition)". Gamma-emission probabilities and other decay data is checked in "Table of Radioactive Isotopes". These books are based on the ENSDF database (Evaluated Nuclear Structure Data File) [36]–[38].

3.3 Instrumentation and software

In order to be complete, a short outline is given about the instrumentation and software used to develop, validate and test the computer models for the Ge-T10 and Ge14 detector.

3.3.1 HPGe-detector

A computer model will be improved, validated and tested for both the Ge-T10 and Ge14 HPGe detectors. HPGe detectors are classified as semiconductor detectors. The main component of such a detector is the germanium-crystal. Ionising radiation interacts with these crystals, generating electrons and holes which are then collected at the anode and cathode, respectively creating a signal in which the pulse height is proportional to the deposited energy. Furthermore, the intensity of the signal at a given energy is proportional to the activity of the identified radionuclide. Such crystals are classified based on their molecular structure, different types are: Molecular crystals, Ionic crystals, covalent crystals and Metallic crystals. Germanium crystals are covalent crystals since the outer shell of the atomic configuration of the atoms is partly filled. Each atom therefore shares its valence electrons with its four neighbouring atoms. Because of such interactions, the crystal structure and its bounds are highly directional dependent [10], [27], [39].

a) Crystal structure

In order to understand the working principle of a Germanium crystal and why this crystal is opted for in gamma-radiation detection, the creation of the band structure is first explained. Figure 24 shows the lattice structure of diamond, Si and Ge. The difference between their lattice structures lies in different lattice constants and thus other dimensions.

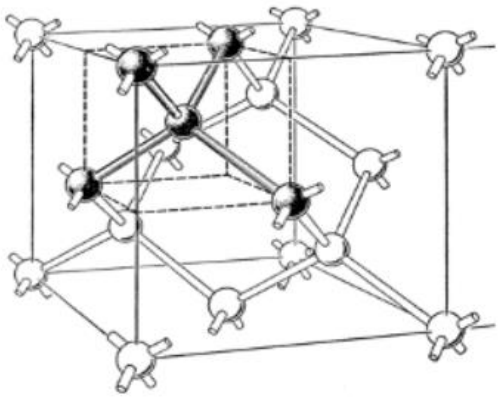

Figure 24: Lattice structure: silicon and germanium [10, p. 208]

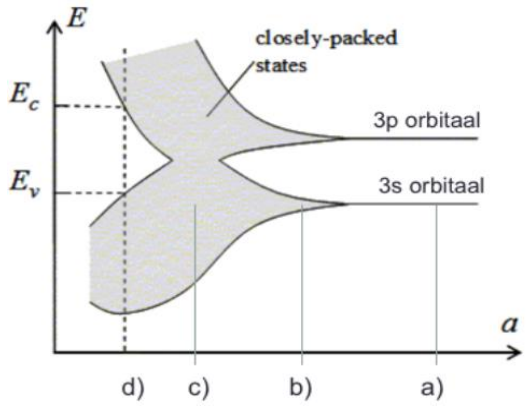

Figure 23: Band structure: germanium [10, p. 208]

A lattice structure of a large number (N) of atoms is considered. As shown in figure 23, It is assumed that the initial distance "a" between the atoms in the lattice is very large. Then, it is considered how the energy levels change as the distance between atoms is gradually reduced. At distance a), the interatomic distance between the atoms is large. Therefore, each atom in the crystal behaves as a free atom. If the distance between atoms is further reduced until the hypothetical distance b) is reached, the electrons at the outer shell (valence electrons) ‘feel’ each other's presence. Therefore, the energy levels start to change and the pure s and p orbitals in the atom's configuration are no longer energy levels of the atom itself, but they

now become new energy levels of the whole system (crystal). They are now considered as a mix of both s and p orbitals and are called sp-hybridisation levels. According to the Pauli-principle, electrons with opposing spin attract each other, creating a reduction of energy of all existing energy levels. Electrons with a spin in the same direction repel each other, resulting in an increase of energy in the existing energy levels. Instead of obtaining many degraded energy levels, reducing distance and the Pauli-principle result in many energy levels close to each other, called energy bands. This described change applies only to the outer shells of the atoms since they are responsible for chemical bindings. The lower energy levels such as $1s^2$, $2s^2$ and $2p^6$ are stronger bound to the nucleus. Therefore, no overlap with neighbour shells can take place and thus no band structure is formed there. Moving the atoms even closer to position c), the more the previously created energy bands split up. Eventually, the band created from the 3p orbitals overlaps with the band from the 3s orbitals. A band at greater energy level is thus created with a capacity of 8N states, occupied with 4N electrons making this band half filled. Decreasing the distance between the atoms even more till position d), splits up the band of 8N states in two bands that each have 4N states. Electron couples with the same spin sit at the upper band, electron couples with opposing spins, which are energetically more favourable, sit at the bottom band. The bottom band is fully filled and is called the valence band. The upper band is completely empty (at T=0 k) and is called the conduction band. The distance between those two bands is called the forbidden gap. An energy gap E_g is assigned to the forbidden gap [10].

An important part of radiation detection in such crystal detectors is the ability of the created electron-hole pairs to transfer from the valence band to the conduction band. Before explaining the detection principle, the ideal crystal material for a detector is scrutinised. In semiconductors the distance between the valence and conduction band is small enough in order for the charged particles (electrons) to pass through and get to the conduction band because of thermal excitation. Because of this, a number of free charged particles exist, depending on the temperature of the crystal. Depending on what the atoms and impurities are in a crystal, an amount of energy is required to reach the conduction band and thus cross the forbidden zone. The difference in energy gap E_g between different material groups is visualised in figure 25. Practically, conductors can’t be used to detect ionisation caused by radiation, if we want to count the released electrons and holes created by ionisation in such a crystal, this signal would disappear into the background among the many conduction electrons that are always there. Therefore, only semiconductors or insulators remain as optional crystal materials to detect radiation. Since the average needed energy to create an electron-hole pair in a semiconductor is lower than in an insulator (because of a smaller forbidden zone), semiconductors are chosen as the desired material to detect and count radiation. A crystal composed of purely Si atoms has a forbidden zone of 1.1 eV, purely out of Ge atoms the crystal has a forbidden zone of 0.7 eV. Therefore, Silicon acts as an insulator at room temperature. Germanium on the other hand, has a non-negligible number of electrons that are transferred to the conduction band at room temperature because of thermal excitation, in such a way that a germanium crystal would act as a conductor at room temperature. Temperature thus plays an important role in the determination of the crystal being an insulator or a conductor. Germanium is preferred, but needs extra support to counteract the signal caused by thermal excitation [10].

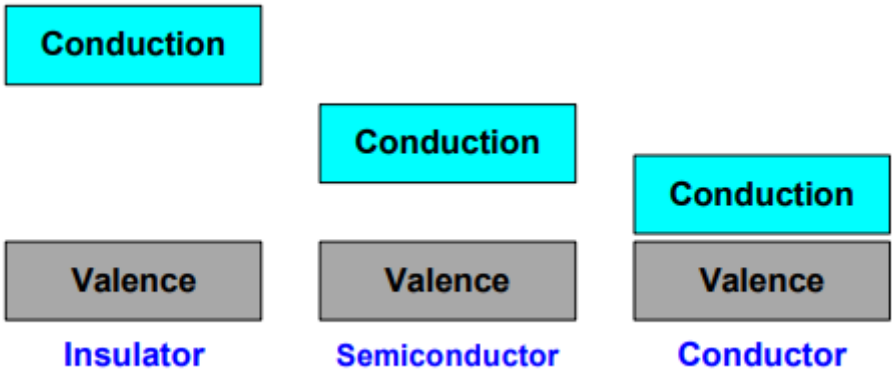

Figure 25: Band structure for electron energies in solids [39, p. 7-1]

b) Deadlayer

Before discussing the detection principle, it is of great interest to explain the concept of sensitive volume and the presence of a deadlayer. Generally speaking, at the surfaces of semiconductor detectors there is a deadlayer present that either is the result from natural or induced passivation or it is created during the contact-making process. Ionisation produced by charged particles moving through this region is inadequately collected and recorded by the designated electronics, which causes deviations from the ideal case in both energy deposition and resolution. Therefore, the sensitive or active volume of a semiconductor detector is the crystal itself excluding the deadlayers [10]. The exact way in commercial companies produce the contacts is a matter of some secrecy and not all details are available in scientific articles. This also highlights the need for this work as an exact description of contacts/deadlayers cannot be obtained from manufacturers. Today most n+-contact are made by diffusing Li-ions into the crystal. Such contacts/deadlayers are typically a few hundred micrometres thick. Using special techniques, some companies are today proficient in making Li-diffused deadlayers on below 100 micrometres albeit for a limited area. The p+ contact is typically implanted using e.g. B-ion. Such contacts/deadlayers are much easier to make really thin, even below one micrometre. Research shows that:

> These layers correspond to the doped regions defining the semiconductor properties of the device, ohmic contacts to bias voltage and readout electronics and/or undepleted volumes of under-biased detectors. Deadlayer effects have received detailed attention in the spectroscopy of low-energy gamma and X-rays, which deposit energy in or near the deadlayer. Hartmann et al. [3] carried out measurements of the charge collected from deadlayers in p-n junction detectors. A study of the charge collection from Li-diffused contacts on Ge detectors has been reported by Aguayo et al. [4]. Similarly, for charged particles, energy loss in even the thinnest of deadlayers can amount to a significant fraction of the total energy deposition for radiations of interest in nuclear and particle physics experiments. A 20-keV electron, for instance, will deposit approximately 1% of its total energy in a 100-nm silicon deadlayer. In high-precision measurements, the thickness of the deadlayer and the fate of charges created therein must be taken into account [40].

Besides its clear physical importance in HPGe detectors, deadlayers also play an important role when validating a MC model of the detector. Not only is it necessary to include the surface deadlayers in the computer model, it needs to be taken into account that the thickness of the deadlayer may vary over time. Therefore, adjustment of deadlayer thickness is necessary to achieve accurate simulated efficiency and is one of the parameters to play with when validating the MC model [41]–[45].

c) Working principle of the detector

When ionising radiation enters the sensitive volume of the detector (the Ge crystal without deadlayer area), it interacts with the semiconductor material, creating electron-hole pairs in the valence band. These particles will operate as the charge carriers in semiconductors. The number of electron-hole pairs is proportional to the energy of the incoming ionising radiation. Excess amounts of energy of the radiation (after the electron-hole pair is created) is ceded upon these particles. This allows many electrons to transfer from the valence band to the conduction band. An equal number of holes are created in the valence band. An electric field is created over the crystal, compelling both electrons and holes to travel to the nearby electrodes where they result in a pulse that is measured afterwards (the number of pulses is counted simultaneously). This process is shown in figure 26. The pulse itself carries information about the energy of the original incident of the ionising radiation. The number of pulses gives information about the intensity of the radiation. It is also possible to determine the origin of radiation by analysing the energy of these pulses (spectra analysis). Signal processing and the use of auxiliary components for correct radiation detection are talked more about in paragraph 3.3.3 Electronics [10], [27].

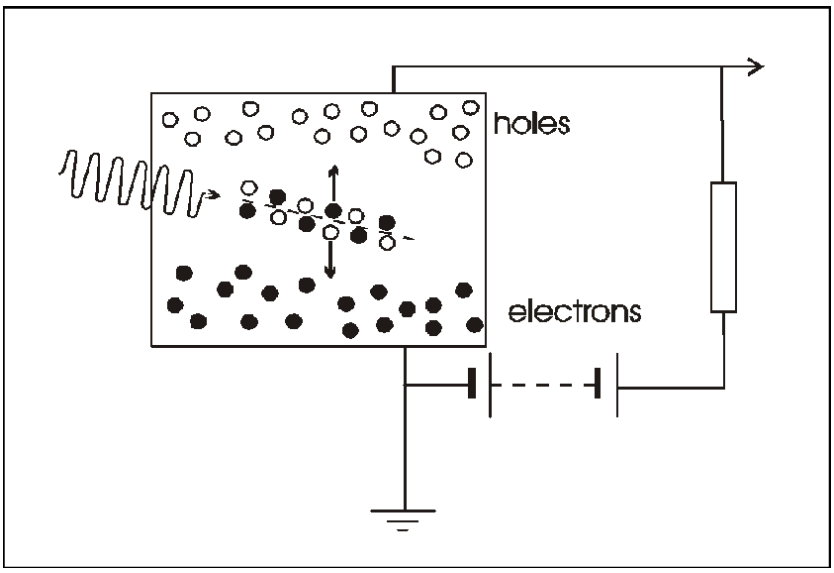

Figure 26: Principle of a semiconductor detector [46, p. 56]

One can conclude that the smaller the bandgap, the better the resolution of the detector. Since a crystal composed of purely Si atoms has a forbidden zone of 1.1 eV, purely out of Ge atoms the crystal has then a forbidden zone of 0.7 eV the last one offers a better resolution. However, a major drawback to take into account is the fact that the smaller the bandgap, the more thermal conduction of electron-hole pairs. It gets easier to promote electrons to the conduction band solely by thermal excitation. This process is already non-negligible at room temperature. Thus, the material behaves increasingly as a conductor. The higher the temperature the more

electrons are present in the conduction band because of thermal excitation. The number of electrons in the conduction band at a certain temperature is given by equation 2 (this is without interaction of ionising radiation and thus solely an effect of temperature and material properties (bandgap)). This effect in general is an undesirable effect since this creates pulses and thus a signal on itself which would for example be the typical signal of a 1 MeV gamma. For the quality of detection, one wants to eliminate this created bias. In order to measure the free electrons and holes created by ionising radiation and meanwhile, ignoring the electrons and holes created by thermal excitation can be achieved by converting the crystal into a **diode**. This is sufficient for a Si-crystal but since the bandgap in a Ge-crystal is even lower, extra **cooling** is needed to suppress creation of electron-hole pairs by thermal excitation. Besides that, cooling offers the advantage of suppressing the increase and deformation of the deadlayer [10].

$$n_i = A \cdot T^{3/2} \cdot e^{-\frac{Eg}{2kT}} \tag{2}$$

As a remark, the equation above assumes that the crystal is 100% pure which is never the case (not even in HPGe although the impurity concentration is as low as $0.8*10^{10}$ cm^{-3}). This results in more free charged particles than estimated. Since there are uncertainties on the purity of the material one does not know for sure how many free charged particles there are and thus what bias they contribute in the final spectrum. Therefore, impurities can be used to our advantage. Through the targeted introduction of impurities into the crystal, called doping, the amount of free charged particles can be controlled. By doing this, it is possible to adapt some properties of the semiconductor to our likings. More specifically, Ge and Si are called indirect semiconductors meaning that the electrons that are present in the conduction band take in special states that differ a lot from the position of the holes which are still present in the valence band. Therefore, band-to-band recombination is highly delayed. Recombination is the collision of an electron and hole, leading to their disappearance. Besides the loss by band-to-band recombination, there is another factor that plays a major role in signal loss by recombination of electrons and holes, called traps. Traps are impurities in the crystal that can be seen as a staircase between the valence and conduction band, making it easier for the electron and hole to travel to the other band and recombine with each other (shown in figure 27). This lowers the lifetime of free charged particles drastically. Practically in indirect semiconductors like Si and Ge, impurities form the dominant factor of recombination losses. This phenomenon should be avoided or at least controlled in such a way that the operator knows the number of impurities and thus time of recombination losses. This is because this phenomenon is detrimental in two different ways: first of all, charges that come from ionising radiation detection that one wants to detect have a lower lifetime leading to less of them being collected and counted, thus signal loss. Secondly, extra charges can climb from the valence band to the conduction band which practically leads to a leakage current. This in its turn goes hand in hand with noise which is detrimental to the energy resolution of the semiconductor detector. In a spectrum, this translates to wider edges of Gaussian peaks and thus lower energy resolution. This needs to be avoided at all costs since an HPGe detector is mostly used in applications for its high energy resolution. Therefore, the principle of **doping** is applied in the production process of the crystal [10], [27].

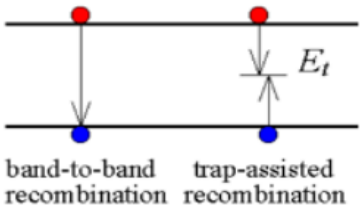

Figure 27: Principle of traps caused by impurities [10, p. 218]

When compared to the energy needed to produce paired ions in a gaseous ionisation detector, the energy needed to produce electron-hole pairs in semiconductors is incredibly low. Therefore, the statistical variance of the pulse height is lower and the energy resolution is greater in semiconductor detectors. Since electrons move quickly, the time resolution is also excellent. The density of a semiconductor detector is particularly high in comparison to gaseous ionisation detectors, and charged particles with high energies can emit their energy in a semiconductor with very small dimensions. For measuring gamma's a decision must be made between using a semiconductor or scintillator detector since a gaseous ionisation detector is not capable of stopping a good fraction of gammas. Figure 28 shows the difference in timing and energy resolution. Overall it can be stated that the energy resolution of semiconductors is better while scintillators are generally faster. Table 1 lists the main pros and cons of both types [10], [47].

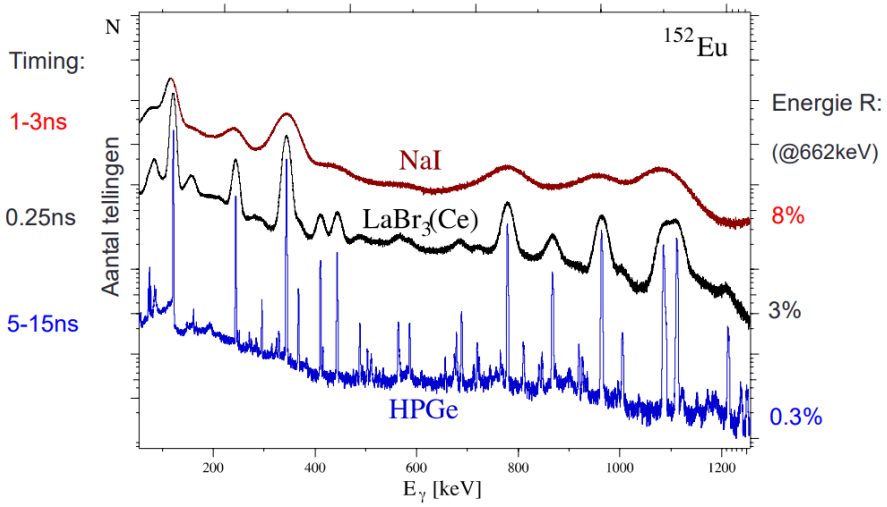

Figure 28: Timing and energy resolution comparison between scintillators and HPGe [10, p. 328]

Table 1: Comparison between Germanium and Scintillator detectors of their major properties [10, p. 329]

Properties	***Germanium detectors***	***Scintillator detectors***
Price	*Extremely expensive (>> $10000)*	*Relatively affordable*
Size of sensitive collection volume (impact on detection-efficiency)	*Size limitation because of the specific production process for the crystal*	*Can be available in bigger sizes*
Atomic number (impact on detection-efficiency)	*Lower Z-values*	*Can provide higher Z-values*
Cooling	*Essential for its functioning (< 110°K)*	*Not necessary*
Time resolution	*Not the best time resolution (5 – 15 ns)*	*Great time resolution (<< 1ns)*
Position information	*Less suitable*	*Suitable (for example in: PET / Spect).*
Radiation type identification	*Not suitable*	*Can Identify radiation types (PSD)*

3.3.3 Electronics

It has been discussed how the semiconductor crystal itself is not sufficient for performing good radiation detection or to perform radio spectrometry. There is need for extra cooling, doping and the crystal should be transformed into a p-n junction (diode). Last but not least, after the electron-hole pairs are created, a signal processing system is needed to count and process the produced signal to a spectrum [39], [48].

a) Cooling

As already mentioned, is it of great importance to consider the operating temperature and bias across Ge detectors. Liquid nitrogen is used to cool down Ge detectors to a temperature around 90 Kelvin. Because of this drop in temperature, there is less leakage current and thus noise which is detrimental for a good energy resolution. If utilised at room temperature, there would be unusable amounts of thermal noise because the thermal creation of electron-hole pairs would outweigh the production by radiation. Since Ge detectors have a shorter band gap than scintillators (which is around 50 eV for scintillators and 0.6-1 eV for Ge), cooling is only necessary for Ge detectors. Figure 29 shows a new design where the cryostat and detector no longer share the same vacuum, making it possible for the operator to remove the detector himself. Figure 30 shows how this is normally put into practice [10], [27], [49].

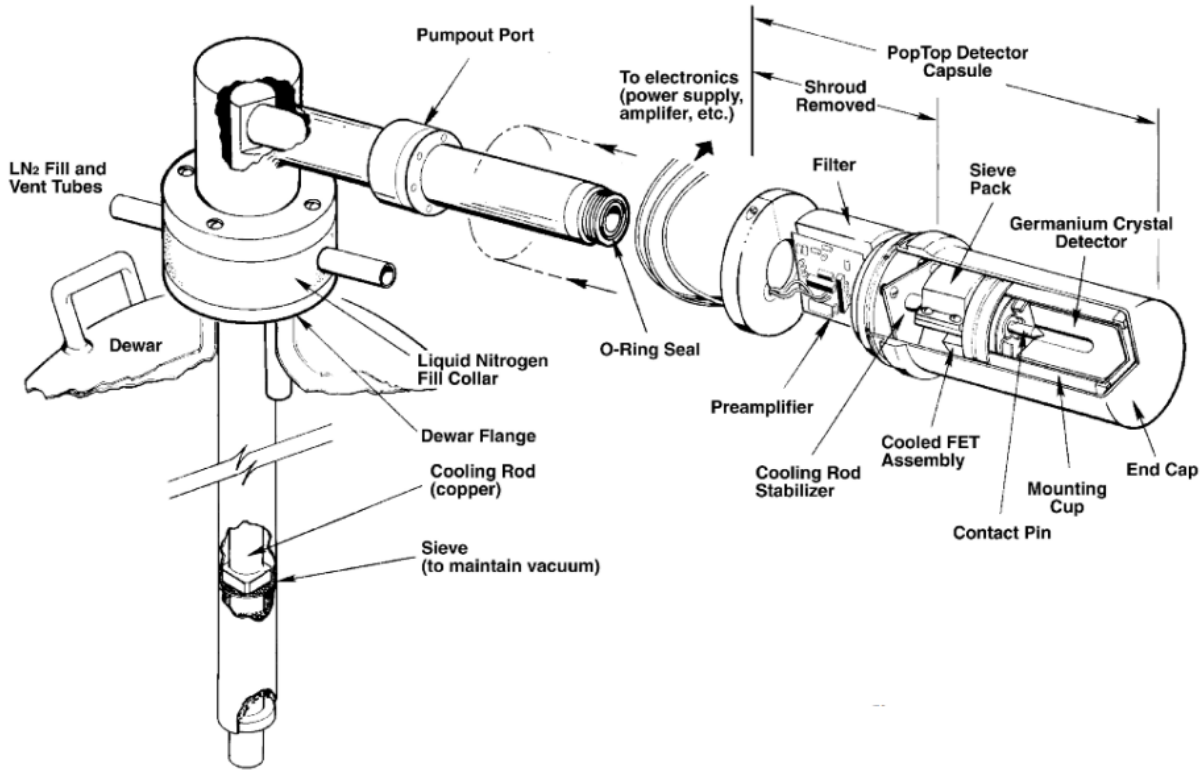

Figure 29: Example of a cooling performed by a special dipstick cryostat. HPGe crystal, pre-amplifier and high voltage filter are stored in one detector module attached to the cryostat as a unit, making it possible to get the detector out of the cryostat since they do not share the same vacuum unlike in usual cryostat designs [50, p. 2]

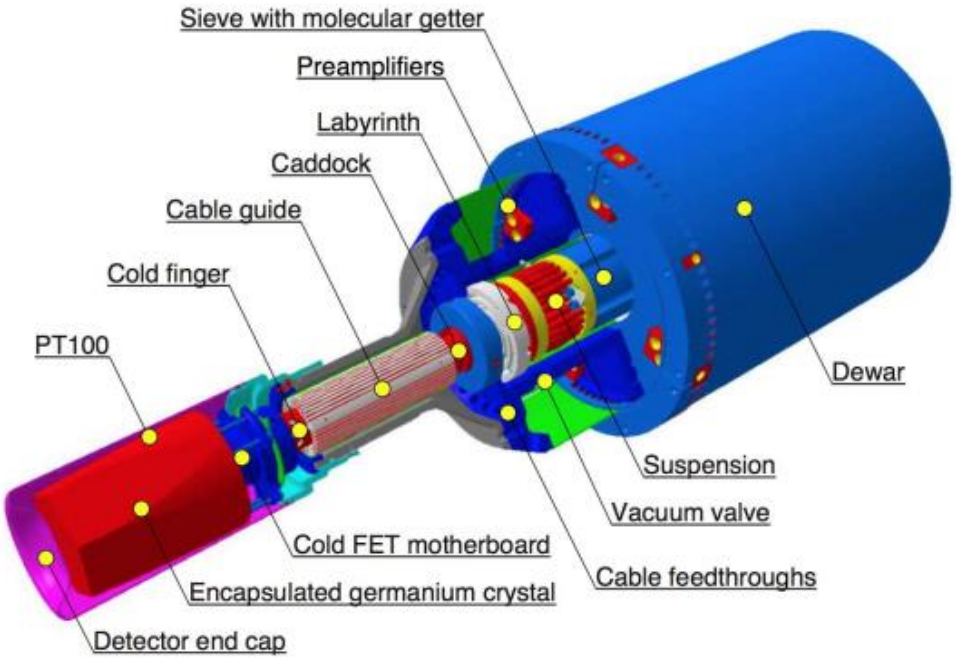

Figure 30: Cryostat for the cooling of an HPGe where the detector is part of the cryostat [10, p. 275]

The main parts of the cryostat design in figure 30 are explained since this is the most common design in practice [10]:

- **Dewar:** the double-walled and super insulating vessel that contains certain amounts of liquid nitrogen (LN2). Depending on the size of the dewar, the detector can be cooled for 12h till a week.
- **Cold finger:** the thick copper rod that transfers the temperature of the dewar to the crystal.
- **PT100:** The temperature of the crystal is monitored by measuring the PT100 resistance element. The PT100 is a calibrated temperature sensitive resistance component.
- **Sieve with Molecular getters:** The vacuum (< 10^{-6} mbar) inside the detector is maintained by the molecular getters. This is a chemical material that is able to capture remaining gas atoms inside the vacuum chamber. Different materials can be used for this purpose such as a carbon getter, zeolite or palladium.
- **Caddock:** If the vacuum deteriorates, the air close to the detector starts to condense which is a warning that the getter material is satisfied and thus the vacuum is no longer maintained. The detector is connected to a pump and is then heated. Therefore, the **caddock** is of great use. This is a resistance that is put in touch with the **cold finger** and in this way heats the cryostat to around 80°C. At these higher temperatures, the getter material will emit its stored gas atoms which are carried away by the pump (warming up the cryostat without a pump can cause an overpressure in the detector in such a way that the endcap can be damaged.
- **The motherboard:** this component contains the feed-back elements and is directly attached on the encapsulated crystal to minimise the distance between detector and pre-amplifier. As a result, a reduction of the electrical noise is achieved.

b) Doping

As explained in paragraph 3.3.1 c) The working principle of an HPGe detector and 3.3.3 Electronics: the p-n junction, it is important to dope the crystal in order to detect radiation. Doping is specified as the controlled implementation of impurities into the crystal. These impurities can take in interstitial or substitutional places into the crystal as shown in figure 31. For the sake of completeness, the two ways of doping are explained in this paragraph [10].

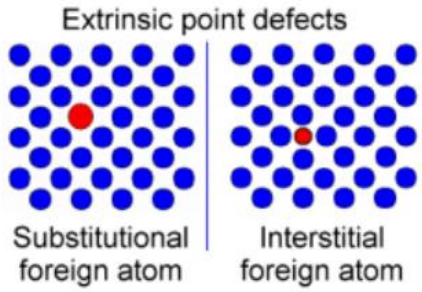

Figure 31: Implantation of impurities in a semiconductor crystal [10, p. 219]

A first option is to dope Si and Ge with elements from group V of the periodic table such as P, As, Sb. Since Si and Ge both belong to group IV, the atoms from group v carry an extra valence electron compared to Si and Ge. Thus, when implanted in the Ge or Si crystal, four covalent bonds take place while one free electron roams around in the bonding matrix. This is shown in figure 32. After multiple impurities are implanted, this results in an increase in conductivity of the crystal. The crystal is called a n-type semiconductor containing free, negative charged particles (electrons) and fixed positive charged particles (P) [10].

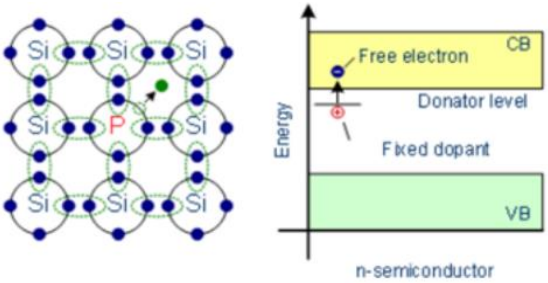

Figure 32: Atomic visualisation of an n-type semiconductor [10, p. 220]

A second option is to dope Si and Ge with elements from group III of the periodic table such as B, Al, Ga and In. Since Si and Ge both belong to group IV, the atoms from group III lack a valence electron compared to Si and Ge. Thus, when implanted in the Ge or Si crystal, three covalent bonds take place with the impurity atom. This is shown in figure 33. After multiple impurities are implanted, this results in holes 'travelling' through the crystal and the impurity becomes a fixed negative charge. The crystal is called a p-type semiconductor [10].

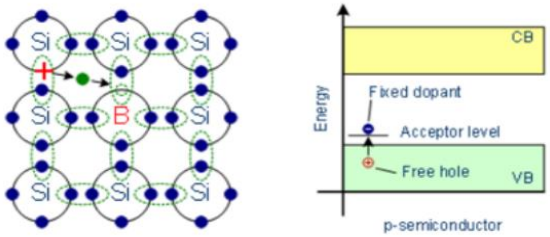

Figure 33: Atomic visualisation of a p-type semiconductor [10, p. 222]

c) P-n junction

Just like cooling, a p-n junction serves the purpose of eliminating the electron-hole pairs due to thermal excitation. A p-n junction is created by combining both an n-type and p-type doped part of a crystal with each other. This should be constructed from one crystal in order to eliminate deviations in the signal because of different physical properties at the border if it were to be constructed out of two crystals [51].

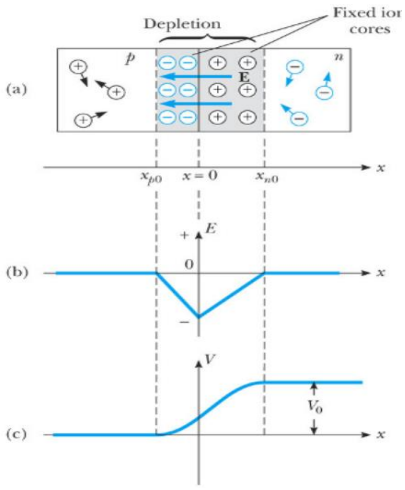

Figure 34: Working principle of a p-n junction [10, p. 227]

As shown in part (a) of figure 34, in the contactzone a gradient arises since diffusion of n in p-material and the reverse process that takes place. As a result of diffusion, recombination of the diffused electrons and holes with the majority of charge carriers in the other material happens. As a result, there is no longer neutrality in the contact zone. A layer of fixed charges is now present in this specific area without the presence of free charges. This zone now operates as an insulator. The separation of fixed charges creates an electric field (visible in part (b) of figure 34) which further prevents diffusion of electrons and holes to take place. Outside of the neutral zone, the sum of charges equals zero. The electric field leads to the presence of a potential difference over the neutral zone as is shown in part (c) of figure 34 [10].

The neutral zone in this design forms the sensitive region of the detector. Because of the absence of free charged particles, radiation detection via ionisation is possible here. Therefore, it is desired to increase this sensitive region. This is achieved by applying an external electric field, visualised in figure 35, forcing the free charged particles to move away from the centre and thus increasing the sensitive region for radiation detection. Another benefit of this configuration is that the few electron-hole pairs created by thermal excitation in this zone are immediately removed by the applied field, leading to a small but controlled leakage current. Last but not least, it is important to apply polarisation in the reverse direction as shown in figure 35. Polarising in forward direction would cause the charge-free zone to shrink, losing the advantage of dealing with thermal excitation. It would make the diode conductive and the current would increase exponentially with rising voltage which could damage the crystal [10], [51]–[53].

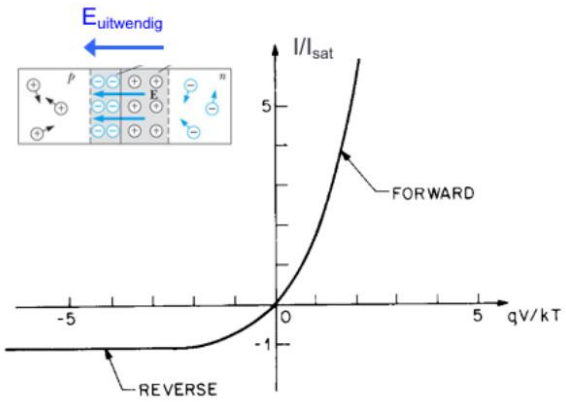

Figure 35: Polarisation in reverse direction and the current in function of applied voltage curve [10, p. 230]

d) Signal processing

Figure 36 shows the general components needed for signal processing. First, electrons and holes are produced by the interaction of ionising radiation with the semiconductor crystal as shown in figure 37. This creates a detector pulse. Then, this pulse is sampled using a quick digitizer with enough resolution to recreate the pulse. The result is shown in figure 38. The required methods are then used by a digital signal processor (DSP) to filter the pulse and retrieve the pulse height (as shown in figure 36). Implementing filtering mechanisms is very flexible when using digital signal processing. The software is easily modifiable [49], [52]–[54].

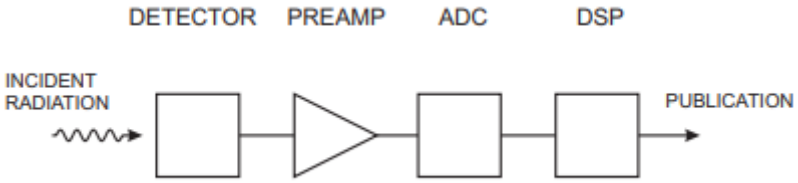

Figure 36: Block diagram of a detector readout using digital signal processing [54, p. 31]

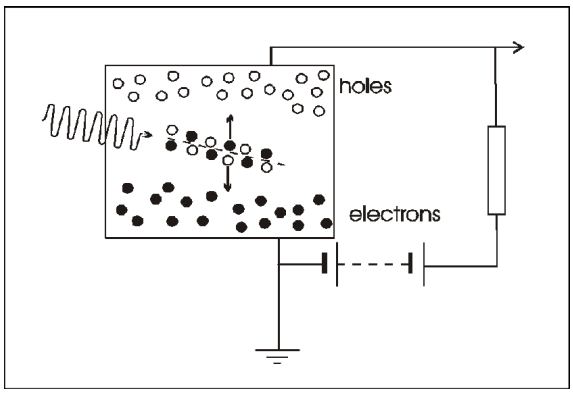

Figure 37: Principle of a semiconductor detector [46, p. 56]

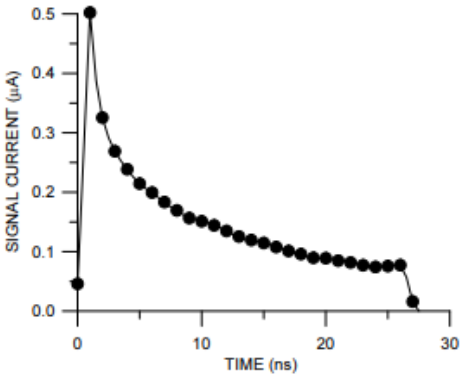

Figure 38: Sampling a pulse to allow digital processing. The pulse shown is the current pulse from a strip detector [54, p.31]

3.3.4 Software

A wide variety of software programs are used during the span of this thesis work. In this paragraph more insight on the purpose and working principles of these programs is given. Last but not least, while discussing EGSnrc as MC code, the basics of programming and the build-up of a detector computer model are explained. Examples of computer models of detectors made in the past are also provided as an introduction to paragraph 6. Optimisation/validation of detector Ge-T10 and 7. Optimisation/validation of detector Ge14.

a) Genie2000

Genie2000 is a comprehensive environment for data acquisition, display and analysis of alpha-particle and gamma-particle spectrometry data from Multichannel Analyzers (MCAs). Figure 39 gives an overview of the Genie2000 architecture. For more information about the Genie2000 architecture and software specifics, the following source provides a more detailed explanation about this [55].

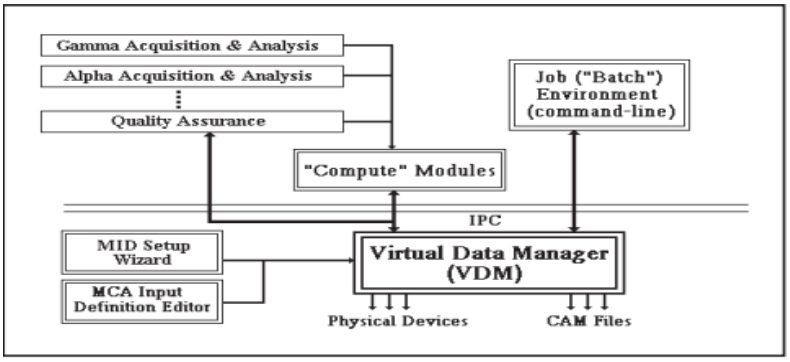

Figure 39: Block chain of Genie2000 architecture [55, p. 20]

For this work, it is of more interest to explain the practical use of Genie2000 when using it to analyse gamma-ray spectra. For this project, Genie2000 is of particular interest for 'processing' and analysing the spectra resulting from experimental reference source measurements. After a sufficiently long measuring time (a reference point is to collect at least 10.000 counts under FEP of interest so the relative counting statistical uncertainty is reduced to 1%), a gamma-ray spectrum is obtained (an example is given in figure 41). When analysing the spectrum a sequence consisting out of three different processes is applied. First of all, all the visible peaks (following a certain mathematical algorithm) in the spectrum are located automatically by Genie2000. Then, Genie2000 generates a fit for all located peaks which is essential for later processing purposes in GLysis (figure 40 represents a fitted peak). Since peak fitting is a complex process and the uncertainties must be minimised when calibrating a detector and setting up a computer model, the fit of FEPs of interest are all manually inspected, checked and (when necessary) improved. Things to look for are: good counting statistics under the peak (more than 10.000 counts), a good FWHM (Full Width Half Maximum) for the fit (a ratio in the range: 0.9-1.1 compared to the calibrated FWHM) and if there are no clear signs of other peaks besides the peak of interest in the residuals. If peaks are seen in the residuals, it is recommended to add other peaks manually at these indicated locations and check if the FWHM-ratio gets closer to 1. Such structures in the residuals can also be assigned to high counting statistics. In this case, no peaks should be manually inserted. The result of applying this sequence to the spectrum form the inputs for the reprocessing in GLysis [55]–[57].

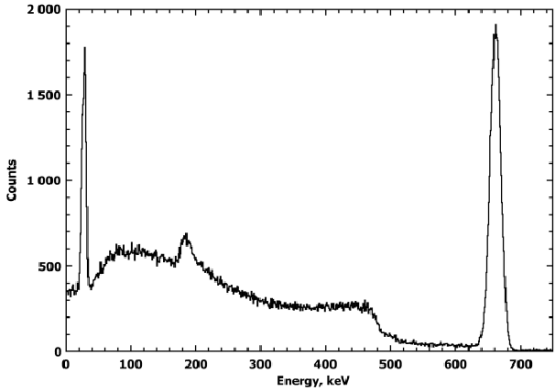

Figure 41: Gamma-spectrum of ^{137}Cs [56, p. 174]

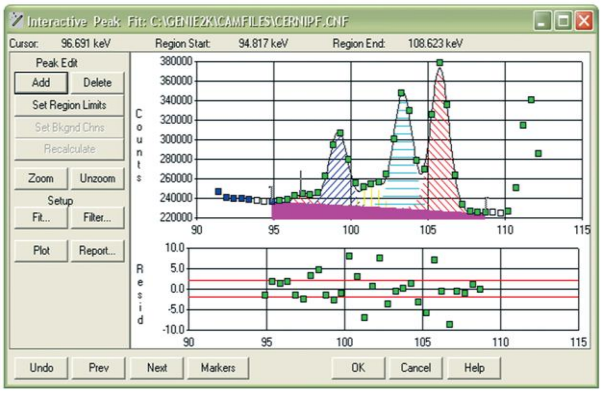

Figure 40: Interactive peak fit from Genie2000 [57, p. 1]

b) EGSnrc

A MC computer model is constructed, tested and validated for both the Ge-T10 and Ge14 HPGe detector in this thesis work. A MC simulation code is needed to carry out HPGe efficiency simulations. However, a model for the detector should first be constructed to carry out the simulations with. Figure 42 and 43 give a representation of the models of both the Ge-T10 and the Ge14 detector. These models and the adaptation of them is further discussed in paragraph 6. Optimisation/validation of Ge-T10 detector and 7. Optimisation/validation of Ge-14 detector for a more precise description of the code, I refer to the following manual: [58].

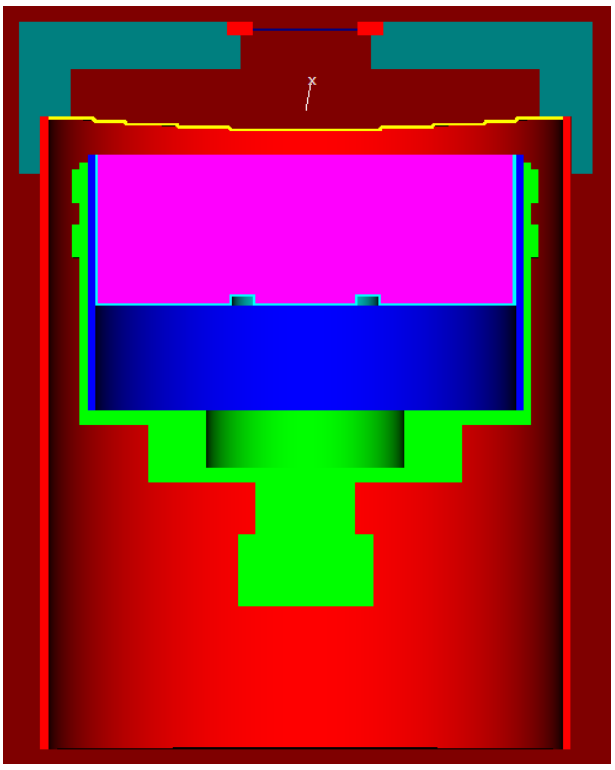

Figure 42: Model of the Ge-T10 detector with point source placed on a special holder on top of the detector

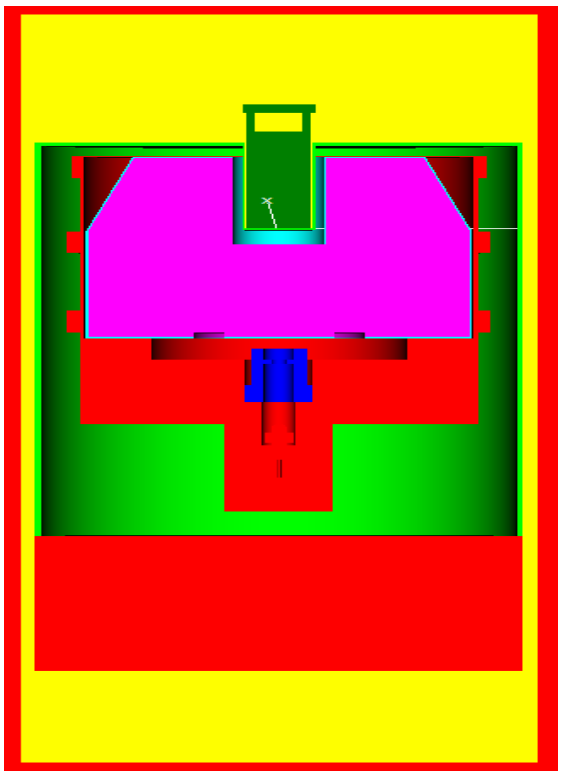

Figure 43: Model of the Ge14 detector with a vial inserted in the well

As for the MC simulation code, EGSnrc is chosen for this particular application at the JRC. EGSnrc is a general-purpose software toolkit that can be used to build Monte Carlo simulation for both electron and photon transport (for particles ranging in energy from 1 keV to 10 GeV). EGSnrc is used for a wide range of applications that utilise radiation transport physics to calculate specific quantities. From all different Monte Carlo codes, this one is used mainly in medicine for imaging or radiotherapy purposes. It is possible to calculate quantities such as absorbed dose, Kerma, particle fluence, and much more, with complex geometrical conditions. For this project EGSnrc is opted for over other codes such as serpent (mainly used in reactor physics neutron transport simulations) for its high-quality gamma-ray modelling which is necessary for gamma-spectrometry simulations. The main asset of EGS is its outstanding electron transport algorithms (down to 1 keV) and therefore fit for the work in this thesis. Besides that, the package HPGE3 is used. HPGE3 was developed by Guillaume Lutter at JRC-Geel especially for modelling HPGe-detectors using EGSnrc. The aim of HPGE3 is to estimate the detection efficiency of a sample and the detector configuration. This simulation code makes use of egs++ libraries, is written in C++ and is based on the EGS_AdvancedApplication class [58].

c) GLysis

Similar to the explanation of Genie2000, GLysis is explained in this paragraph with a focus on practical use rather than the theoretical working principles of this program. GLysis was developed by Guillaume Lutter (JRC-Geel) for calculating activities in Bq from gamma-ray spectrometry spectra in a way such that the user has much more freedom to see and steer calculations compared to commercial software. This approach does not fit all laboratories but is suitable for a reference laboratory like the RN-team of JRC-Geel. For this project, two major sets of input are required: (i) being the fitted spectra from the reference measurement and (ii) the MC model simulation files for the FEP and radionuclides of interest. Next, all the FEPs of interest are selected and the reference date and activities for all radionuclides are specified. Here the selection between useful and useless[1] FEPs is made by selecting the ones of interest. The values are compared for all major FEPs resulting in a plot of relative differences between model and experiment as shown in figure 44. This forms the basis for determining the most suitable MC model (the one that most closely matches the experimental values).

[1] A peak can be considered “useless” for calibration if, for example, there are non-negligible interferences from other peaks that are difficult to correct for or if there are uncertainties in decay parameters that are considered too large.

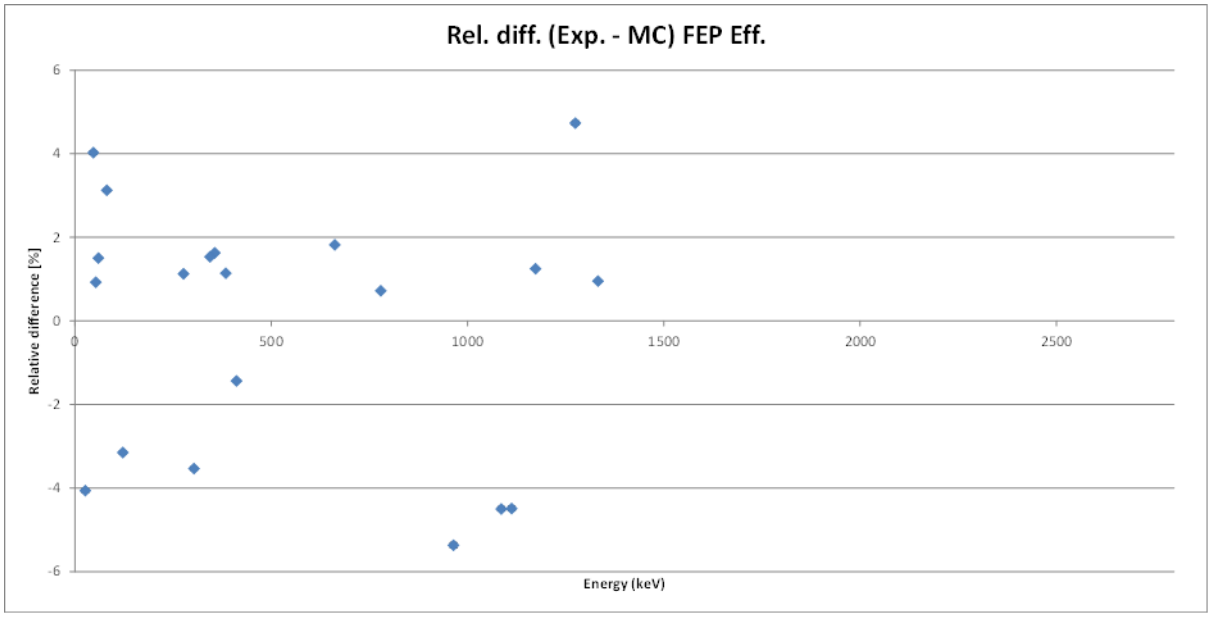

Figure 44: Relative difference plot obtained by combining the experimental reference source measurements and simulation results for different FEPs (this specific example is from detector GeT10)

3.4 gamma-ray spectrometry: efficiency calibration

For public safety it is of great importance to verify the radioactive composition of environmental samples which can contain NORM or non-natural radioactivity. Radioactivity levels should not exceed limitation values imposed by the European commission. Therefore, according to Articles 35 and 36 of the Euratom Treaty, the Member States are obliged to monitor the level of radioactivity in the air, water and soil and to report to the European Commission. In addition, the Euratom Treaty also obliges the Commission to verify the efficiency and operation of this monitoring. A common laboratory technique used for analysing samples containing gamma-ray emitting radionuclides is called gamma-ray spectrometry. Gamma-ray spectrometry makes use of High Purity Germanium (HPGe) detectors because of their exceptional resolution. In order to achieve a good performing HPGe detector, it is of great importance that these detectors are precisely calibrated and thus the efficiency is precisely determined. Note that spectroscopy is the study of radiated energy and matter to determine their interaction, and it does not create results on its own. Spectrometry on the other hand is the application of spectroscopy so that there are quantifiable results that can then be assessed. Equation 3 represents the basic equation of gamma-ray spectrometry, which shows how the activity of a particular radionuclide is determined based upon a gamma-ray spectra and the efficiency transfer method to determine the efficiency [1], [9], [59], [60] .

$$A=\frac{C_{TOT}-C_{Peak}^{Bkg}-C_{Continuum}}{\varepsilon_{REF}^{Exp}\frac{\varepsilon_{Sample}^{MC}}{\varepsilon_{REF}^{MC}}P_{\gamma}}e^{\lambda t_d}\frac{\lambda}{(1-e^{-\lambda t_m})}K_1K_2K_3 \quad (3)$$

3.4.1 Ways to determine efficiency

As already mentioned, it is important to determine the radioactive content and activity in samples by using the gamma-ray spectrometry technique with HPGe detectors. However, the obtained spectra on its own is not enough to recreate the original/actual value of activity of the sample. Obviously, decay corrections need to be made. In addition, the efficiency of the detector for the measurement of that specific sample needs to be obtained since a detector does not observe every single emitted gamma from the sample. Thus, in order to achieve a good performing HPGe detector, it is of great importance that these detectors are precisely calibrated and thus the efficiency is precisely determined. This can be done in various ways such as: experimental efficiency determination, MC efficiency determination and finally by the use of the Efficiency Transfer method. Later, it will be discussed how these different efficiency calculation methods are used to validate the MC computer model which in its turn is of great use to determine the specific efficiency of a sample measurement (this will be discussed in paragraph 6. and 7.) [1], [3], [44].

a) Experimental

The calibration can be carried out with an experimental approach, by using reference materials or standard sources. These reference sources have a well-known activity, geometry and composition. The efficiency can then easily be derived according to (somewhat simplified[2]) equation 4, compared to the basic equation, where C are the measured counts under the full-energy peak, t stands for the time measured (live-time), P is the fraction of which this decay path happens and gamma-ray in questions emitted (emission probability). The results from such a calibration can in turn be used to evaluate the radioactivity of unknown samples, which is necessary to live up to the obligations of the Euratom Treaty and for many other applications. This is only valid when these unknown samples have a similar composition and geometry as the used reference sources. Therefore, a directly practical limitation is implied on the use of gamma-ray spectrometry where calibrations are performed with reference sources, as it is not always possible to obtain suitable materials that closely match the samples which need to be characterised [1], [3], [44].

$$\varepsilon = \frac{C}{A * t * P} \tag{4}$$

a) Simulation

An alternative to counter these limitations is making use of Monte Carlo (MC) simulations for the HPGe detector. The simulated detector response of the HPGe detectors can be used to derive the full-energy peak efficiencies and therefore operate as an 'alternative' to the use of reference sources, to carry out calibration of the detector. And in its turn, the results from such a calibration can again be used to evaluate the radioactivity of unknown samples. By making use of the MC, there is no longer the geometry limitation encountered while working with reference sources. Thus the MC code is used for a wide range of material compositions and source geometries, which eliminates the need for having a specific geometry reference material for each encountered sample. The disadvantage of such MC based efficiency determinations is the fact that even the smallest deviation in the computer model (small difference between the modelled thickness of the deadlayer compared to the actual thickness, wrong defined material, etc.) ensures that all determined efficiencies for the different energies for different full energy peaks deviate from their true values. In order to counter such deviations in the EGS computer model, the EGS model for the HPGe detector is run by varying a few parameters to establish optimal agreement between the model and the experimental (this is an important part to fulfil before using the model as a calibration tool for sample measurement). The key parameters to vary are: crystal position, top deadlayer thickness and side deadlayer thickness. The so obtained MC efficiency values for different full-energy peaks (and different parameter values) are compared to the experimental obtained efficiencies. The best fit determines the setting and adjustment of the parameters in the computer model. This validation of the MC computer model is further discussed in paragraph 6. and 7. [3], [44].

[2] In this formula excluding decay corrections, angular correlations, deadtime corrections and summing corrections.

b) Efficiency transfer (ET)

Last but not least, there is the option to carry out the calibration of the detector for sample measurements using the experimental reference source measurements and the MC model of the detector. As mentioned, the experimental reference source measurements are very precise when a similar geometry as the sample can be obtained (which is not always possible or desired depending on the specific geometry of the sample and the institute's inventory of reference material geometries). In cases where this forms a practical obstruction, the MC model of the detector can be used to carry out the calibration for sample measurements. As the model on its own may still entail deviations from the actual detector (even though the model has been tested by varying different parameters (see paragraph 6 and 7)), determining the efficiency in this way is extremely sensitive for mistakes in the MC model of the detector (which are inevitable). Therefore the Efficiency Transfer Method is often opted for to determine the efficiency of a certain sample measurement. This technique relies on combining both the experimental reference source measurements (and thus the experimental efficiencies) and the MC model determined efficiencies. The FEP efficiency of a sample measurement is then defined as in equation 5 (without introducing coincidence summing. The main advantage of this technique is that it is able to eliminate mistakes in the MC model since the two values obtained by the model appear in a ratio [3], [61]–[63].

$$\varepsilon_{sample} = \varepsilon^{exp}_{ref} = (\varepsilon^{MC}_{sample} / \varepsilon^{MC}_{ref}) \quad (5)$$

3.5 Calibration of HPGe detectors in the literature

After describing the fundamentals such as: gamma interactions, the basic parts of a gamma-spectrum, the working principle of an HPGe detector, basics of gamma spectrometry, etc. which form the foundation of this work, this chapter aims to situate the project of calibration of HPGe detectors more in existing literature. Specific questions such as the following are discussed: what is the current state of research about calibration of HPGe detectors? Which new methods are on the rise? How does my research compare with methods currently under investigation? What things emerge from previous studies that are of great importance to take into account for this project?

3.5.1 Internal research papers

First of all, the foundation for this project lies in the previously conducted efficiency calibrations of other HPGe detectors at JRC. Similar to this project, other acquired HPGe detectors at JRC needed a good working model. Since similar programs and detectors were involved compared to the Ge-T10, this contains valuable information and thus a similar working principle can be followed for the calibration of the Ge-T10. As described in the introduction of this project, three different parameters play a role within the model: crystal position, Side deadlayer thickness and top deadlayer thickness. Besides that, such a calibration can be performed at different distances or with volume sources. In the two earlier reports, different approaches were taken concerning which parameter to change first and by how much. One report is about the efficiency calibration of gamma detector Ge-T2, executed by Patric Lindahl. A point source efficiency calibration was performed at three different distances (2.45 cm, 13.72 cm and 14.47 cm). First of all, the crystal position and the side deadlayer thickness were changed and finally the top deadlayer was changed [61].

This study revealed a noticeable difference when performing the calibration for different source distances. The relative difference between the model and experimental efficiency was lower for longer distances of the source to the detector. This reason for this is not given in the report, but it is later ‘discovered’ in this project work. It is concluded that the main changes in relative differences were found by changing the side deadlayer thickness and the crystal position. This is due to the difficulties in determining the correct values for these parameters from the radiography of the detector. Changes in the top deadlayer were not that effective. However, this had a more noticeable effect on low energy calibration points. Another important observation is the fact that some calibration points of different ^{152}Eu gamma lines and ^{241}Am gamma lines were not in line with other calibration points from different radionuclides used. This was reported as not fully understood, but it is suspected to be because of the need for revision of the ^{152}Eu decay scheme or that the summing code used for ^{152}Eu in the model may have imperfections [61].

Secondly, Elisabeth Wieslander performed the calibration of detector Ge-T4 at the JRC. A similar approach was done here. A similar conclusion was made about the changes in all the different parameters. Here the fact also surfaced again that for other source distances it was difficult to have an agreement for the results of all these distances. There was again a noticeable deviation. However, this time the difference was lower, but it was also performed with smaller distances compared to the calibration of the Ge-T2 [62].

Lowie Brabants performed a similar research study where the efficiency of a coaxial p-type HPGe detector from Canberra was modelled. The main difference with this project is the fact that TOPAS MC Software was used for this research instead of the here utilised EGSnrc MC Software. It differs even more from the previous two studies by using three different source geometries to validate the model. Volume sources are described and used for this which is also done in this project. Again, deviations for the ^{152}Eu gamma-rays were observed. This is linked to the experimental error due to the small P_y and the interference of the 686.61 keV gamma-ray emission of ^{152}Eu [3].

These results will be a starting point for carrying out this project and are kept in mind when assessing own results.

3.5.2 External research papers

The previous mentioned studies were performed at the JRC. In order to be more complete and expand the scope of this thesis, some publications about the efficiency calibration topic are investigated.

A first paper that was consulted was about 'efficient calibration for imperfect computer models'. More in general, this paper states the importance of the calibration of a computer model (not only a computer model for a detector but all computer models). It emphasis on the fact that many computer models contain unknown parameters. In order to fix this in an efficient way, these parameters need to be estimated and updated by using physical observations. However, before doing a calibration and validation of a computer model to evaluate certain parameters, it is important to think about which parameters could be wrong and why that might be. This will help tremendously in the fluency of the calibration process. The basic idea of calibration is stated to be to find the combination of the model parameters, under which the computer outputs match the physical responses. Translated to this thesis, it is known which parameters are not precisely known by the manufacturer or that change over time: thickness of the deadlayer, thickness of the endcap and crystal position. Change in thickness and form of deadlayer has already been mentioned in paragraph 3.3.1 HPGe detector, based on [40]–[45]. Change in crystal position can be explained by the fact that during the manufacturing of the detector, no cooling is implemented. However during the operation of an HPGe detector, cooling is necessary in order to have good radiation detection (see paragraph 3.3.3 Electronics). Lower temperatures entail shrinkage of detector components (material specific). This is most prominent in the cold finger connecting the detector and the cryostat. This may lead to the crystal being positioned lower than originally during manufacturing. Change in thickness of the endcap is explained in paragraph 6 Optimisation/validation of detector Ge-T10. Besides that it is mentioned how an important part of the calibration of computer models is to tackle the model uncertainty. Most physical models are built under certain assumptions or simplifications, which may not hold in reality. As a result, the computer output can rarely fit the physical response perfectly, even if the true values of the calibration parameters are known [64].

Another paper that was consulted is about 'Simplified efficiency calibration methods for semiconductor detectors used in criticality dosimetry'. This article is of great value since it also carries out an efficiency calibration of an HPGe detector, but compared to this thesis, not to calibrate a computer model of a detector. A multi-nuclide calibration source containing ^{60}Co,

^{241}Am and ^{137}Cs is used for the efficiency calibration. Even though, this calibration is about the detector itself and not the computer model, it still entails useful information applicable to this thesis. It contains information about measuring calibration sources which is also part of this project. It is stated that calibration of the detector are often performed by MC simulations. However, in this case it is opted for to use calibration sources since the MC simulations require a model of the detector which is quite time consuming when not already available and detailed knowledge of the internal structure of the detector and its composition materials is needed. It is stated that gamma spectroscopy system efficiency calibrations are typically determined by measuring a source containing several radionuclides of known energy (in the range of calibration interest) in a geometry that is as close as possible to the samples we would like to measure later on [65].

A next paper that contained interesting information for this thesis is called 'A detailed procedure to simulate an HPGe detector with MCNP5'. Besides the fact that another simulation code is used (MCNP5 instead of EGSnrc in this thesis), most of the procedure is till applicable to this work. The detector of which the computer model is discussed in this paper is also manufactured by Canberra and shows many similarities to the Ge-T10. Figure 45 shows a schematic representation of the 45% HPGe detector. This paper starts by giving a similar explanation to 3.4.1 Ways to determine efficiency. Using the Monte Carlo method is often easier and certainly cheaper to determine the detector's response curves compared to the experimental way where all sorts of different geometries of calibration sources are needed. Another difficulty is the peak sum effect. These events affect the activity results and need to be taken into account. This effect is not dependent on the activity of the source. By having a good working computer model, the efficiency of another sample can be easily determined by changing the code of the computer model after which MC simulations are done. This work represents a detailed description of the procedure to simulate and calibrate models of co-axial HPGe detectors. Therefore, experimental measurements were carried out won an HPGe co-axial gamma-X detector, manufactured by Canberra. Several radionuclides were measured, covering the 46 keV – 1332 keV energy range. The source have different origin than the sources used in this thesis (here it was from the Brazilian Ionising Radiation Metrological Laboratory (LNMRI). In order to carry out detector simulations, a model was constructed based on manufacturer data and own measurements, see [66] for specifics. The importance of the correctness of the deadlayer is emphasised in this paper. It impacts the efficiency values, especially for low energy gamma-ray's. For them to be able to carry out precise simulations, they wanted to get accurate values for the deadlayer. Therefore, an ^{241}Am source (suitable because of it low energy gamma-rays) was measured and simulated, the two efficiency values were compared after which the deadlayer thickness was adjusted accordingly. After that, ^{137}Cs was used to confirm (validate this change). Finally, a maximum deviation of less than 9% difference was achieved [66].

.

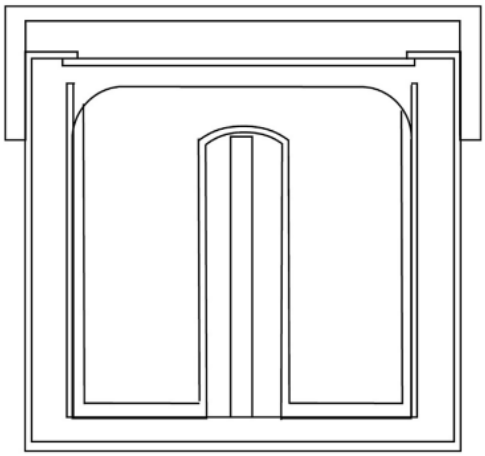

Figure 45: Output of the MCNP5 computer code relative to the described geometry used as input. The detector was described along the x axis and the centre of the base of the crystal was positioned at 0,0,0 (x,y,z) [66, p. 36]

Compared to this thesis work, this is similar to our optimisation process of the computer model of the Ge-T10. As was seen in previous papers ([40]-[45]) and discussed in 3.3.1 HPGe detector, indeed the thickness of the deadlayer is an important parameter for lower energies which can change in thickness and form over time. However, here only one parameter is taken into account for possible divergences between experimental and simulated data. For example, crystal position may also impact efficiency values for lower energies. Therefore in this thesis, multiple parameters are varied in the optimisation process of the computer models. However, it was mentioned that low energy photons mainly interact closer to the crystal's surface, for this reason, some of the secondary electrons can deposit part of their energy in the deadlayer and not be recorded. In order to account for this process, both photons and electrons must be considered in the simulation (which is also the case for EGSnrc used for this thesis, EGSnrc has the best electron transport algorithms out of all MC codes).

Finally, a similar paper dating back to 2012 was investigated. The title of this paper is 'HPGe well detector calibration procedure by MCNP5 Monte Carlo computer code. Compared to the previous paper, the procedure is now about an HPGe well-detector (and thus similar to the Ge14 in this thesis) which is shown in figure 46. Again the paper starts with explaining the need for environmental monitoring and a good working computer model of an HPGe detector in order to be able to determine the efficiency for sample measurements by MC simulations instead of the experimental way (calibration source measurements). Therefore, the detector's sensitive volume (making and optimisation of the model) was determined by comparison of simulated and measured spectra by using three point sources (^{241}Am, ^{137}Cs and ^{60}Co). Again the focus was on the thickness of the deadlayer for all crystal surfaces. The optimised model was then validated by using two volumetric sources, one placed inside the well and one on top of the well. Again, only the thickness of the deadlayer was varied (this time both the side deadlayer and the inner-deadlayer (deadlayer in the well). Finally, a maximum deviation of less than 10% difference was achieved [67].

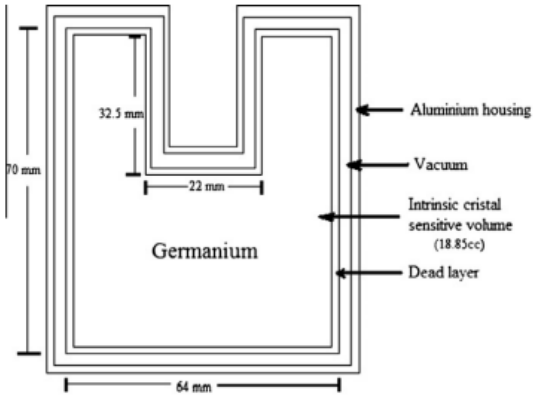

Figure 46: Schematic figure of HPGe well-detector cross section [67, p. 214]

From this literature study, the results will be a starting point for carrying out this project and are kept in mind when assessing own results. Besides that, it was clear that the last mentioned papers were less in depth on this method and often carried other objectives compared to efficiency calibrations performed at the JRC. That is why a procedure similar to [3] is chosen (explained in 5.1.3 and 5.2.3)

4 Objectives and hypotheses

In recent years the use of computer simulation has helped to improve accuracy, and robustness of measurement results. A more specific example of its utility lays in the analysing of samples containing gamma-ray emitting radionuclides. As discussed, following the Euratom treaty, the member states need to carry out monitoring of radioactivity in the environment in order to protect the people and the environment. Amongst its many tasks, JRC is in charge of varying the quality and equivalence of those measurements. For analysing samples, three different techniques were discussed to determine the efficiency for the sample measurement in 3.4 Gamma-ray spectrometry: efficiency calibration. The most precise technique is called the efficiency transfer method which makes use of a good working computer model of the concerning HPGe detector. It was discussed how it is possible that parameters such as crystal position, thickness of the deadlayer and thickness of the endcap given by the detector manufacturer are not precisely known or can change over time. Therefore, in order to develop a good working computer model of a detector, it is very important to carry out efficiency calibration measurements, and adapt these parameters accordingly.

The goal of this Master thesis is to test, develop and validate computer models for a coaxial HPGe detector located in the above ground (RADMET) lab, the Ge-T10 detector and one HPGe well-detector in the underground research facility HADES, the Ge14 detector. It is desired to have the relative difference in efficiency between experimental data and computer model as low as possible for all FEPs of the calibration sources. In general, it is desired to be better than 5% for all radionuclides. A statistical uncertainty analysis should be conducted including the following uncertainties on measurement and simulations: Calibration source activity, gamma intensity probability, experimental counts, measurement time, simulation uncertainty and last but not least coincidence summing correction. After this process, the computer model for the Ge14 is used in an application project linked to determining the distribution of radiocaesium in large wild mammals (wolves and bears) in collaboration with the Ruder Boskovic institute in Zagreb, Croatia.

It is expected to have lower relative efficiency difference for the Ge14 than for the Ge-T10 detector since a well-detector has higher efficiency for measurements (therefore, any relative difference between experimental data and computer model is lower). According to the literature study, see 3.5 Calibrations of HPGe detectors in the literature, deviations in the calibration points for ^{152}Eu are expected to be seen. For the measurement project, ^{137}Cs is expected to be present in different organs (remaining from the Chernobyl nuclear accident in 1986), but the question is in which organs will it be detectable.

5 Material and method

5.1 Ge-T10 specifics

This chapter discusses the materials used more specifically in context of the HPGe detectors used for this thesis: one coaxial HPGe detector located in the above ground (RADMET) lab, the Ge-T10 detector and one HPGe well-detector in the underground research facility HADES, the Ge14 detector. Hereby the characteristics of both the Ge-T10 and Ge14 detector are further explained.

5.1.1 Type of HPGe detector and location

Figure 47: External view of the Ge-T10 detector

Figure 48: Look inside the shield of Ge-T10 detector

The Ge-T10 is a coaxial HPGe detector constructed by Miron (Canberra) and is located in the above ground (RADMET) lab at the JRC, Geel. Figure 47 and 48 visualise this detector. It is a so-called Broad Energy Germanium (BEGe) detector. The Mirion BEGe detector cover the energy range of 3 keV to 3 MeV. The resolution at low energies is equivalent to that of their Low Energy Ge (LEGe) detectors and the resolution at higher energies is comparable to that of good quality coaxial (SEGe) detectors. More specifically, the BEGe detector has a thick shape which enhances the efficiency of the detector below 1 MeV for all sorts of typical sample geometries. It is exactly this energy range that is the most important for routine gamma analysis. In addition to higher energies, the BEGe detector exhibits lower background than typical coaxial detectors because its shape is not as long as corresponding coaxial detector. Last but not least, the BEGe detector is designed with an electrode structure that enhances low energy resolution and is fabricated from select germanium having an impurity profile that improves charge collection (thus peak shape and resolution) at higher energies.

5.1.2 Detector specifications

Table 2: Physical Characteristics Ge-T10

Active diameter	80.7 mm
Active area	5000 mm^2
Thickness	31.6 mm
Distance from window (outside)	5.5 mm
Window thickness	0.6 mm
Window material	Carbon epoxy

Table 3: Electrical Characteristics Ge-T10

Depletion voltage	(+) 3000 Vdc
Recommended bias voltage Vdc	(+) 3500 Vdc
Reset rate at recommended bias	/
Preamplifier test point voltage at recommended bias	-0.7 Vdc
Preamplifier output polarity	Neg.

Table 4: Resolution and Efficiency Ge-T10 (Amp time Cte: 4 us–7.2 us Rise Time, 0.8 us Flat Top)

Isotope	^{55}Fe	^{57}Co	^{60}Co
Energy (keV)	5.9	122	1332.5
FWHM (eV)	352	619	1795
FWTM (eV)	/	1137	3387

5.1.3 Calibration method

To optimise and validate the computer model of the Ge-T10 HPGe coaxial detector, the following working scheme is applied. Firstly, several point calibration sources (with known activity), present at the JRC, are measured on the Ge-T10 detector: ^{152}Eu, ^{210}Pb, ^{22}Na, ^{133}Ba, ^{60}Co, ^{137}Cs and ^{241}Am. The average uncertainty given by the producer is about 1.5%. The producer of these point sources is PTB (Physikalisch-Technische Bundesanstalt, Germany) and for the volume sources it is CMI (Czech Metrology Institute, Czechia). Following paragraph 3.5 “Calibration of HPGe detectors in the literature”, it was chosen to start the calibration process by measuring the calibration sources on the endcap. Later on, it will be discussed whether this was the most optimal starting point. The obtained gamma-ray spectra are then analysed in Genie2000. Different useful FEPs are then selected, fitted and checked. Simultaneously, the original computer model of the Ge-T10 detector is used to perform simulation with the software package EGSnrc for the same radionuclides and FEPs. Now both experimental and simulated efficiencies are collected, a comparison is made between both corresponding values in GLysis. Based on the comparison of the efficiencies originating from simulation with the original model and the experimental efficiencies, targeted changes are made to the model in order to minimize the relative efficiency difference for all FEPs. This is done by changing several parameters that are possible to not be precisely known by the manufacturer or that can change over time (and therefore can be adapted). More specific, the following parameters are played with: Crystal position under the endcap, thickness of the side deadlayer and thickness of the endcap. The reason for their change was shortly explained in 3.5.2 External papers. When the final model for that specific source-detector distance (on endcap) is obtained, it is validated at different source-detector distances and for volume source measurements. The measurements of the point sources are performed on three different source distances: on the endcap, at 4 cm distance and at 10 cm distance. Besides that 4 different volume sources are used. If the validation process indicates a difference between simulations and experimental, then this is an indication to repeat the process, adjusting the model further until the model gives an appropriate result for each situation (iterative process).

5.2 Ge14

5.2.1 Type of HPGe detector and location

Figure 49: View of the shield of the Ge-14 detector

Figure 50: View inside the shield of the Ge-14 detector (the well is seen as the circle at the centre)

The Ge14 detector is an HPGe well-detector, located in the underground research facility HADES. The Ge14 detector was is the first ultra-low background point contact well-detector in the world (the first SAGe detector optimised for an underground laboratory). Figure 49 and 50 visualise this well-detector. The biggest advantage of this Ge14 well-detector is the fact that its resolution is better than that of a normal well-detector. This is due to several factors: a well-detector can be made in such a way that the critical deadlayer strip in the well itself is small (small Li diffusion layer); in the past, for flat detectors, it was not possible to make big crystal detectors since charge collection had to be possible. By constructing point contacts, higher electric fields can be achieved so charges are collected quicker (better resolution) and the crystal can be made bigger (better efficiency).

5.2.2 Detector specifications

Table 5: Physical Characteristics Ge14: Coaxial one open end, closed end facing window (geometry)

Diameter	90.5 mm
Active volume	483 cc
Length	85 mm
Distance from window (outside)	6.5 mm
Crystal well depth	41 mm
Crystal well diameter	21.5 mm

Table 6: Electrical Characteristics Ge14

Depletion voltage	(-) 3500 Vdc
Recommended bias voltage Vdc	(-) 4000 Vdc
Leakage current at recommended bias	0.01 nA
Preamplifier test point voltage at recommended bias	-0.7 Vdc

Table 7: Resolution and Efficiency Ge14 (With amp time constant of 4 us – 7.2 us Rise Time, 0.8 us Flat Top)

Isotope	^{57}Co	^{60}Co
Energy (keV)	122	1332
FWHM (keV)	.738	2.08
FWTM (keV)		3.86
Peak/Compton		80.9:1
Rel. Efficiency		118.6%

5.2.3 Calibration method (nog verder uitbreiden)

To optimise and validate the computer model of the Ge14 HPGe well-detector, a similar working scheme to the one for the Ge-T10 is applied. Firstly, experimental calibration source measurements are performed. Since the Ge-14 is located at HADES personal measurements would be difficult since access needs to be granted. Therefore, previous measurements of calibration sources on the detector are used. More specifically, the CMI5 volume source is used to carry out the calibration and the CMI4 volume source will be used to carry out the validation of the optimisation. The average uncertainty given by the producer is about 1.5%. The producer of the volume sources is CMI. Again, the gamma-ray spectra are then analysed in Genie2000. Different useful FEPs are then selected, fitted and checked. Simultaneously, the original computer model of the Ge14 detector is used to perform simulations with the software package EGSnrc for the same radionuclides and FEPs. Now both experimental and simulated efficiencies are collected, a comparison is made between both corresponding values in GLysis. Based on the comparison of the efficiencies originating from simulation with the original model and the experimental efficiencies, targeted changes are made to the model in order to minimize the relative efficiency difference for all FEPs. Similar parameters compared to the Ge-T10 are changed: Crystal position, thickness of the side deadlayer and thickness. A difference is that also the thickness of the well-deadlayer is changed (Ge14 is a well-detector). This process starts with using the CMI5 for optimising the model. When the final model is obtained, the validation is carried out by using the CMI4 volume source. If the validation process indicates a difference between simulations and experimental, then this is an indication to repeat the process, adjusting the model further until the model gives an appropriate result for each situation (iterative process).

6 Optimisation/validation of detector Ge-T10

This chapter displays the applied working method, difficulties and results of the optimisation and validation of the Ge-T10 detector. All results essential for drawing a conclusion are included in this chapter. Interim results are presented in Appendix A: Relative efficiency difference graphs of Ge-T10. From here on, under all graphs representing relative efficiency difference there will be noted what the average value is as well as the absolute standard deviation (each in percentage %).

6.1 Original model

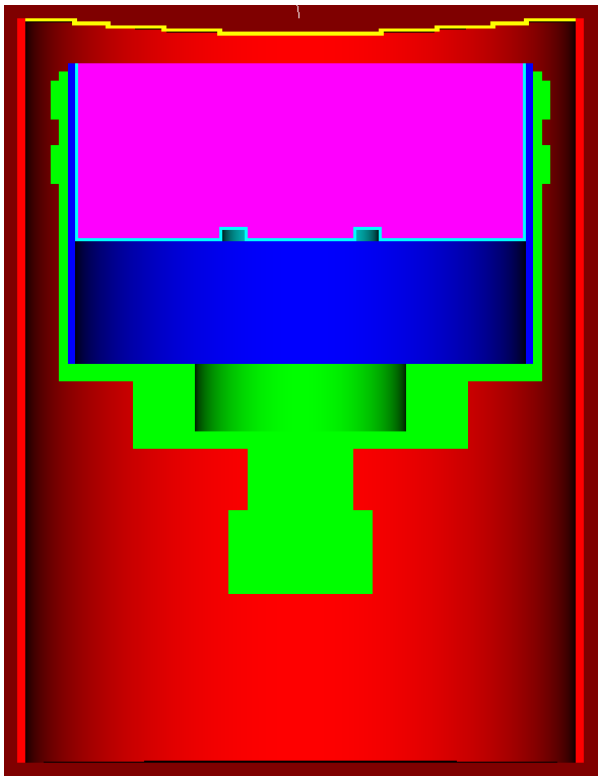

Figure 51: Model of the Ge-T10 detector

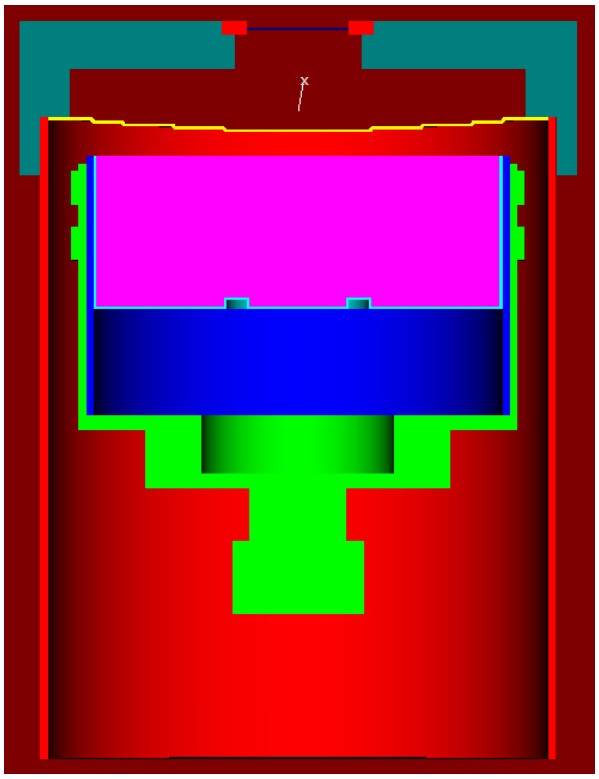

Figure 52: Model of Ge-T10 detector with point source

Starting off with measurements of point source on the endcap, the original model was adapted to fit this geometry. Figure 51 visualises the original model based on the manufacturer's data of the detector, before any optimisation was made. Figure 52 represents the same model but adapted for point source measurements/simulations.

This 'original' model was the simulated for the same radionuclides and FEPs as measured. After comparison in GLysis with measurement results on the endcap this resulted in a relative efficiency difference plot as shown in figure 53. A general trend can be seen in this graph, namely that the relative difference efficiency points for all energies are below zero, going down to -11%. This indicates that the simulated MC efficiencies overestimate the actual efficiency values.

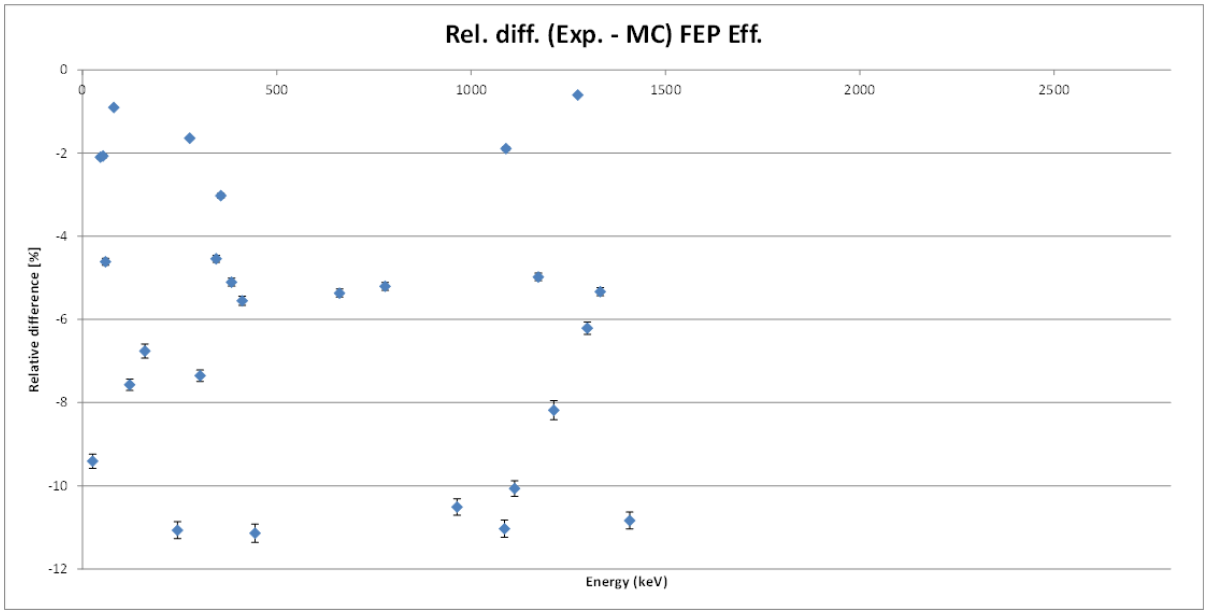

Figure 53: Relative difference in efficiency between experimental data and simulations for point sources on endcap (data from the original computer model based on manufacturer's data of the detector). An average of -6.29% and a spread (absolute standard deviation) of 3.10%

6.2 Working on optimising the model

In order to lower the simulated efficiency, one of the following parameters is adapted in the model: Crystal position, thickness of the top deadlayer, thickness of the side deadlayer and thickness of the endcap. The most suitable parameters to inflict a general (for all energies/FEPs) upwards or downward motion are the crystal position and the thickness of the side deadlayer. Simulations were performed in which the crystal position in the model was adapted ranging from - 1 mm to - 5 mm. simultaneously, the side deadlayer was adjusted, ranging from 0 mm to 1 mm. It is likely that the actual geometry is going to be a combination of both. This whole optimisation process is described in appendix (Appendix A) and resulted in a computer model that resulted in the relative difference graph shown in figure 54.

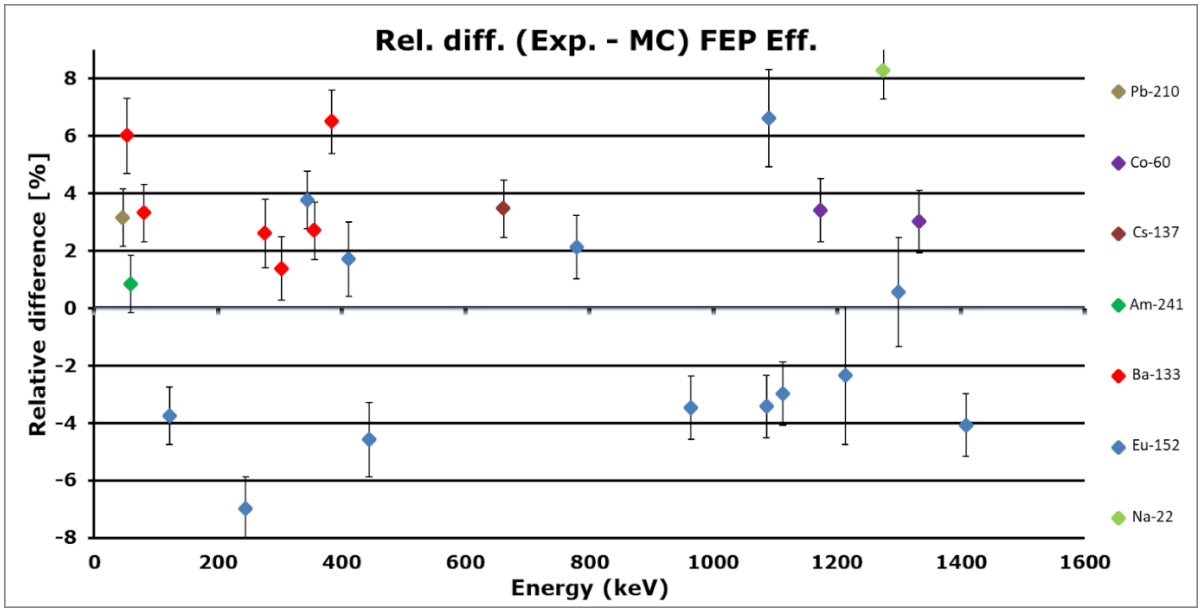

Figure 54: Relative difference in efficiency between experimental data and computer model for point sources on the endcap. The uncertainties represent the counting statistical uncertainty (~1%), uncertainty of calibration sources (~1.5%) and coincidence summing correction is included (uncertainty on measurement time is negligible). This is displayed at the level of one sigma. The average is 0.92% and an absolute standard deviation of 3.79%

However, subsequently, the same process was carried out at the second source distance (4 cm). The data obtained at 4 cm is shown in Figure 55. Finally the same process was repeated for sources measured at 10 cm and that data is presented in Figure 56. By comparing figure 55 and figure 56, it can be seen that the spread on relative difference between experimental and simulated FEPs efficiencies (using the same model) is gets lower with increasing sample-detector distance; This is due to factors such as uncertainties is source alignment and coincidence summing corrections etc. gets smaller at larger distances to lower the impact of these phenomena and to draw a better conclusion concerning the best fitting computer model, it was chosen to start at the highest possible source distance (10 cm) and validate the best fitting model there at the shorter source distances (4 cm and on endcap).

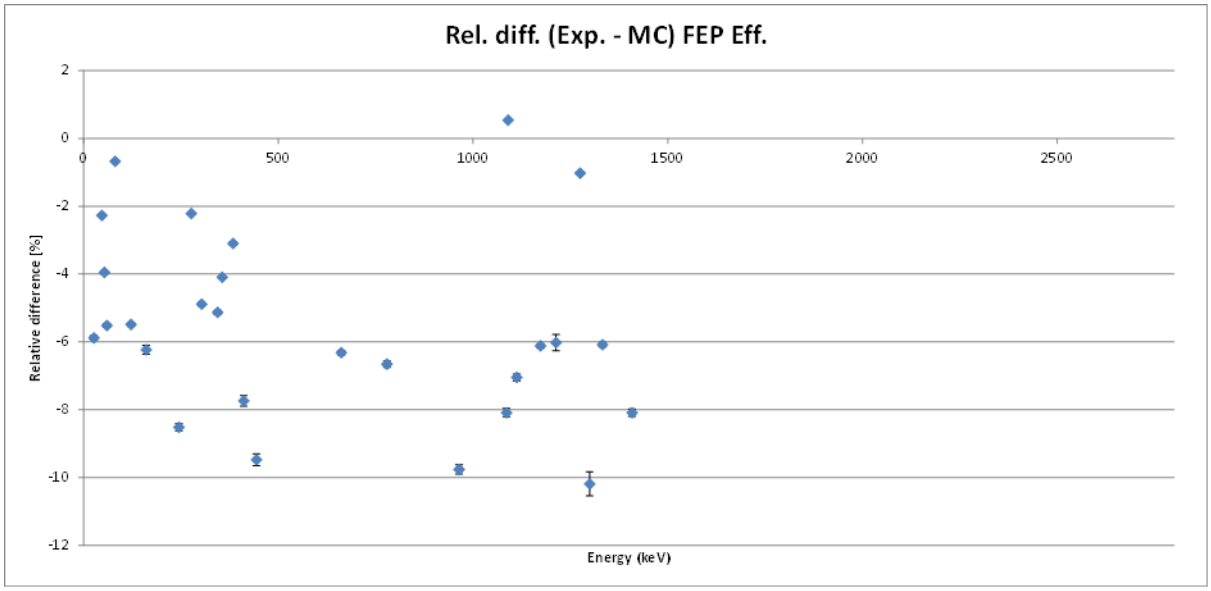

Figure 55: Relative difference in efficiency between experimental data and simulations for point sources at 4 cm distance. Average of -5.13% and a spread of 2.66%

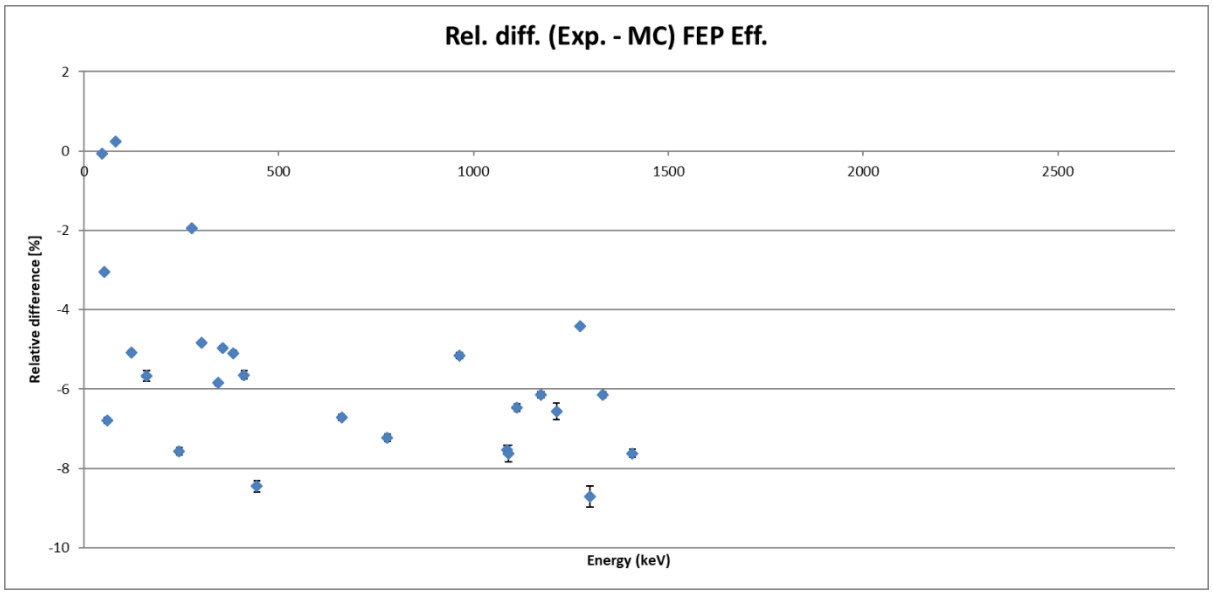

Figure 56: Relative difference in efficiency between experimental data and simulations for point sources at 10 cm distance. Average of -4.88% and a spread of 2.28%

6.3 Final version of the model

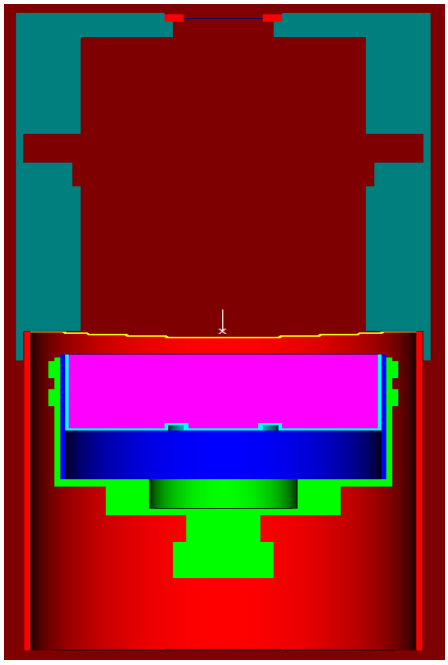

Figure 58: Final model of Ge-T10 at a source detector distance of 10 cm

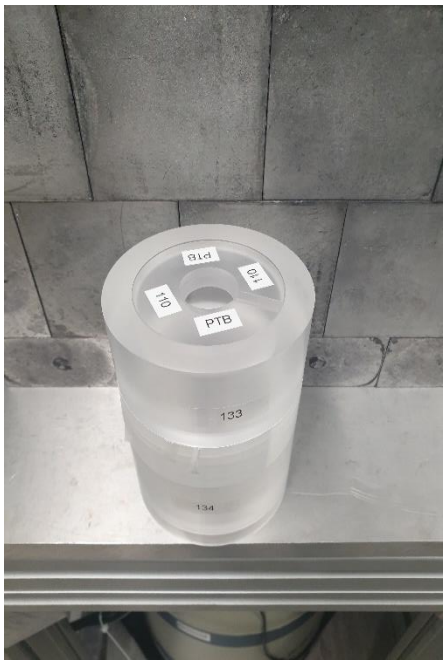

Figure 57: Source holders to have 10 cm distance

Following the previous paragraph, a final version with an acceptable difference in efficiency between experimental and simulations was achieved based on measurements at 10 cm (see appendix A). This was done by moving the crystal down by 1.5 mm, increasing the thickness of the side deadlayer by 0.5 mm and decreasing the thickness of the endcap by 0.1 mm. The actual shape of the endcap is curved. In the model this was approximated by several steps. At the points where the model makes steps the incoming radiation takes a longer path inside the endcap. This justifies a slight decrease in general thickness of the endcap. Figure 58 shows the model at distance 10 cm. Figure 57 shows the source holders used. The result of the comparison between experimental and simulation is shown in figure 59. It can be seen that the mean deviation is -0.29% with a maximum relative difference (spread around zero) of 3%. Besides the numerical results, it is important to perform a statistical analysis to determine whether the results can be further improved, or whether certain radionuclides appear as outliers. Therefore, different uncertainties were emerged to get to the uncertainty of the difference between experimental and simulation. Following uncertainties were included: Calibration source activity, gamma-ray emission probability, experimental counts, measurement time, simulation uncertainty and last but not least coincidence summing correction. All these factors combined are visualised in figure 55-9 as one sigma (combined standard uncertainty). 68% of all points cross zero at one sigma, 92% of all points cross zero at two sigma. This is very much in agreement with statistical theory (68% for 1 sigma, 95% for 2 sigma). No real outliers are present in the graph. However, this analysis is not meant to deliver an exclusionary conclusion whether this model is ‘right’ or ‘wrong’. A computer model of a detector is not the real detector and will always contain deviations unless one makes a model at molecular or even electron levels as charge collection is the crucial process of the functioning of an HPGe-detector. On the other hand, it does give an indication of how well the computer model replicates reality. Taking into account the uncertainty analysis, it is close to impossible to further improve the model for this source distance.

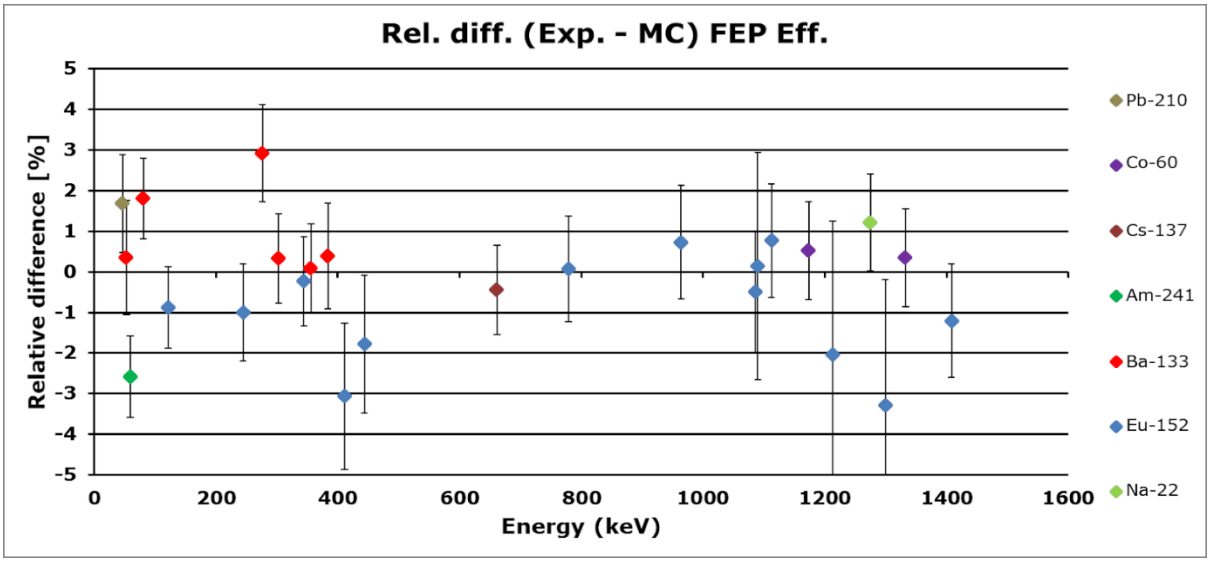

Figure 59: Relative difference in efficiency between experimental data and simulations for point sources at 10 cm distance (Final model). Average of -0.29% and a spread of 1.49%

6.4 Validation of the model (volume sources)

6.4.1 Point sources (different source-detector distances)

In order to validate the computer model, the last model that ended in acceptable results for the highest source distances, is now used for other distances. Figure 61 shows the model on the endcap, figure 60 shows the model with the source at 4 cm distance.

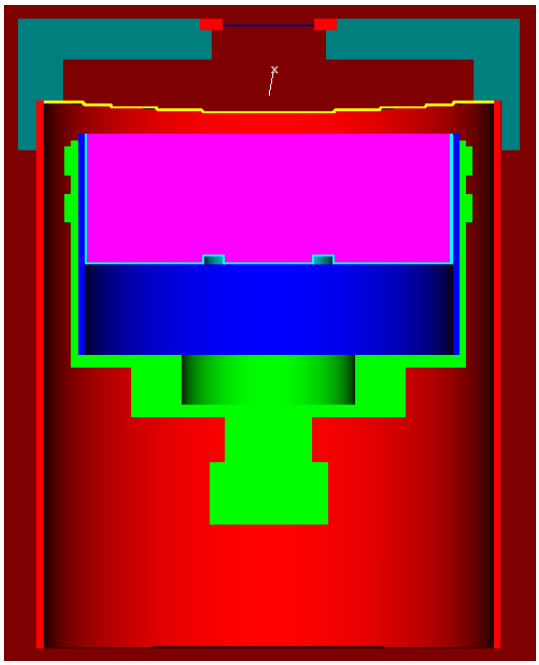

Figure 61: Model of Ge-T10 detector with point source on endcap

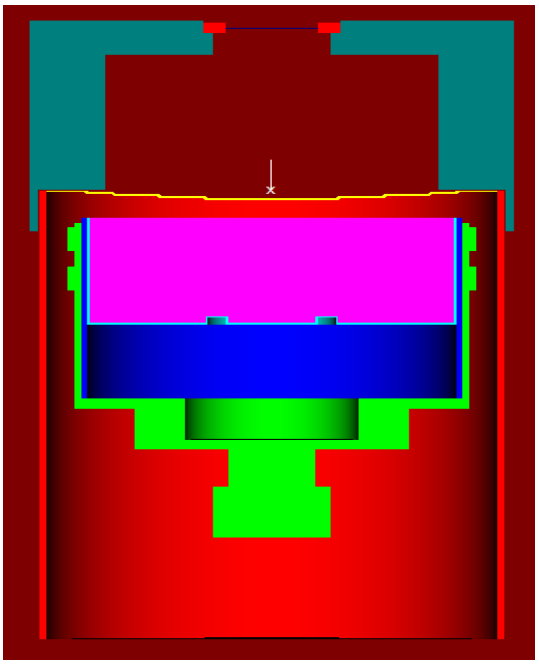

Figure 60: Model of Ge-T10 detector with point source at 4 cm distance

Again, acceptable results were obtained. However, the greater impact of uncertainties in the discussed factors such as source alignment and coincidence summing correction are clearly visible. The spread in relative difference increased, going down in source distance. Besides a general increase in spread, it is shown that ^{152}Eu differs more from the mean average compared to other radionuclides. Based on the literature study in Chapter 3.5 it is expected to be due to the fact that coincidence summing is more prominent for this radionuclide with a very complex decay scheme and including summing with X-rays. Thus, it is suspected that the decay scheme of ^{152}Eu or the summing code used in the model may have imperfections. It is most likely that the complex decay scheme of ^{152}Eu needs a careful scrutiny and update, involving new accurate measurements. As explained is the impact of this factor more dominant at lower source distant and therefore more visible in figure 63 than in figure 62 (on endcap or 4 cm).

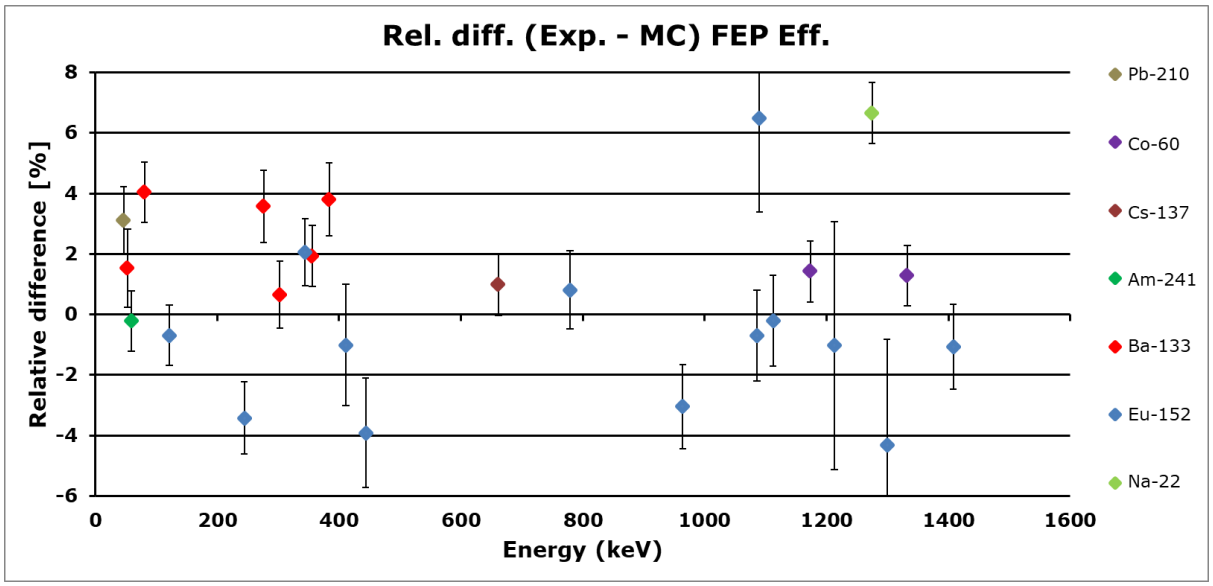

Figure 62: Relative difference in efficiency between experimental data and simulations for point sources at 4 cm distance (Final model) with an average difference of 0.50% and spread of 2.64%

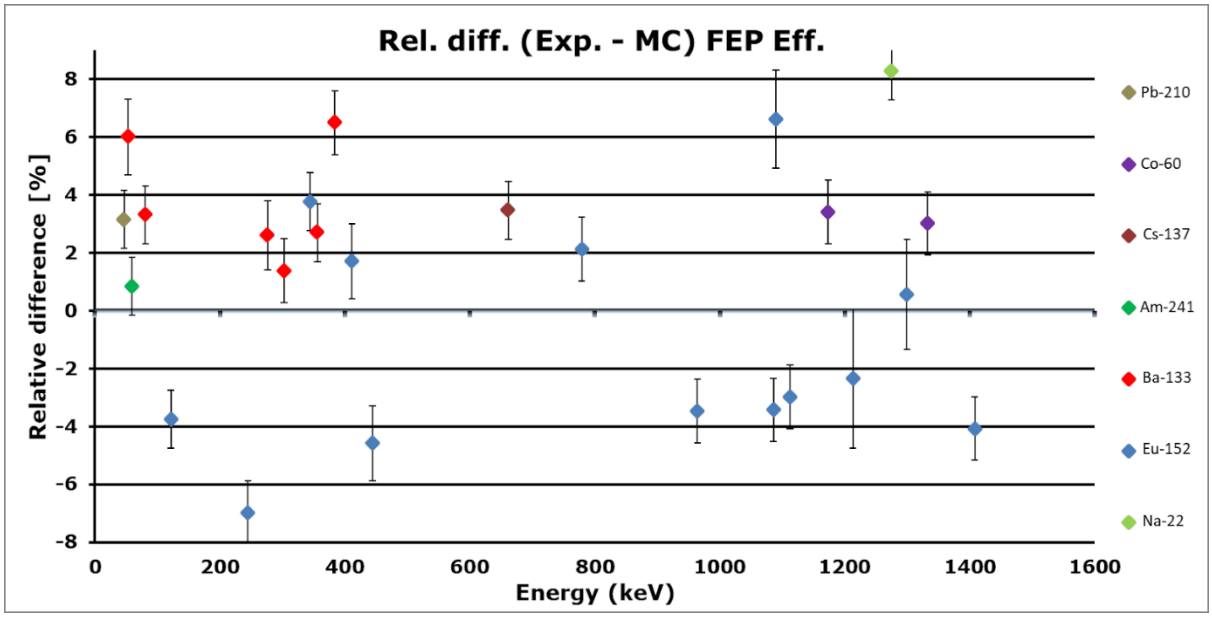

Figure 63: Relative difference in efficiency between experimental data and simulations for point sources on endcap (Final model) with an average difference of 0.92% and spread of 3.79%

6.4.2 Volume sources

As explained, the final model described in the previous Chapter 6.4.1 will be used to simulate efficiency values for specific sample measurements. It should be able to deliver correct efficiency values for any dimensions or geometries of the sample that needs to be measured. Therefore, besides being validated for different source-detector distances for point sources, the computer model should also be validated for volumetric sources. More specific, this is done for four different volume sources containing different radionuclides with different known activities (reference sources). Figure 64-67 shows the implementation of the sources in the temporary (for point sources on different distances) final computer model. If unacceptable deviations occur in the comparison of experimental and simulated efficiency for the volume sources, the model will be adapted accordingly, restarting the optimisation process (iterative process).

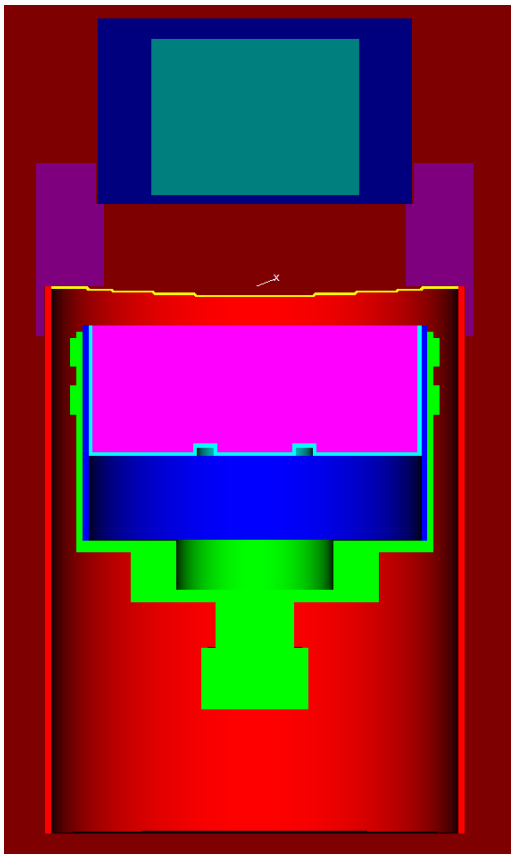

Figure 65: Temporary final computer model of the Ge-T10 for the CMI-3 volume source

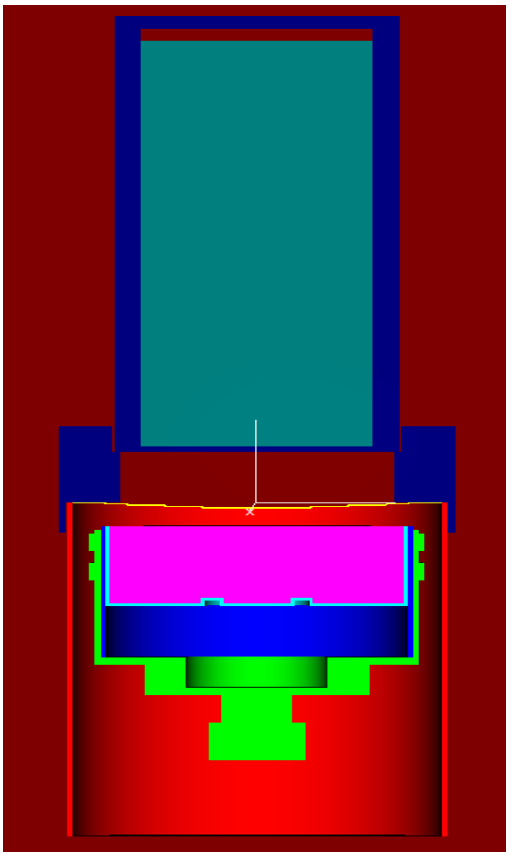

Figure 64: Temporary final computer model of the Ge-T10 for the CMI-14 volume source

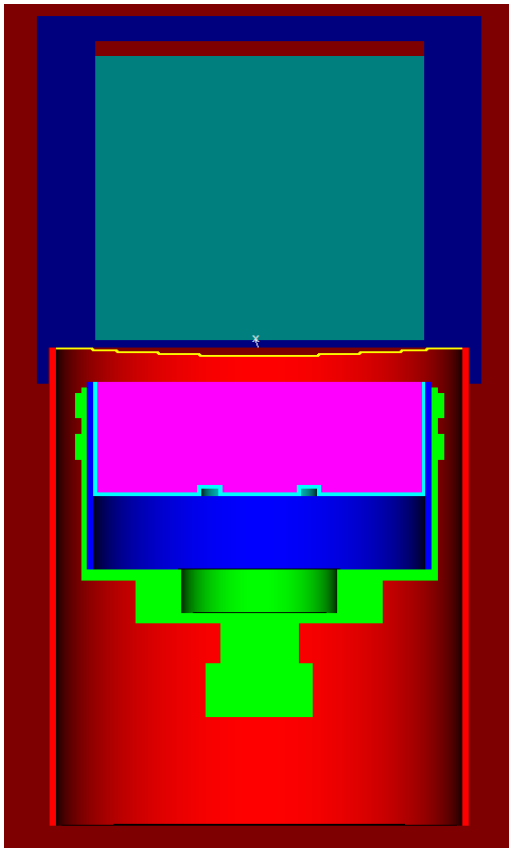

Figure 67: Temporary final computer model of the Ge-T10 for the CMI-15 volume source

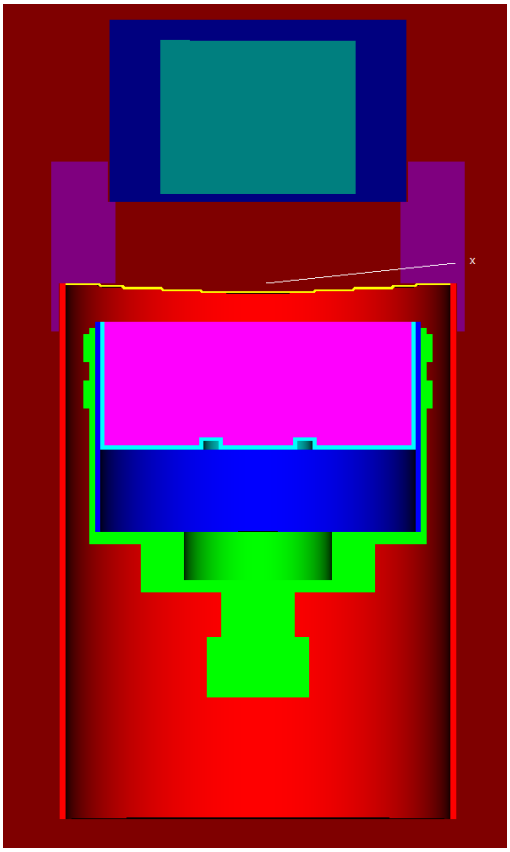

Figure 66: Temporary final computer model of the Ge-T10 for the CMI-8 volume source

Figure 68-71 represents the relative efficiency difference between experimental and simulation data for the different volume sources. It can be seen that the relative difference in general is around 5%.

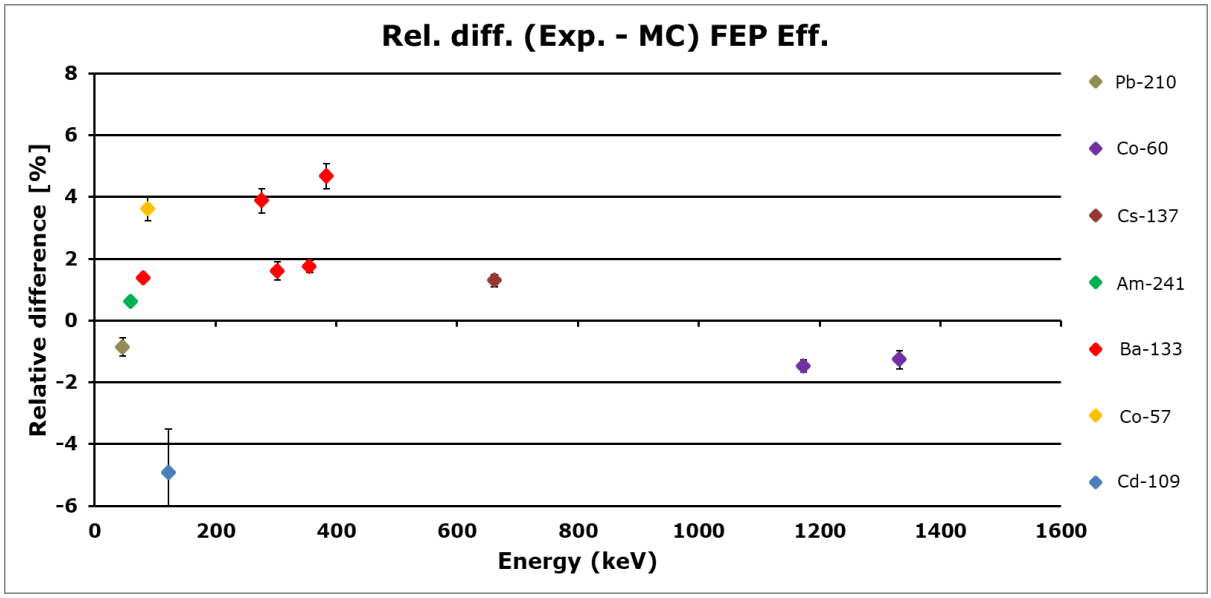

Figure 68: Relative efficiency difference between experimental and simulation data for the CMI-3 Volume source measured at 3.2 cm (midpoint: 4.1045 cm). Average difference 1.40%, spread 2.32%

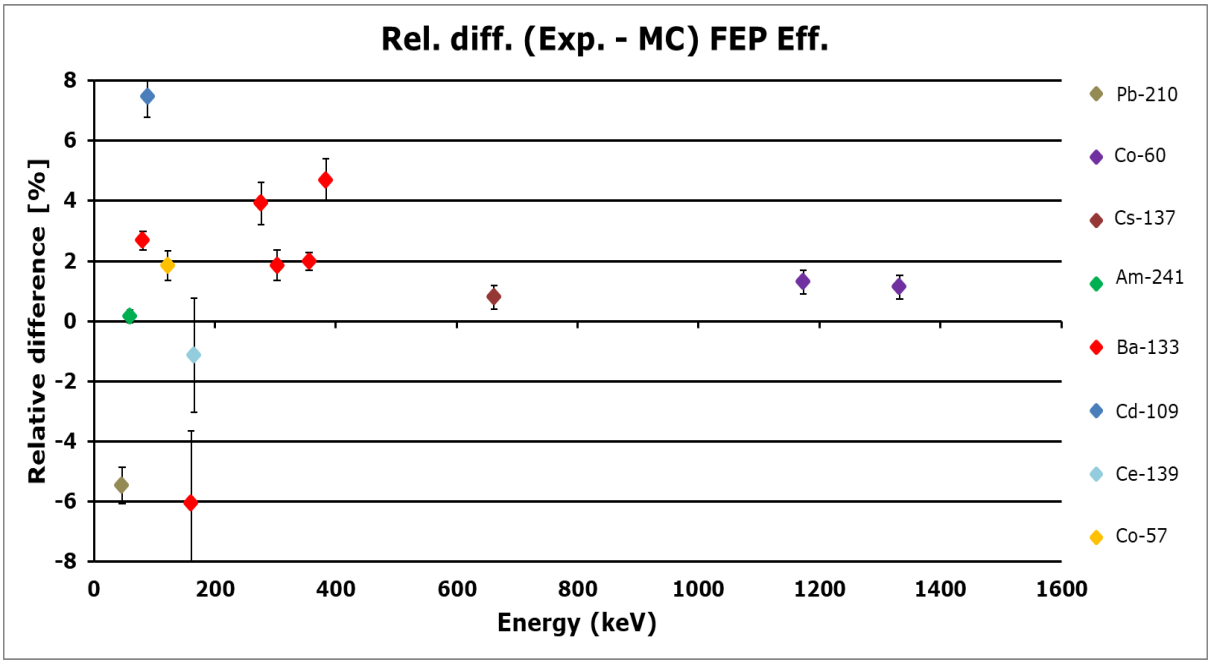

Figure 69: Relative efficiency difference between experimental and simulation data for the CMI-14 volume source measured at 2 cm (midpoint: 10.256). Average difference 1.09%, spread 3.63%

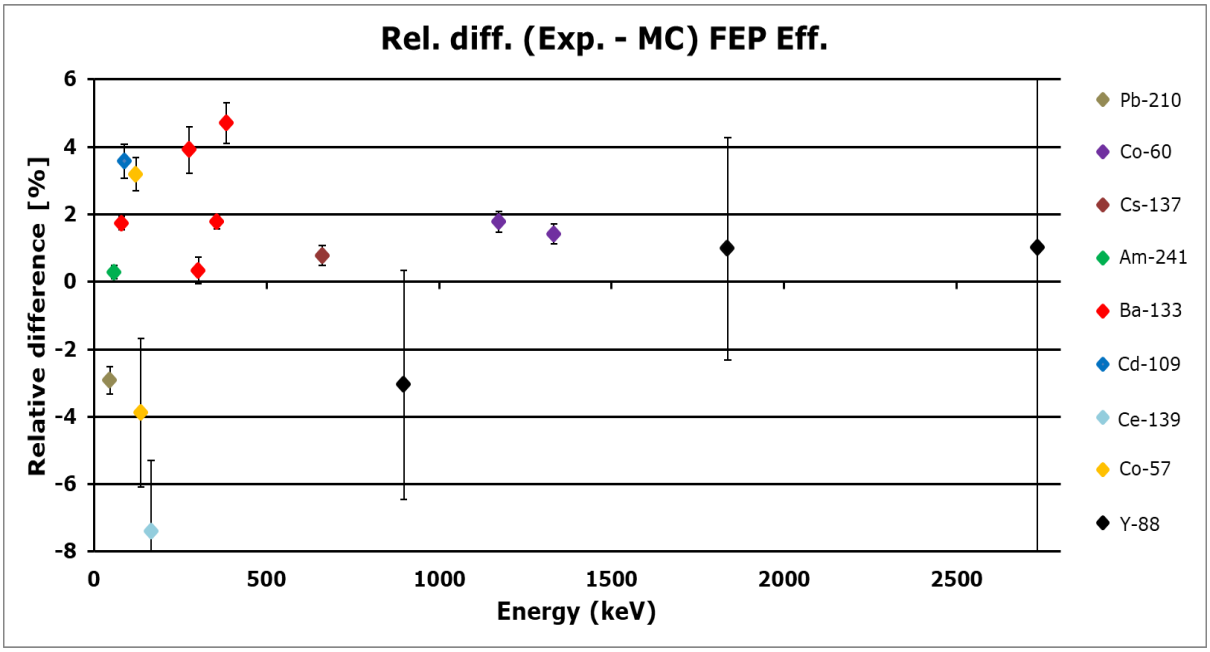

Figure 70: Relative efficiency difference between experimental and simulation data for the CMI-15 volume source measured at 0 cm. Average difference 0.42%, spread 3.15%

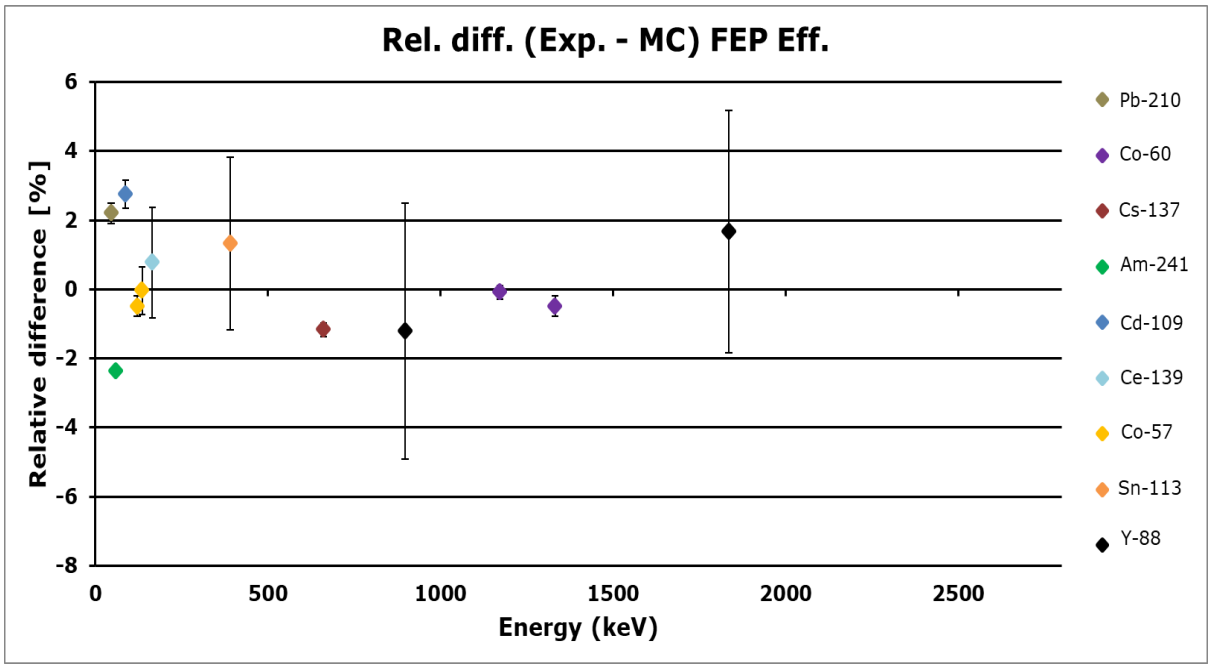

Figure 71: Relative efficiency difference between experimental and simulation data for the CMI-8 volume source measured at 2 cm. Average difference 0.11%, spread 1.64%

A noteworthy fact is that the average deviation for the volume sources is significantly smaller than for point sources close to the detector. This is linked to the fact that the average distance in a volume source is further from the detector than the bottom surface of the volume source. It is thus a fact that gives more confidence in the computer models when measuring “real” samples that are mostly volumes of some 100 cm^3 or so.

7 Optimisation/validation of detector Ge14

This chapter displays the applied working method, difficulties and results of the optimisation and validation of the Ge14 detector. All results essential for drawing a conclusion are included in this chapter. Interim results are present in Appendix B: Relative efficiency difference graphs of Ge-14.

7.1 Original model

The original computer model based on manufacturer's data of Ge14 is displayed in figure 72 including the CMI5 volume source that is used to carry out the optimisation of this detector. A typical representation of a sample suitable to be measured in this detector is visualised in figure 73.

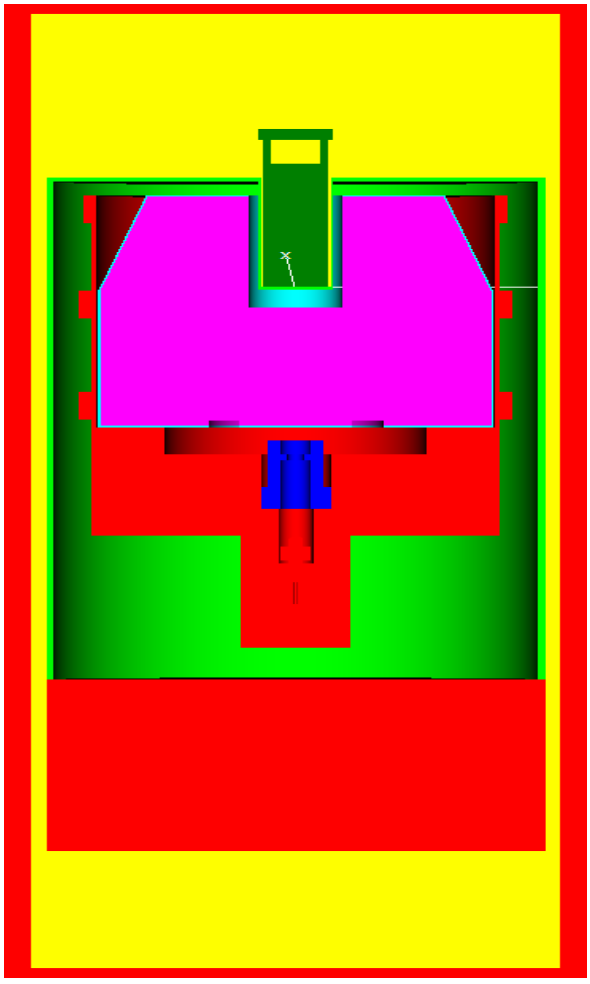

Figure 72: Original model of the Ge14 HPGe well-detector with a volume source inside

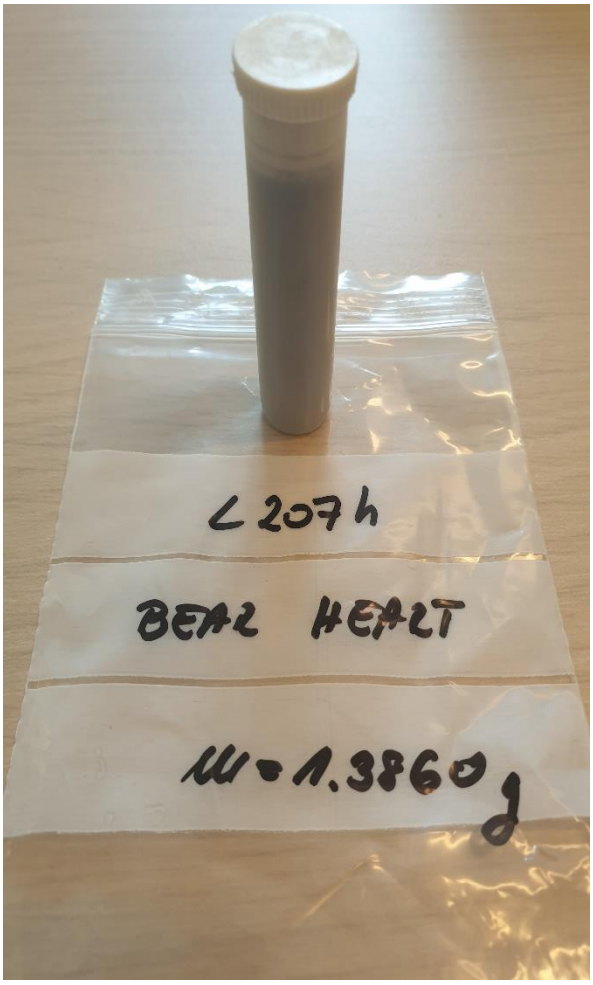

Figure 73: Example of a typical volume source (freeze dried heart from a bear) ready to be measured with the Ge14

This ‘original’ model was the simulated for the same radionuclides and FEPs as measured. After comparison in GLysis with measurement results on the endcap (source standing at the bottom of the well) this resulted in a relative efficiency difference plot as shown in figure 74. A general trend can be seen in this graph, namely that the relative difference efficiency points for all energies are below zero, going down to approximately -20% for lower energies. This indicates that the simulated MC efficiencies overestimate the actual efficiency values and that it is expected that the biggest intervention in the model is needed to change the lower energy efficiency.

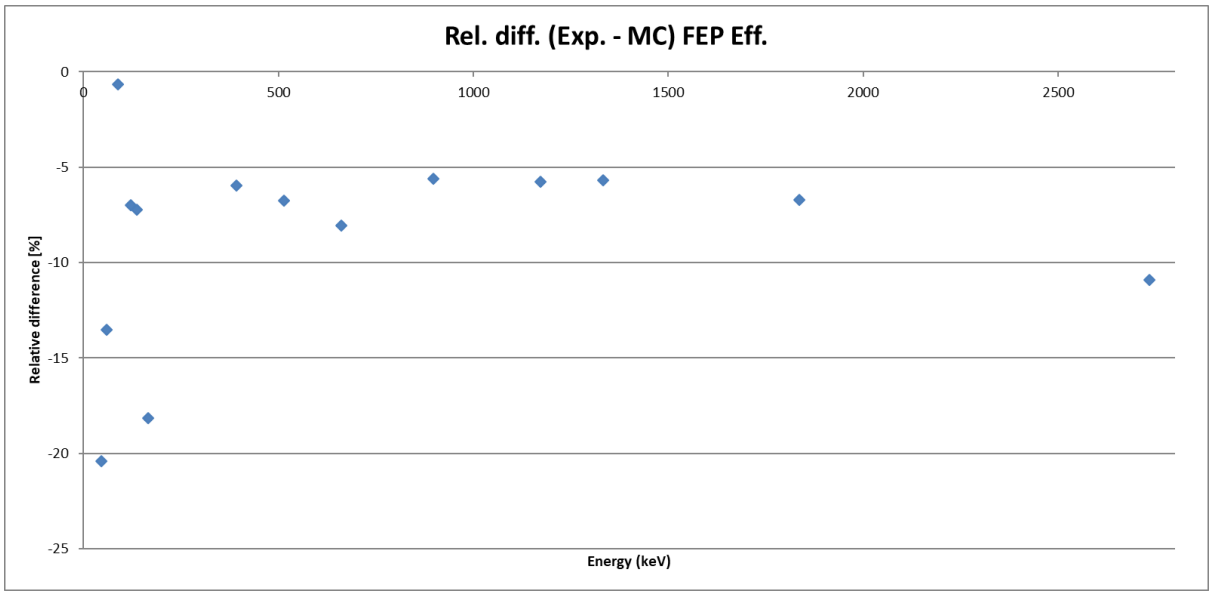

Figure 74: Relative difference in efficiency between experimental data and simulations for CMI5 volume source for the original model of the Ge14 detector with an average of -4.82% and a spread of 5.24%

7.2 Working on optimising the model

In order to lower the simulated efficiency, one of the following parameters is adapted in the model: Crystal position, thickness of the outer deadlayer and thickness of the well-deadlayer. The most suitable parameters to inflict a general (for all energies/FEPs) upwards or downward motion are the crystal position and the thickness of the outer deadlayer. In order to inflict a change in relative efficiency difference for the lower energies, the thickness of the well-deadlayer is in focus. Simulations were performed in which the crystal position in the model was lowered up until minus 0.5 mm. Simultaneously, the outer deadlayer was adjusted, ranging from 0.05 cm to 0.17 cm and the well-deadlayer was varied between 0.004 cm and 0.015 cm. In figure 75 it can be seen that while changing only the outer and well-deadlayers, a relative large spread on the calibration points remains for all energies (especially lower energies). By moving down the crystal and changing the thickness of the well-deadlayer, a lower spread on the lower energy calibration points is achieved, but the spread on higher energies is worse as shown in figure 76. An increase in outer deadlayer is required to uplift the calibration points for higher energies.

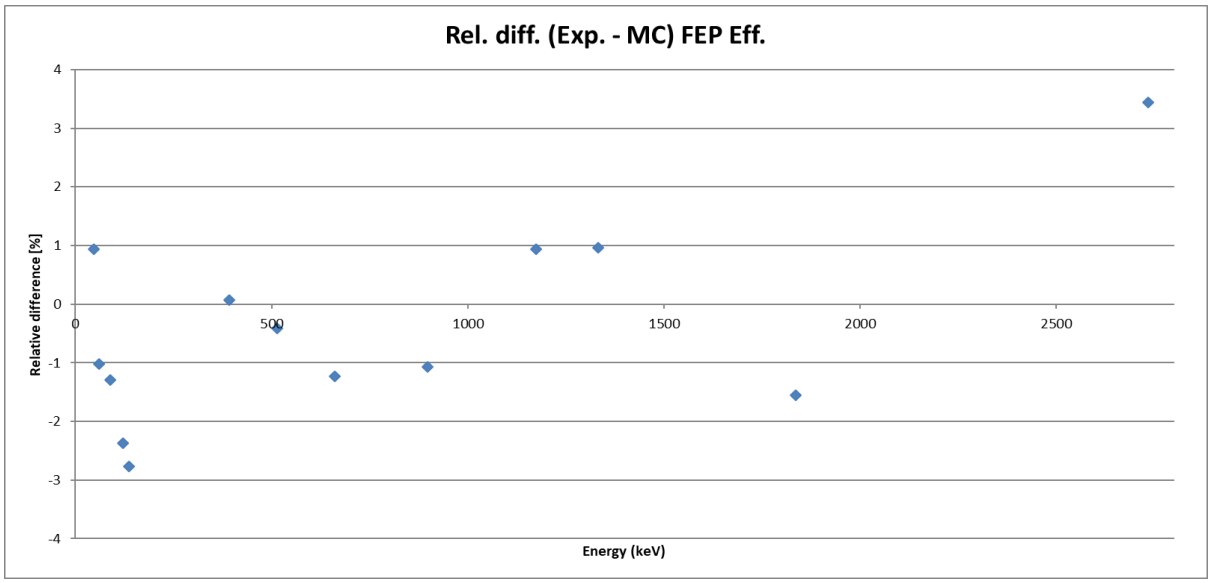

Figure 75: Relative difference in efficiency between experimental data and simulations for CMI5 volume source with an increase of outer deadlayer by 0.12 mm and increase of well-deadlayer by 0.08 mm compared to the original model with an average of -0.71% and a spread of 1.31%

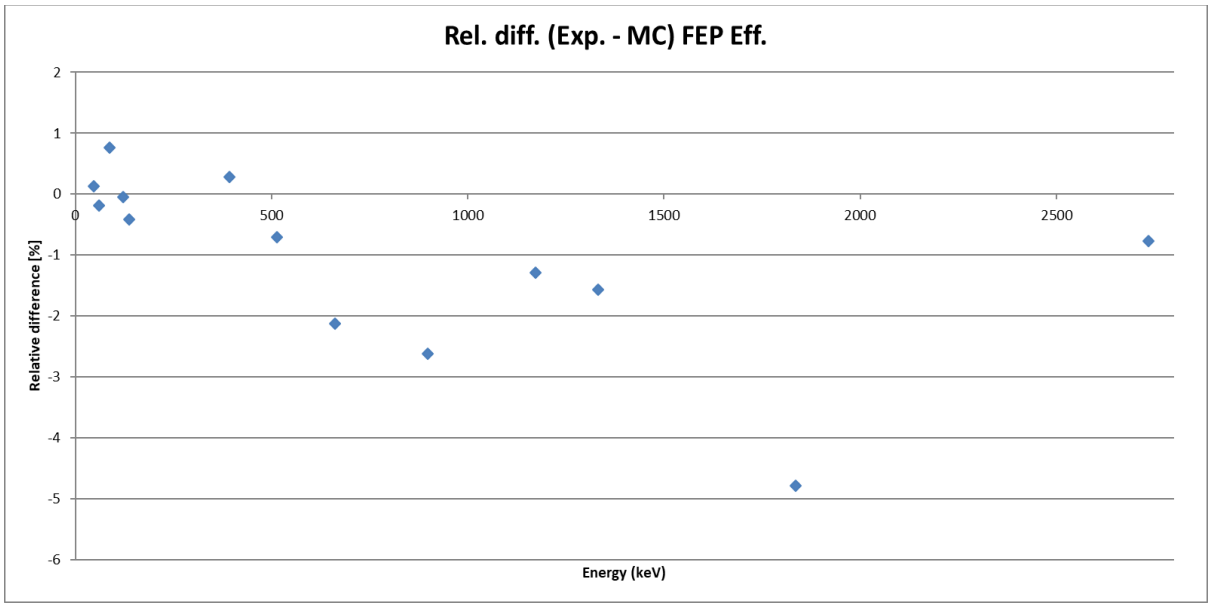

Figure 76: Relative difference in efficiency between experimental data and simulations for CMI5 volume source with an increase of outer deadlayer by 0.01 cm (to 0.06 cm), increase of well-deadlayer by 0.006 cm (to 0.01 cm) and moving down the crystal position by 0.25 cm compared to the original model (average of 0.59% and spread of 1.34%)

However, by increasing the thickness of the side deadlayer in the latest model, an unexpected result was achieved shown in figure 77. It can be seen that the adaptations caused a shift for lower energy efficiencies even though it was expected to mainly target the efficiency at higher energies. Taking a closer look at figure 78, this can be explained by the fact that the volume source used for the optimisation is filled to an extent above the well. Therefore, some of the radation crosses this thicker (compared to the well-deadlayer) outer deadlayer before reaching the sensitive volume of the germanium crystal. At this distance (close to the source), a thicker deadlayer lowers the efficiency at lower energies tremendously. Taking this into account the outer deadlayer is split up from now on, introducing ‘top deadlayer’ as the top part of the outer

deadlayer. From now on, this top deadlayer is held at original thickness of 0.05 cm. This may seem a bit unconventional at first, but referring to paragraph 3.3.1 HPGe detector b) deadlayer, it was explained and referred to how besides changes in thickness overtime, these deadlayer changes can be non-uniformly. Besides that, in many cases the samples used in this well-detector are going to be filled in such a way that it extends above the well. Therefore, it is desired to be optimised for this geometry justifying this change in the model.

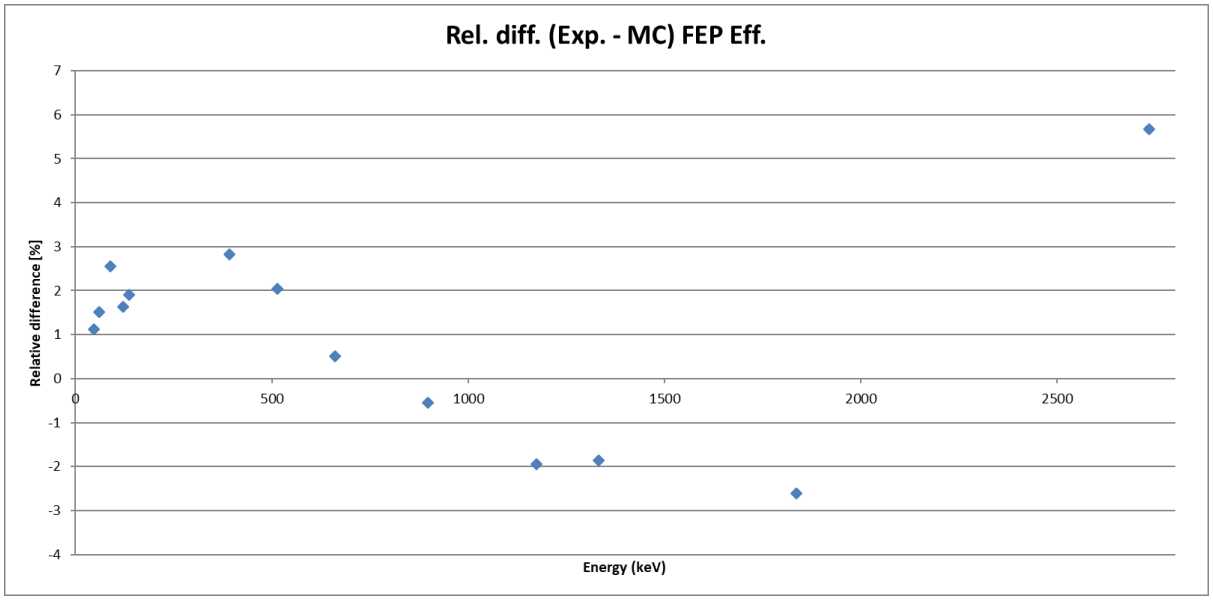

Figure 77: Relative difference in efficiency between experimental data and simulations for CMI5 volume source with an increase of outer deadlayer by 0.05 cm (to 0.1 cm), increase of well-deadlayer by 0.006 cm (to 0.010 cm) and moving down the crystal position by 0.25 cm compared to the original model (average of -0.83% and spread of 1.63%)

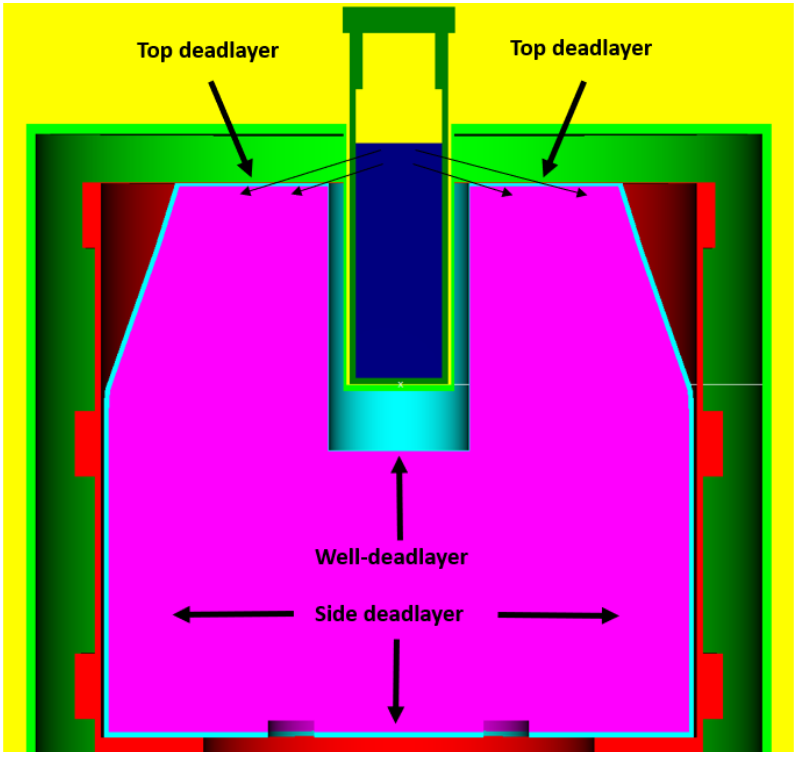

Figure 78: Overview of different 'types' of deadlayers and the path of gamma radiation through the top deadlayer

7.3 Final version of the model

Following the previous paragraph, a final version of the computer model was reached. It was decided to only change deadlayer thickness and not move the crystal since lower spread on relative efficiency difference across all energies was achieved this way. This was done by increasing the thickness of the outer deadlayer by 0.12 cm (to 0.17 cm) and increasing the thickness of the well-deadlayer by 0.010 cm (to 0.014 cm).

This resulted in an optimal relative difference graph shown in figure 79. It can be seen that the Mean dev. Is -0.71% with a maximum relative difference (spread around zero) of 1.312831%. Besides the numerical results, it is important to perform a statistical analysis to determine whether the results can be further improved, or whether certain radionuclides appear as outliers. Therefore, different uncertainties were emerged to get to the uncertainty of the difference between experimental and simulation. Following uncertainties were included: calibration source activity, gamma-ray emission probability, experimental counts, measurement time, simulation uncertainty and last but not least coincidence summing correction. All these factors combined are visualised in figure 79 as one sigma. 23% of all points cross zero at one sigma, 23% of all points cross zero at two sigma. This is not in agreement with statistical theory (68% for 1 sigma, 95% for 2 sigma). However this does not mean that this model cannot be accepted for further use as explained before. Comparing with the model of the Ge-T10, this efficiency calibration process is more difficult since there is mixing of parameters as explained in paragraph 7.2. Working on the model. There it was seen that increasing the side deadlayer also impacts the lower energies because of the filling geometry of the calibration source therefore complicating the calibration process. The last point at 2734 keV stands out to the eye but is only 3.4% away from the zero-line and therefore very close to the criterion of reaching 3%. This point can be said to be a bit tricky as it has contributions both from the sum of 898 keV + 1836 keV and a direct transition from the 2734 level.

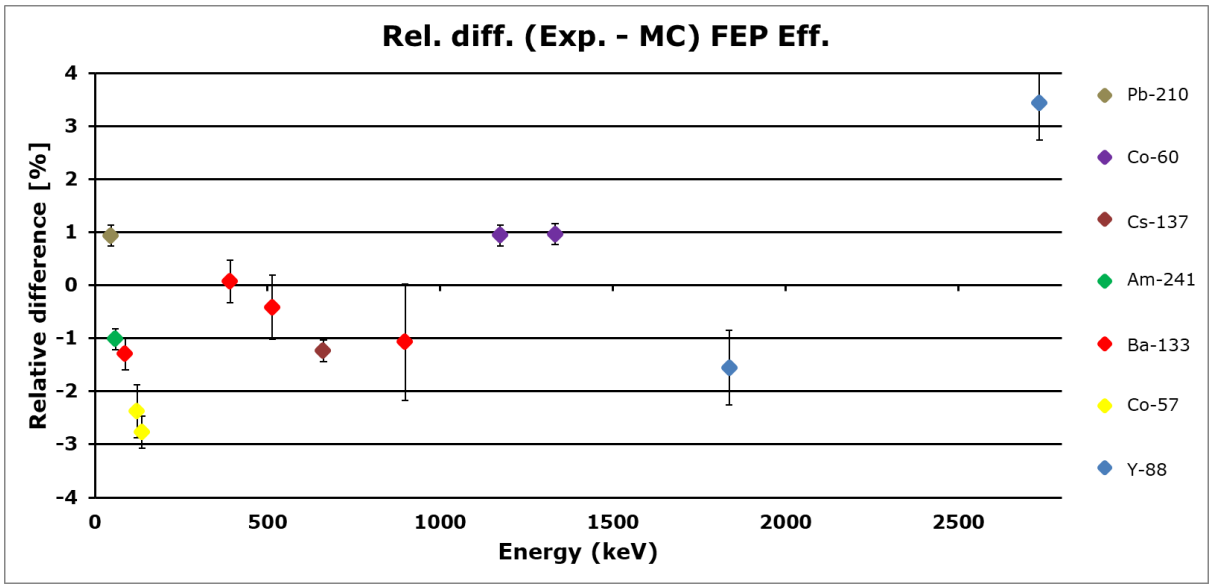

Figure 79: Relative difference in efficiency between experimental data and simulations for CMI5 volume source for the final model (average of -0.17% and spread of 1.31%)

7.4 Validation of the model

The final model will be used to simulate efficiency values for specific sample measurements, an example of such a project is implemented in paragraph 8. It should be able to deliver correct efficiency values for any dimensions or geometries of the sample that needs to be measured. Therefore, the current final computer model (Thickness of the outer deadlayer 0.17 cm and the well-deadlayer 0.014 cm) is also validated for another volumetric source. The volume source used for the validation of the model is the CMI4 and has the same dimensions, geometries and filling height as the CMI5 volume source as shown in figure 76. Ideally, a source with different filling height or other geometry should be used. For example a volume source completely filled like the samples used in the ROWAN project in paragraph 8. This would ensure more certainty about the final results for that application project. This is not possible since no such calibration sources were available. If unacceptable deviations occur in the comparison of experimental and simulated efficiency for the CMI4 volume source, the model will be adapted accordingly, restarting the optimisation process (iterative process).

Figure 80 shows the relative efficiency difference graph for using the CMI4 volume source. It can be seen that its values are similar to the results of the CMI5 volume source. However, all points are lightly shifted down, stimulating to reoptimize the model slightly.

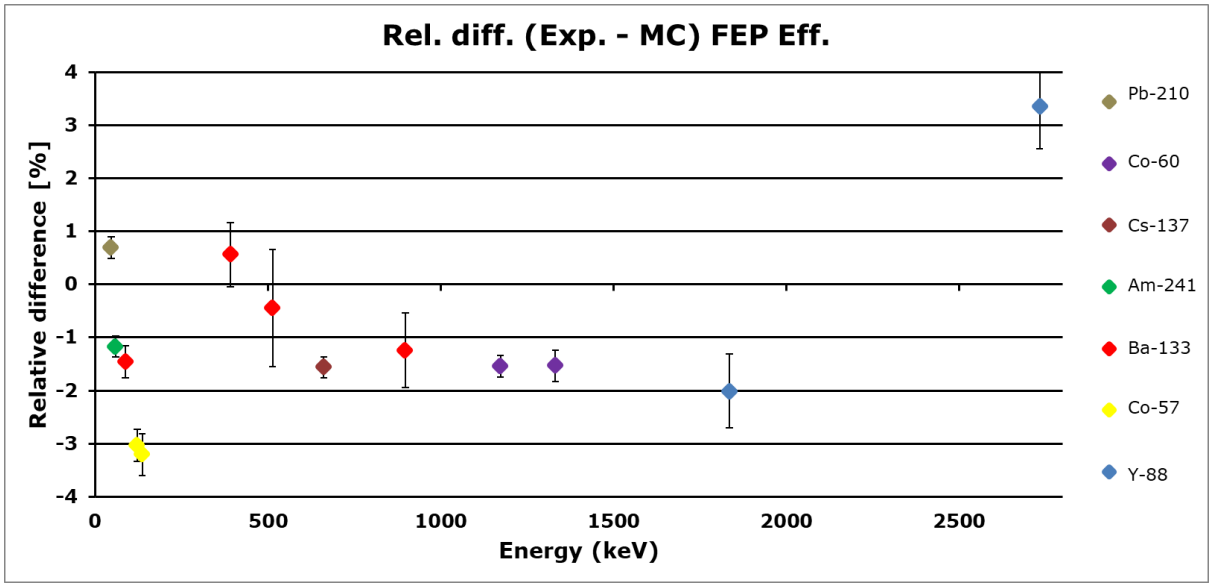

Figure 80: Relative difference in efficiency between experimental data and simulations for CMI4 volume source for the validation of the final model (average of -1.32% and spread of 1.23%)

Since most efficiency calibration points are below zero, it was decided to uplift all points by moving down the crystal under the endcap by 0.05 cm. This resulted in the relative difference graph shown in figure 81. It can be seen that conducted adaptation of the previous model was successful in moving the calibrations points upward. After it was checked if these dimensions also translate in a good working model for the CMI5 volume source. The results of the comparison between experimental data and computer model for the CMI5 is shown in figure 82. Most calibration points are between –2% and 2% after this adaptation.

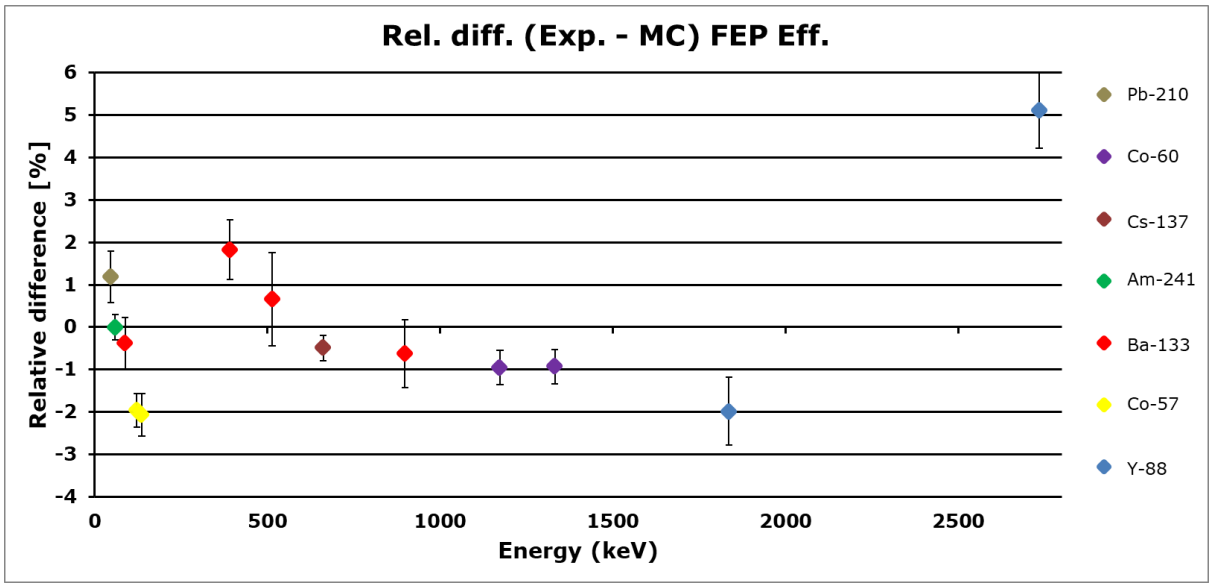

Figure 81: Relative difference in efficiency between experimental data and simulations for CMI4 volume source for the second validation of the final model (average of -0.42% and spread of 1.32%)

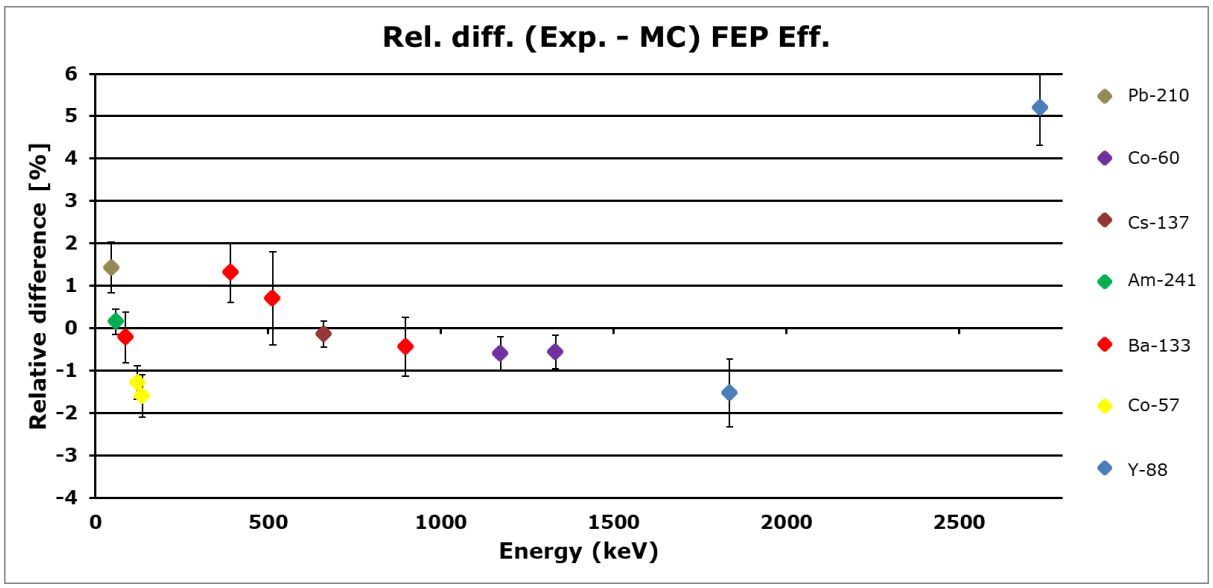

Figure 82: Relative difference in efficiency between experimental data and simulations for CMI5 volume source after the validation of the final model (average of -0.22% and spread of 1.05%)

8 Application of the Ge14 validated model in the project ROWAN

8.1 ROWAN

The new recommendations from ICRP (document 103) call for the first time for protection of the environment for the sake of the environment as such and identifies the need for scientific studies in this field. Consequently, the new Basic Safety Standards (Council Directive 2013/59 EURATOM) have strengthened its demand for radioprotection of the environment. There are basically no studies of distribution of anthropogenic radionuclides in organs of large mammals. Together with several Croatian research groups organs from bear and wolves are now measured within the JRC open access project ROWAN (Radionuclides in Organs of Wild Animals). The small amount of radioactivity present in the sample materials (freeze dried inner organs) calls for using the underground detector Ge14 in HADES. The new computer model was used for calculating the ^{137}Cs activities in these samples. More specific, the computer model was used to determine the efficiency of this measurement which is required to determine the actual ^{137}Cs activities in the samples.

8.2 List of measurements

For this project, samples of different organs form wolves and bears are measured. In order to achieve sufficient statistical data to draw any conclusion about the radioactivity levels present in the animals' organs, multiple animals are being measured. Since it is expected that the sample contain low amounts of radioactivity, each sample is not only measured in HADES to eliminate background in the spectrum but also a long time to obtain enough counts. Therefore, this project is planned over several months meaning that only three samples (kidney, spleen and hearth) of one animal can be analysed by now. Tables 8 and 9 show more information about these three specific measurements.

Table 8: Measured samples information bear

#	Sample-id	Det.	Start-date (dd/mm/year)	Stop-date (dd/mm/year)	Days	Live-time (d)	mass (g)
1	L207 Sp bear spleen	14	01/02/2022	08/02/2022	7	6.93	4.19
2	L207 R bear heart	14	08/02/2022	15/02/2022	7	6.92	1.386
3	L207 k bear kidney	14	15/02/2022	22/02/2022	7	6.94	4.9449

Table 9: Measured samples information wolves

#	Sample-id	Det.	Start-date (dd/mm/year)	Stop-date (dd/mm/year)	Days	Live-time (d)	mass (g)
4	WCRO 291 LUNGS	14	09/03/2023	14/03/2023	5	4.90	4.0194
5	WCRO 291 KIDNEY	14	14/03/2023	22/03/2023	8	7.95	2.6996
6	WCRO 291 MUSCLE	14	22/03/2023	29/03/2023	7	6.89	3.2844
7	WCRO 291 HEART	14	29/03/2023	04/04/2023	6	5.94	3.6879
8	WCRO 291 SPLEEN	14	04/04/2023	12/04/2023	8	7.93	4.5354
9	WCRO 271 muscle	14	20/04/2023	25/04/2023	5	4.90	3.6574
10	WCRO 271 kidney	14	25/04/2023	05/05/2023	10	9.88	3.1338
11	WCRC 271 spleen	14	05/05/2023	10/05/2023	5	4.96	3.8994
12	WCRO 271 heart	14	10/05/2023	16/05/2023	6	5.94	3.72
13	WCRO 271 lungs	14	16/05/2023	23/05/2023	7	6.83	3.5767
14	WCRO 271 liver	14	23/05/2023	30/05/2023	7	6.94	3.8121

8.3 Sample preparation

This chapter discusses the sample preparation of the organs used in this measurement project (this was executed by the Czech researchers of the Ruđer Bošković Institute) . A distinction is made between sample preparation for soft tissues and bone tissues (these samples are not included in Chapter 8.4 Result since they are not measured yet). The following bullet list represents which actions of the sample preparation are carried out on which location:

- The sample collection and storage is done in the Faculty of Veterinary Medicine, University of Zagreb which has suitable equipment for these tasks.
- Freeze-drying, soft tissue homogenization and the use of a diamond blade for certain interventions is done in the Institute for Medical Research and Occupational Health.
- Oven-drying, bone preparation and cryogenic grinding is performed in the Ruđer Bošković Institute.
- Sample packing is done in the Ruđer Bošković Institute.

The sample preparation of soft tissue starts by sectioning the concerning tissues of the wolf carcasses, after which the tissue samples are stored at -18°C. Approximately, 30 to 60 g of tissue (depending on tissue type) was freeze-dried. Afterwards, the samples were pulverized and homogenized by a kitchen grinder. A few grams from those samples were taken for ICP-MS analysis. Finally, approximately 2 to 4 g (average of 3 g) of pulverised and homogenised sample was packed in a vial (similar to CMI5) for gamma-ray spectrometry.

The sample preparation of bone tissue starts with removing one femur from each carcass (during sectioning of wolf carcasses) for analysis. Femurs were then stored at -18°C until analysis. Whole femur were dried at 105°C for 72 h. After drying, residual soft tissue (e.g. tendons and muscle) were scrapped of the bones and small fragments (5x5 mm) were cut form the femur diaphysis with a diamond blade. Remains of the bone were cut with a diamond blade in several larger fragments after which is was freeze-dried to remove any remaining water. Freeze-dried bone fragments were submerged into liquid nitrogen to make them more brittle before breaking in smaller fragments that are suitable for cryogenic grinding. Finally, bones were pulverized and homogenized by cryogenic grinding. All available bone powder was packed in larger containers for gamma-ray spectrometry (approximately 50 g)

8.3 Data analysis

Before data analysis can be performed, the model needs to be adapted according to the experimental situation. Since the sources have the same dimensions as the CMI5 volume source for which the model was optimised, no geometric adaptations to the source are required. However, the content of the source is no longer gel, yet it is now the different organs of wolves and bears. Therefore, the material list of the code is updated for the right organic composition for soft tissue organ. This is done based on lab analysis executed by the Croatian research group at the Ruđer Bošković institute in Zagreb, Croatia. Table 10 gives the composition of each organ of the large wild mammals and table 11 gives an overview of the composition used for all organs (soft tissue (approximation)). Besides that, all samples have a different density which will impact the efficiency determination. Thus, this is the only factor the code differs in for different organs.

Table 10: Overview of elemental composition for different organs of large wild mammals

FINAL Mass fractions (%) of elements in freeze dried tissue (no water) NORMALIZED to 100%															
ORGAN	H	C	N	O	Na	Mg	P	S	Ca	Fe (representing all heavier elements)	sum	Sr	Ba	Pb	Sum-bones
MUSCLE	7.896	49.340	14.973	23.804	1.392	0.381	0.936	0.936	0.167	0.176	100				
LIVER	8.393	48.004	15.060	24.394	1.525	0.198	0.941	0.941	0.106	0.436	100				
HEART	8.548	46.874	14.706	24.173	2.889	0.541	0.919	0.919	0.108	0.324	100				
KIDNEY	8.548	46.874	14.706	24.173	2.889	0.541	0.919	0.919	0.108	0.324	100				
SPLEEN	7.819	47.259	14.826	23.572	3.370	0.411	0.927	0.927	0.152	0.737	100				
LUNGS	9.625	45.313	14.216	24.730	3.397	0.166	0.888	0.888	0.173	0.604	100				
BONES	3.383	24.647	7.732	11.598	1.046	0.586	0.483	0.483	49.996	0.025		0.013	0.007	0.000	100.000

Table 11: Organic composition of soft tissue (these values are used for each organ)

FINAL Mass fractions (%) of elements in freeze dried tissue (no water) NORMALIZED to 100%											
ORGAN	H	C	N	O	Na	Mg	P	S	Ca	Fe (representing all heavier elements)	sum
AVERAGE soft tissue	8.471	47.277	14.748	24.141	2.577	0.373	0.922	0.922	0.136	0.433	100
Rel.st.dev (%)	7.0	2.6	1.8	1.6	31.7	39.7	1.8	1.8	21.4	43.3	

For the calculation of the elemental composition a few approximations were made:

- Assumption of the lack of presence of water since everything was freeze-dried.
- Carbs were assumed to be 100% carbon
- Assumed equal amounts of phosphor and sulphur.

Note that it is not critical for our calculations to have the exact values of the composition of each organ as the nuclear interactions are only sensitive of large amounts of elements heavier than ^{55}Fe.

8.4 Results

Table 12: Results of activities for ^{137}Cs, ^{210}Pb, ^{22}Na and ^{40}K in wolf and bear organs

#	Sample-id	Bear/Wolf	Organ	137Cs: massic activity (mBq/g)	^{210}Pb: massic activity (mBq/g)	^{22}Na: massic activity (mBq/g)	^{40}K: massic activity (mBq/g)
1	L207 Sp bear spleen	Bear	Spleen	1.9	3.5	1.1	312
2	L207 R bear heart	Bear	Heart	25	<2.4	8.1	1249
3	L207 k bear kidney	Bear	Kidney	2.4	46.1	2.3	213
4	WCRO 291 LUNGS	Wolf	Lung	5.1	<0.65	<0.84	118
5	WCRO 291 KIDNEY	Wolf	Kidney	14	1.7	3.2	247
6	WCRO 291 MUSCLE	Wolf	Muscle	12	<0.95	<1.3	358
7	WCRO 291 HEART	Wolf	Heart	13	<0.93	<1.2	304
8	WCRO 291 SPLEEN	Wolf	Spleen	13	<0.77	<1.0	389
9	WCRO 271 muscle	Wolf	Muscle	187	<1.7	<2.2	419
10	WCRO 271 kidney	Wolf	Kidney	120	3.3	<1.6	321
11	WCRC 271 spleen	Wolf	Spleen	112	<1.4	2.2	334
12	WCRO 271 heart	Wolf	Heart	102	<1.2	<1.9	325
13	WCRO 271 lungs	Wolf	Lung	87	1.8	2.8	251
14	WCRO 271 liver	Wolf	Liver	99	<1.2	<1.6	278

Table 13: Uncertainties for organ activities

#	Sample-id	Bear/Wolf	Organ	137Cs: Uncertainty (k=1) (mBq/	210Pb: Uncertainty (k=1) (mBq/	22Na: Uncertainty (k=1) (mBq/	40K: Uncertainty (k=1) (mBq/
1	L207 Sp bear spleen	Bear	Spleen	0.1	1.9	0.5	11
2	L207 R bear heart	Bear	Heart	0.9	1.8	1.5	43
3	L207 k bear kidney	Bear	Kidney	0.11	22	0.64	7.3
4	WCRO 291 LUNGS	Wolf	Lung	0.21	0.51	0.55	4.5
5	WCRO 291 KIDNEY	Wolf	Kidney	0.5	0.98	0.79	8.7
6	WCRO 291 MUSCLE	Wolf	Muscle	0.4	0.59	0.77	13
7	WCRO 291 HEART	Wolf	Heart	0.5	0.57	0.75	11
8	WCRO 291 SPLEEN	Wolf	Spleen	0.5	0.5	0.65	13
9	WCRO 271 muscle	Wolf	Muscle	6	1.1	1.5	15
10	WCRO 271 kidney	Wolf	Kidney	3.7	2.2	1.1	11
11	WCRC 271 spleen	Wolf	Spleen	3.5	0.86	1.5	12
12	WCRO 271 heart	Wolf	Heart	3.2	0.78	1.2	12
13	WCRO 271 lungs	Wolf	Lung	2.8	1.2	1.2	8.7
14	WCRO 271 liver	Wolf	Liver	3.1	0.75	1	9.6

Table 14: Decision thresholds for organ activities

#	Sample-id	Bear/Wolf	Organ	137Cs: Decision threshold (mBq/g)	210Pb: Decision threshold (mBq/g)	22Na: Decision threshold (mBq/g)	40K: Decision threshold (mBq/g)
1	L207 Sp bear spleen	Bear	Spleen	0.067	1.3	0.76	0.72
2	L207 R bear heart	Bear	Heart	0.25	2.4	2	2.2
3	L207 k bear kidney	Bear	Kidney	0.056	1.4	1	0.47
4	WCRO 291 LUNGS	Wolf	Lung	0.051	0.65	0.84	0.47
5	WCRO 291 KIDNEY	Wolf	Kidney	0.097	0.85	0.97	0.67
6	WCRO 291 MUSCLE	Wolf	Muscle	0.095	0.95	1.3	0.75
7	WCRO 291 HEART	Wolf	Heart	0.089	0.93	1.2	0.67
8	WCRO 291 SPLEEN	Wolf	Spleen	0.088	0.77	1	0.77
9	WCRO 271 muscle	Wolf	Muscle	0.18	1.7	2.2	1.2
10	WCRO 271 kidney	Wolf	Kidney	0.14	2.4	1.6	0.75
11	WCRC 271 spleen	Wolf	Spleen	0.16	1.4	2.1	0.83
12	WCRO 271 heart	Wolf	Heart	0.15	1.2	1.9	0.66
13	WCRO 271 lungs	Wolf	Lung	0.13	1.2	1.5	0.67
14	WCRO 271 liver	Wolf	Liver	0.13	1.2	1.6	0.47

The results in Tables 12, 13 and 14 were provided to the Croatian research group and they concluded that this data could not have been obtained from their above ground HPGe-detector. The impact is that a larger number of items will be measured to make this the biggest study of its kind so far. The radiobiological results are out of the scope of this thesis which focussed on the metrological aspects. In connection to that follows an uncertainty budget.

9 Summary and conclusion

Both the Ge-T10 and Ge14 detector models are now fit for being applied in various accredited measurement projects. By comparing figure 55 and 56 from the Ge-T10 results, it can be concluded that the optimal starting point for an efficiency calibration is at a higher source detector distance in order to minimise the impact of phenomena such as uncertainties in alignment, homogeneity of calibration sources, uncertainties in coincidence summing corrections (linked to uncertainties in the decay schemes and more complex simulations) and in some cases with high count-rate induced dead-time (not present in this thesis work). These factors are more prominent at lower source detector distances. The deviation of ^{152}Eu (shown in figure 63 and in agreement with earlier predictions (see 5. Objectives and hypotheses)), at lower source detector distance (on endcap) is greater than the other radionuclides. It is due to the fact that coincidence summing is more prominent for this radionuclide because of its complex decay scheme. Thus, it is suspected that the decay scheme of ^{152}Eu or the summing code used in the model may have imperfections. It is also possible that when summing takes place, imperfections in the model multiply and manifest themselves more clearly, but this statement is not substantiated but could be the focus of a future study. As explained, the impact of this factor more dominant at lower source-detector distances and therefore more visible in figure 63 than in figure 62. It is clear that the radionuclide metrology community would look positively on a study carefully going through and re-measuring decay parameters involved in the decay of ^{152}Eu. With the development of more advanced nuclear technologies, it is essential that the basic nuclear data follow and is apt for the demands of the modern world.

During the optimisation process of Ge14 it was seen that due the fact that the volume sources are filled to an extent above the well, the thickness of the outer deadlayer no longer only had impact on the efficiency at higher energies but also on efficiency at lower energies. For calibration purposes, it is desirable to have the different parameters impact separate energy-regions. Therefore, it is suggested to use calibration sources filled to different heights: Some with point sources residing at the bottom of the well. Others with point sources in the middle of the well and perhaps a circular sources to be placed on top of the detector to minimise the influence of the well deadlayer. This will increase the convenience of the calibration of the computer model of the detector.

The validation of the model for the HPGe coaxial GeT10 detector through the use of volume sources and point sources at different source-detector distances showed that the optimised model can be accepted as a good working model of this detector. The original computer model was improved by moving the crystal down by 0.15 cm, increasing the thickness of the side deadlayer by 0.05 cm and decreasing the thickness of the endcap by 0.01 cm. At the highest source-detector distance (10 cm) the relative difference in efficiency was limited to +/- 3%. It can be concluded that this model can be used for determining the efficiency of different application projects for all sorts of geometries.

The validation of the model for the HPGe Ge14 well-detector through the use of the other volume source, CMI4, proved that the model could be further improved. On top of an increase in the side deadlayer of 0.12 cm and an increase of the well-deadlayer of 0.010, the validation process led to a downwards movement of the crystal by 0.005 cm. At the highest source-detector distance (10 cm) the relative difference in efficiency was limited to +/- 2%, which is in agreement with the hypothesis of lower relative differences in efficiency for a well-detector than for a coaxial detector. Thus, the final model consist of a the Ge14 has a crystal position of 0.005 cm, thickness of the side deadlayer of 0.17 cm and thickness of the well-deadlayer is 0.14 cm.

From the ROWAN application project, it can be concluded that the Ge14 detector is perfectly suited for measuring the two radionuclides of main interest: ^{137}Cs and ^{210}Pb. Neither suffers from coincidence summing and therefore the FEP efficiency (per gamma) is very high: 20% at 662 keV and 37% at 46.5 keV. During spring 2023, 15 samples were measured on detector Ge14. In all samples ^{137}Cs were detected and in five samples (bear spleen, bear kidney, wolf kidneys and in one wolf lung) ^{210}Pb was detected. These results are important for building up a better understanding of the metabolism of large wild mammals and thus the distribution of different radionuclides in their organs. ^{40}K and ^{22}Na (cosmogenic) natural occurring radioactive material and are therefore found (in low activities) in the organs of the measured wolves and bears. ^{210}Pb is a long-lived daughter of the ^{238}U decay chain and in nature. The presence of low activity levels of ^{137}Cs in organs of wild large mammals dates back to the nuclear accident in Chernobyl and possibly some remains from atmospheric weapons testing. Besides that, not enough measurements where performed up until now in order to draw a well-grounded conclusion about difference in distribution in different organs. This also beyond the scope of this thesis, but will be further investigated at the JRC. The results of the study were surprisingly positive in the sense that ^{137}Cs was detected in all samples, which was unexpected. This opens up for future, larger scale studies on large wild mammals.

References

[1] M. Hult, V. Jobbagy, and K. Sobiech-Matura, *Radioactivity monitoring: How the JRC verifies results from monitoring within the European Union - A quick guide*. Luxembourg: Publications Office of the European Union, 2019.

[2] M. Hult, G. Lutter, G. Marissens, and H. Stroh, *JRC serving policy and science at the HADES underground research facility - a casebook*. Luxembourg: Publications Office of the European Union, 2020.

[3] L. Brabants, G. Lutter, J. Paepen, B. Vandoren, B. Reniers, and W. Schroeyers, 'Validation of TOPAS MC for modelling the efficiency of an extended-range coaxial p-type HPGe detector', *Applied Radiation and Isotopes*, vol. 173, Jul. 2021, doi: 10.1016/j.apradiso.2021.109699.

[4] D. Jacques, 'Fuel cycle, waste and decommissioning'. SCK CEN.

[5] W. Schroeyers, 'Stralingsbescherming & dosimetrie'. KU Leuven.

[6] M. Hult, W. Preusse, W. Preuße, J. Gasparro, and M. Köhler, 'Underground gamma-ray spectrometry', *Acta Chim. Slov*, vol. 53, pp. 1–7, 2006.

[7] B. Minty and M. Geophysics, 'Fundamentals of airborne gamma-ray spectrometry'.

[8] M. Hult *et al.*, 'Underground gamma-ray measurements of radium isotopes from hydrothermal plumes in the deep Pacific Ocean', *Applied Radiation and Isotopes*, vol. 153, Nov. 2019, doi: 10.1016/j.apradiso.2019.108831.

[9] A. Jenet, B. Acosta-Iborra, L. Aldave de las Heras, and Y. Aregbe, 'Open access to J RC research infrastructures', 2021. doi: 10.2760/562421.

[10] Bart Bruyneel, *Nucleaire meettechnieken*. KU Leuven, 2020.

[11] J. Konya and N. Nagy, 'Radioactive Decay', in *Nuclear and Radiochemistry: Second Edition*, Elsevier Inc., 2018, pp. 49–84. doi: 10.1016/B978-0-12-813643-0.00004-4.

[12] J. Yang *et al.*, ' 60 Co Gamma Ray Damage in Homoepitaxial β-Ga 2 O 3 Schottky Rectifiers ', *ECS Journal of Solid State Science and Technology*, vol. 8, no. 7, pp. Q3041–Q3045, 2019, doi: 10.1149/2.0091907jss.

[13] D. Caligari Conti, 'What is a Photon?', 2016.

[14] J. H. Hubbell, 'Photon Mass Attenuation and Energy-absorption Coefficients from 1 keV to 20 MeV', *Int. J. Appl. Radiat. Isot*, vol. 33, pp. 1269–1290, 1982.

[15] Paul Schuurmans, *Kernfysica 2*. SCK CEN, 2021.

[16] B. E. A. Saleh and M. C. Teich, *Fundamentals of photonics*.

[17] V. Pakulin, 'What are photons?', doi: 10.13140/RG.2.2.22519.96165.

[18] 'European Medical', 2023. https://www.europeanmedical.info/emission-tomography/interaction-of-photons-with-matter.html (accessed Mar. 16, 2023).

[19] R. Hobbie and B. Roth, 'Interaction of Photons and Charged Particles with Matter', in *Intermediate Physics for Medicine and Biology*, 2007, pp. 401–435.

[20] 'Interactions of photons with matter and shape of spectra in X/γ-ray spectrometry'.

[21] D. F. Jackson and D. J. Hawkes, 'X-RAY ATTENUATION COEFFICIENTS OF ELEMENTS AND MIXTURES', North-Holland Publishing Company, 1981.

[22] A. Peres, *Quantum Theory: Concepts and Methods*, vol. 72. Kluwer Academic Publishers, 1994.

[23] J. H. Hubbell, 'Photon cross sections, attenuation coefficients, and energy absorption coefficients from 10 keV to 100 GeV', Gaithersburg, MD, 1969. doi: 10.6028/NBS.NSRDS.29.

[24] K. S. Krane, J. Wlley, N. York, C. Brisbane, and T. Singapore, *INTRODUCTORY NUCLEAR PHYSICS*. 1988.
[25] G. Erdi-Krausz, M. Matolin, B. Minty, J. P. Nicolet, and E. Schetselaar, *Guidelines for radioelement mapping using gamma ray spectrometry data*. International Atomic Energy Agency, 2003.
[26] T. J. Ross *et al.*, 'Neutron damage tests of a highly segmented germanium crystal', *Nucl Instrum Methods Phys Res A*, vol. 606, no. 3, pp. 533–544, Jul. 2009, doi: 10.1016/j.nima.2009.04.024.
[27] G. F. Knoll, *Radiation detection and measurement*. Wiley, 2000.
[28] S. Hamouda and S. A. Hamouda, 'Compton Scattering: A Theory and Experiments', *International Journal of Geology, Agriculture and Environmental Sciences*, vol. 5, no. 4, 2017.
[29] A. H. Compton, 'A QUANTUM THEORY OF THE SCATTERING OF X-RAYS BY LIGHT ELEMENTS', *Phys Rev*, vol. 21, 1923.
[30] N. A. Dyson, *X-RAYS in atomic and nuclear physics*. Cambridge: Cambridge University Press, 1990. doi: https://doi.org/10.1017/CBO9780511470806.
[31] N. Reguigui, *Gamma Ray Spectrometry*. 2014.
[32] S. Hamouda, 'Data reduction for high gamma-ray compton spectroscopy', pp. 541–543, 2013.
[33] R. Wirawan, A. Waris, M. Djamal, and G. Handayani, 'Simulation of energy absorption spectrum in NaI crystal detector for multiple gamma energy using Monte Carlo method', in *AIP Conference Proceedings*, American Institute of Physics Inc., Apr. 2015. doi: 10.1063/1.4917139.
[34] D. Bailey and J. Harlow, 'GE The Germanium Spectrometer', 2011.
[35] A. Simon, 'First sum spectra obtained with the SuN detector', 2016. https://groups.nscl.msu.edu/SuN/SuN_spectra.php (accessed Mar. 16, 2023).
[36] C. Michael Lederer and S. Virginia, *Table of Isotopes* , 7th ed. Wiley, 1978.
[37] E. Brown and R. Firestone, *Table of Radioactive Isotopes*. Wiley & Sons, Incorporated, John, 1986.
[38] M.-M. Bé *et al.*, *Table of radionuclides. (Vol. 7 A=14 to 245)*. BIPM, 2013.
[39] 'Radioisotopes and Radiation Methodology: Chapter 7 Semiconductor Detectors'.
[40] B. L. Wall *et al.*, 'Dead layer on silicon p-i-n diode charged-particle detectors', *Nucl Instrum Methods Phys Res A*, vol. 744, pp. 73–79, Apr. 2014, doi: 10.1016/j.nima.2013.12.048.
[41] M. Hult *et al.*, 'Determination of homogeneity of the top surface deadlayer in an old HPGe detector', *Applied Radiation and Isotopes*, vol. 147, pp. 182–188, May 2019, doi: 10.1016/j.apradiso.2019.02.019.
[42] H. D. Chuong, T. T. Thanh, L. T. Ngoc Trang, V. H. Nguyen, and C. Van Tao, 'Estimating thickness of the inner dead-layer of n-type HPGe detector', *Applied Radiation and Isotopes*, vol. 116, pp. 174–177, Oct. 2016, doi: 10.1016/j.apradiso.2016.08.010.
[43] S. Hurtado, M. Garcia-Leon, and R. Garcia-Tenorio, 'Monte Carlo simulation of the response of a germanium detector for low-level spectrometry measurements using GEANT4', *Appl Radiat Isot*, vol. 61, pp. 43–139, 2004.
[44] V. Peyres and E. García-Toraño, 'Efficiency calibration of an extended-range Ge detector by a detailed Monte Carlo simulation', *Nucl Instrum Methods Phys Res A*, vol. 580, no. 1 SPEC. ISS., pp. 296–298, Sep. 2007, doi: 10.1016/j.nima.2007.05.160.

[45] F. Padilla Cabal *et al.*, 'Monte Carlo based geometrical model for efficiency calculation of an n-type HPGe detector', *Applied Radiation and Isotopes*, vol. 68, no. 12, pp. 2403–2408, Dec. 2010, doi: 10.1016/j.apradiso.2010.06.018.
[46] A. A. Ridha, 'Determination of Radionuclides Concentrations in Construction Materials Used in Iraq', Republic of Iraq Ministry of Higher Education And Scientific Research University of Al-Mustansiriyah College of Science, 2013. doi: 10.13140/RG.2.1.3815.0640.
[47] P. Lecoq, 'Scintillation Detectors for Charged Particles and Photons', in *Particle Physics Reference Library*, Springer International Publishing, 2020, pp. 45–89. doi: 10.1007/978-3-030-35318-6_3.
[48] K. Kok, *Nuclear Engineering Handbook*.
[49] H. Karen, 'Germanium Detectors User's Manual', 2017.
[50] 'High-Performance Germanium Coaxial Detectors for Safeguards and Non-Destructive Assay Product Configuration Guide', 2022.
[51] T. D. C. Busarello, M. G. Simões, and J. A. Pomilio, 'Semiconductor Diodes and Transistors', in *Power Electronics Handbook, Fourth Edition*, Elsevier, 2017, pp. 15–48. doi: 10.1016/B978-0-12-811407-0.00002-7.
[52] H. Spieler, 'Semiconductor Detector Systems', Clarendon Press, Oxford, 2005.
[53] N. Owtscharenko, 'Semiconductor detectors and electronics Master lab course', 2022.
[54] International Atomic Energy Agency, *Instrumentation for digital nuclear spectroscopy*.
[55] 'Genie™ 2000 Spectroscopy Software Operations', 2006.
[56] M. Smirnova *et al.*, 'LaBr3(Ce) gamma-ray detector for neutron capture therapy', in *Journal of Physics: Conference Series*, Institute of Physics Publishing, 2016. doi: 10.1088/1742-6596/675/4/042050.
[57] 'Mirion technologies: Genie2000'. Mirion technologies: Genie2000 (accessed Mar. 24, 2023).
[58] 'EGSnrc HPGE3_a MC simulation code for HPGe efficiency'.
[59] M. Hult, 'Low-level gamma-ray spectrometry using Ge-detectors', *Metrologia*, vol. 44, no. 4, Aug. 2007, doi: 10.1088/0026-1394/44/4/S12.
[60] O. Serra, 'Natural Gamma-Ray spectrometry', *Developments in Petroleum Science*, vol. 15, pp. 113–134, 1984.
[61] P. Lindahl, 'Efficiency calibration of gamma detector T2', Geel, 2005.
[62] E. Wieslander, 'Calibration of detector T4 in Lab-8', Geel, 2000.
[63] T. Vidmar, 'EFFTRAN - A Monte Carlo efficiency transfer code for gamma-ray spectrometry', *Nucl Instrum Methods Phys Res A*, vol. 550, no. 3, pp. 603–608, Sep. 2005, doi: 10.1016/j.nima.2005.05.055.
[64] R. Tuo and C. F. Jeff Wu, 'Efficient calibration for imperfect computer models', *Ann Stat*, vol. 43, no. 6, pp. 2331–2352, Dec. 2015, doi: 10.1214/15-AOS1314.
[65] V. V. Golovko, 'Simplified efficiency calibration methods for semiconductor detectors used in criticality dosimetry', *Applied Radiation and Isotopes*, vol. 187, Sep. 2022, doi: 10.1016/j.apradiso.2022.110335.
[66] C. C. Conti, I. C. P. Salinas, and H. Zylberberg, 'A detailed procedure to simulate an HPGe detector with MCNP5', *Progress in Nuclear Energy*, vol. 66, pp. 35–40, 2013, doi: 10.1016/j.pnucene.2013.03.003.

[67] A. S. E. Santo, F. G. Wasserman, and C. C. Conti, ‘HPGe well detector calibration procedure by MCNP5 Monte Carlo computer code’, *Ann Nucl Energy*, vol. 46, pp. 213–217, Aug. 2012, doi: 10.1016/j.anucene.2012.03.037.

Appendix list

Appendix A: Relative efficiency difference graphs of Ge-T10

The numbers following each graph have the following meaning:
In black: mean and absolute standard deviation for all energies
In red: mean and absolute standard deviation for energies without Europium FEPs
In Green: mean and absolute standard deviation for only energies of Europium

This was done since Europium showed deviations during this process.

Original

Crystal distance: 0 cm Top Deadlayer: 0.4 um Side Deadlayer: 0.05 cm

Mean dev.	-6.29 [%]	Mean dev.	-7.73 [%]	Mean dev.	-4.94 [%]
Stdev of dev.	3.10 [%]	Stdev of dev.	3.09 [%]	Stdev of dev.	1.85 [%]

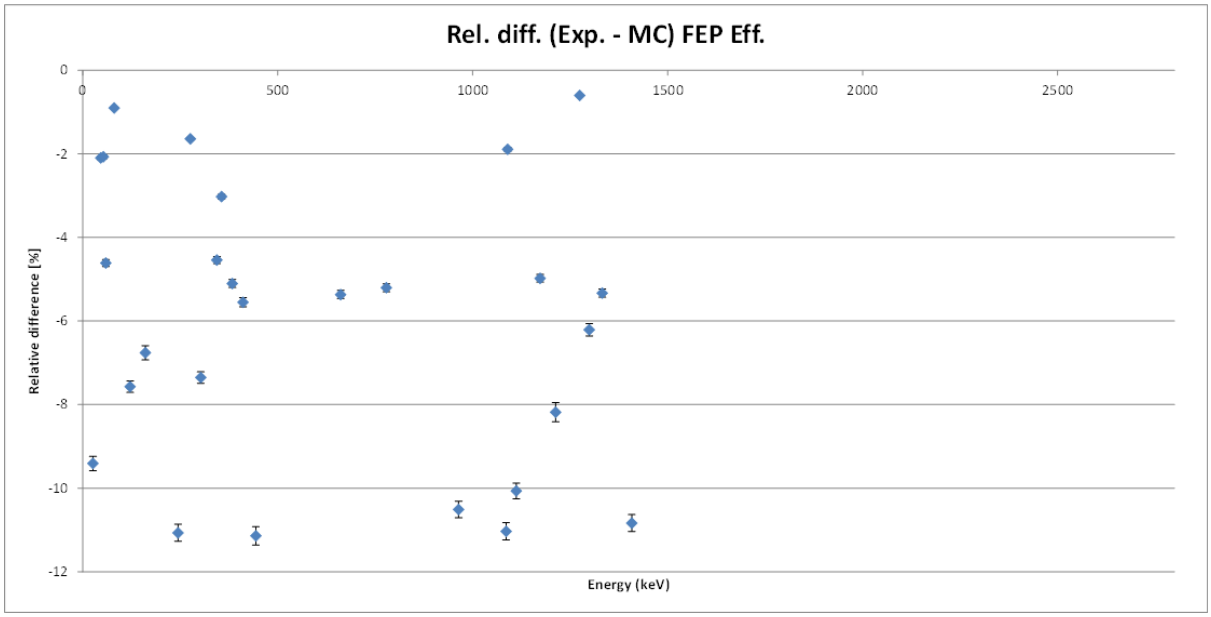

Crystal distance: +0.1 cm Top Deadlayer: 0.4 um Side Deadlayer: 0.05 cm

Mean dev.	-8.68 [%]	Mean dev.	-10.18 [%]	Mean dev.	-6.93 [%]
Stdev of dev.	3.26 [%]	Stdev of dev.	2.84 [%]	Stdev of dev.	2.67 [%]

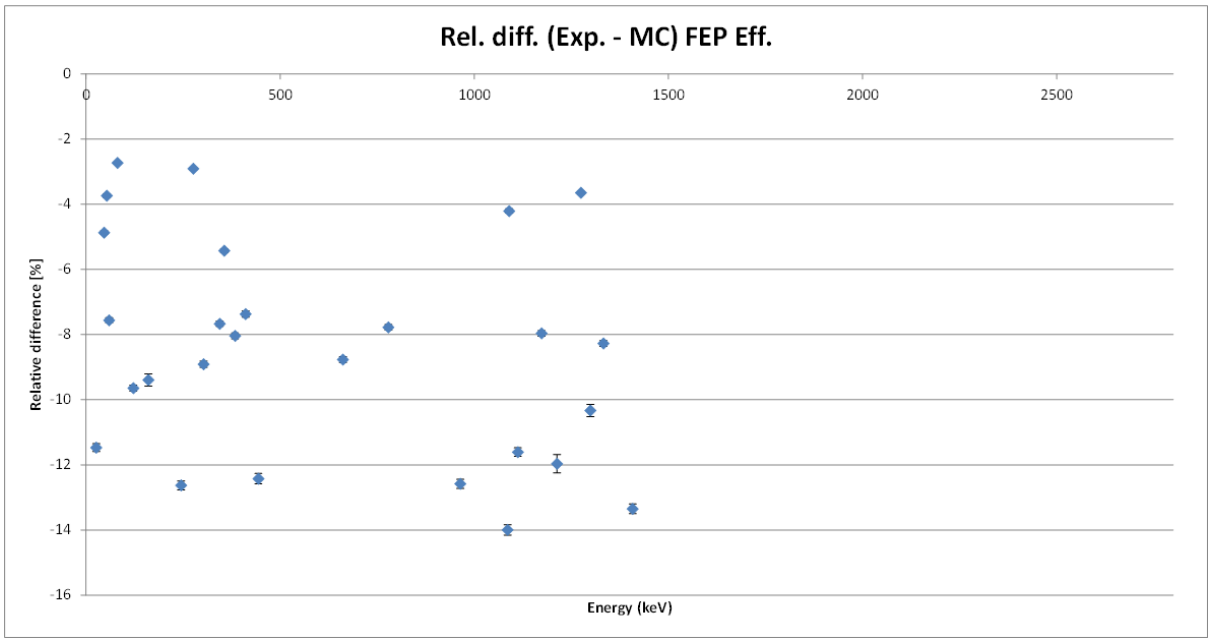

Crystal distance: +0.2 cm Top Deadlayer: 0.4 um Side Deadlayer: 0.05 cm

Mean dev.	-11.32 [%]	Mean dev.	-12.43 [%]	Mean dev.	-9.86 [%]
Stdev of dev.	3.27 [%]	Stdev of dev.	2.88 [%]	Stdev of dev.	3.08 [%]

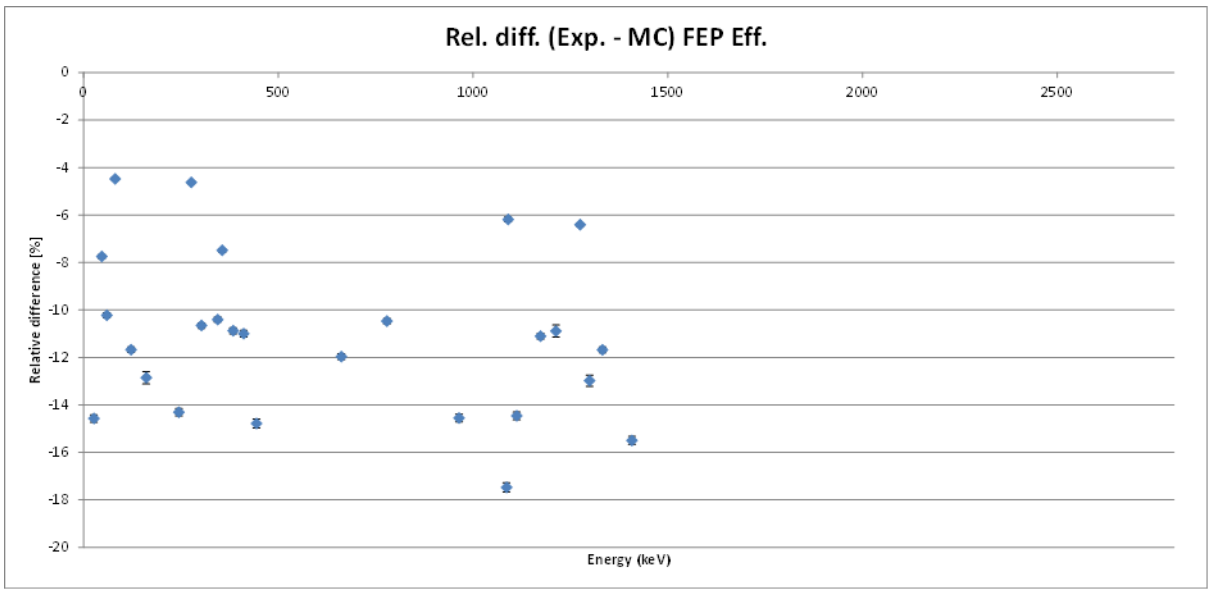

Crystal distance: -0.1 cm Top Deadlayer: 0.4 um Side Deadlayer: 0.05 cm

Mean dev.	-3.75 [%]	Mean dev.	-5.36 [%]	Mean dev.	-1.85 [%]
Stdev of dev.	3.68 [%]	Stdev of dev.	3.92 [%]	Stdev of dev.	2.24 [%]

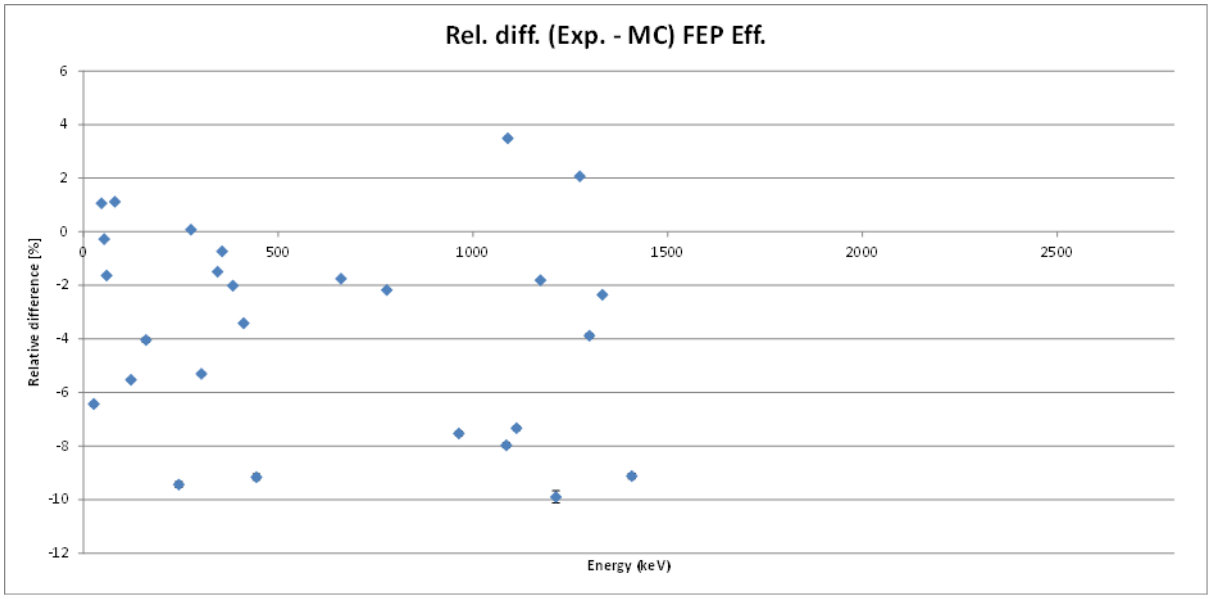

Crystal distance: -0.2 cm Top Deadlayer: 0.4 um Side Deadlayer: 0.05 cm

Mean dev.	-0.70 [%]	Mean dev.	-3.50 [%]	Mean dev.	0.47 [%]
Stdev of dev.	2.76 [%]	Stdev of dev.	3.34 [%]	Stdev of dev.	1.78 [%]

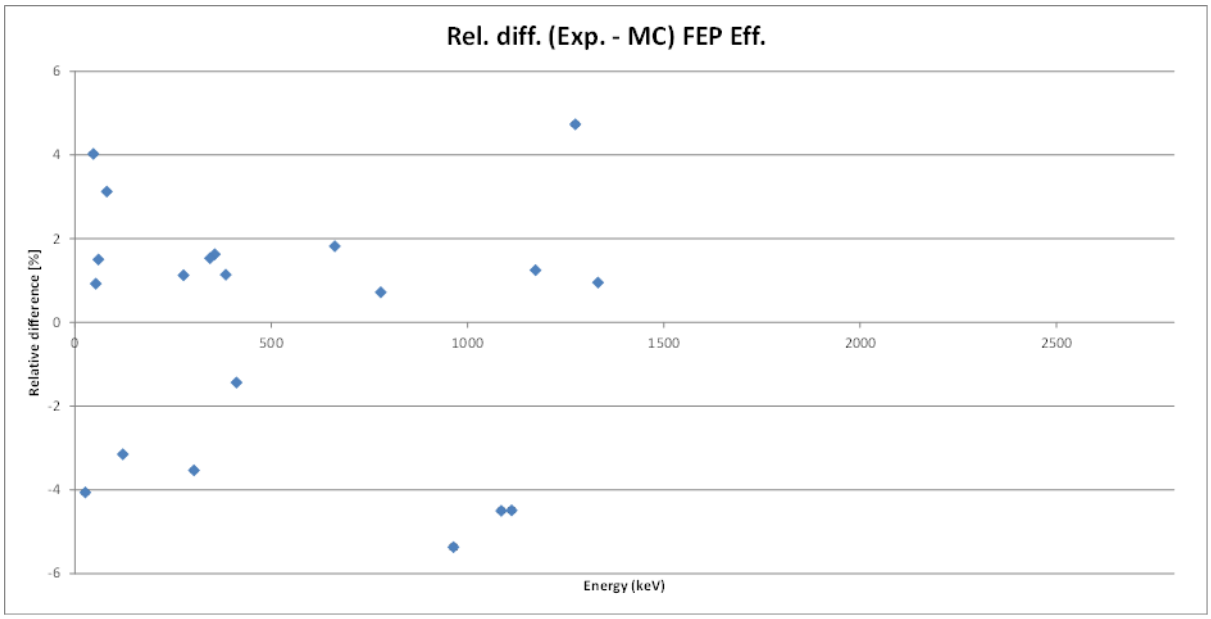

Crystal distance: -0.25 cm Top Deadlayer: 0.4 um Side Deadlayer: 0.05 cm

Mean dev.	0.26 [%]	Mean dev.	-1.29 [%]	Mean dev.	2.11 [%]
Stdev of dev.	3.86 [%]	Stdev of dev.	4.26 [%]	Stdev of dev.	2.83 [%]

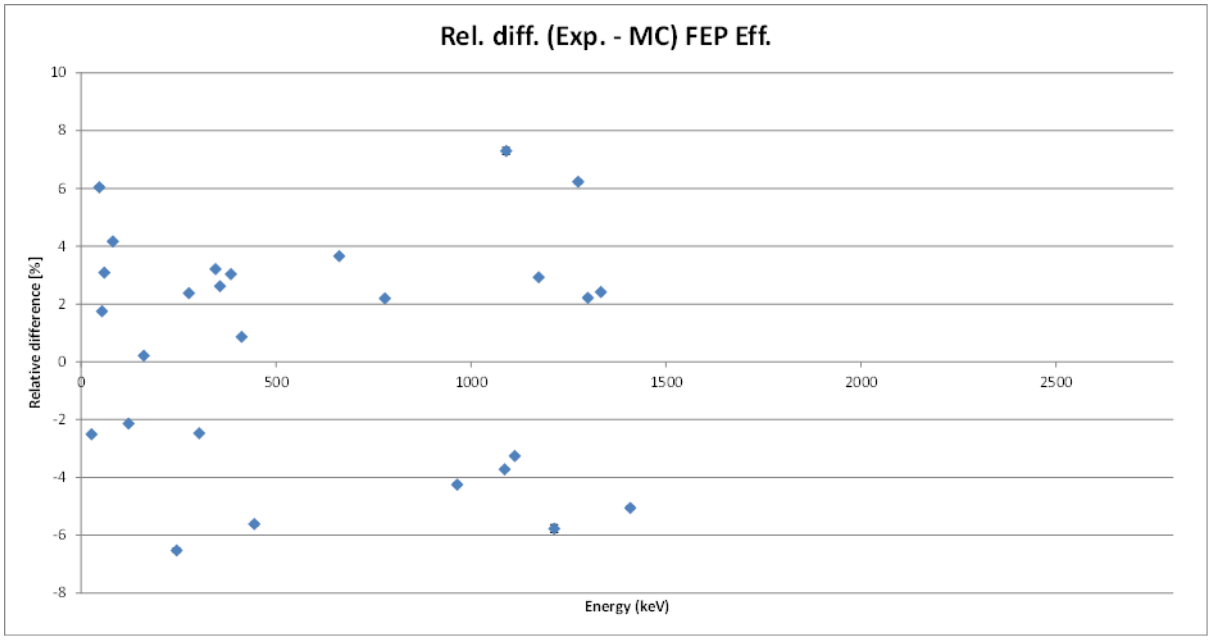

Crystal distance: -0.3 cm Top Deadlayer: 0.4 um Side Deadlayer: 0.05 cm

Mean dev.	1.66 [%]	Mean dev.	0.03 [%]	Mean dev.	3.59 [%]
Stdev of dev.	3.97 [%]	Stdev of dev.	4.37 [%]	Stdev of dev.	2.39 [%]

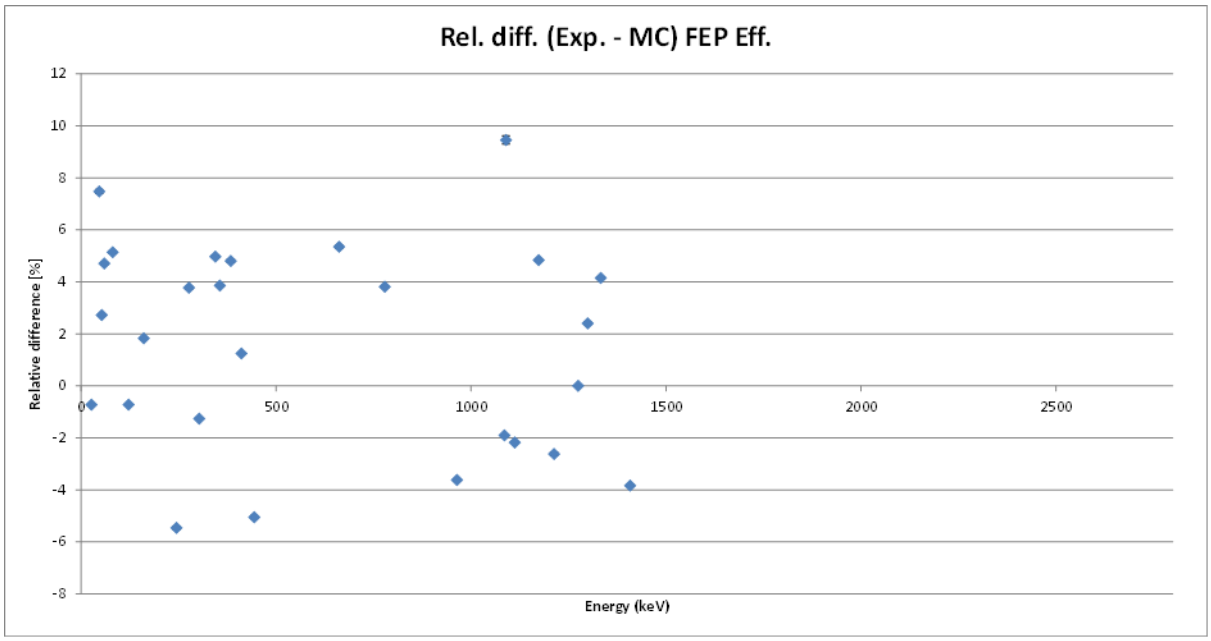

Crystal distance: -0.4 cm Top Deadlayer: 0.4 um Side Deadlayer: 0.05 cm

Mean dev.	4.34 [%]	Mean dev.	2.63 [%]	Mean dev.	6.33 [%]
Stdev of dev.	4.54 [%]	Stdev of dev.	5.20 [%]	Stdev of dev.	2.84 [%]

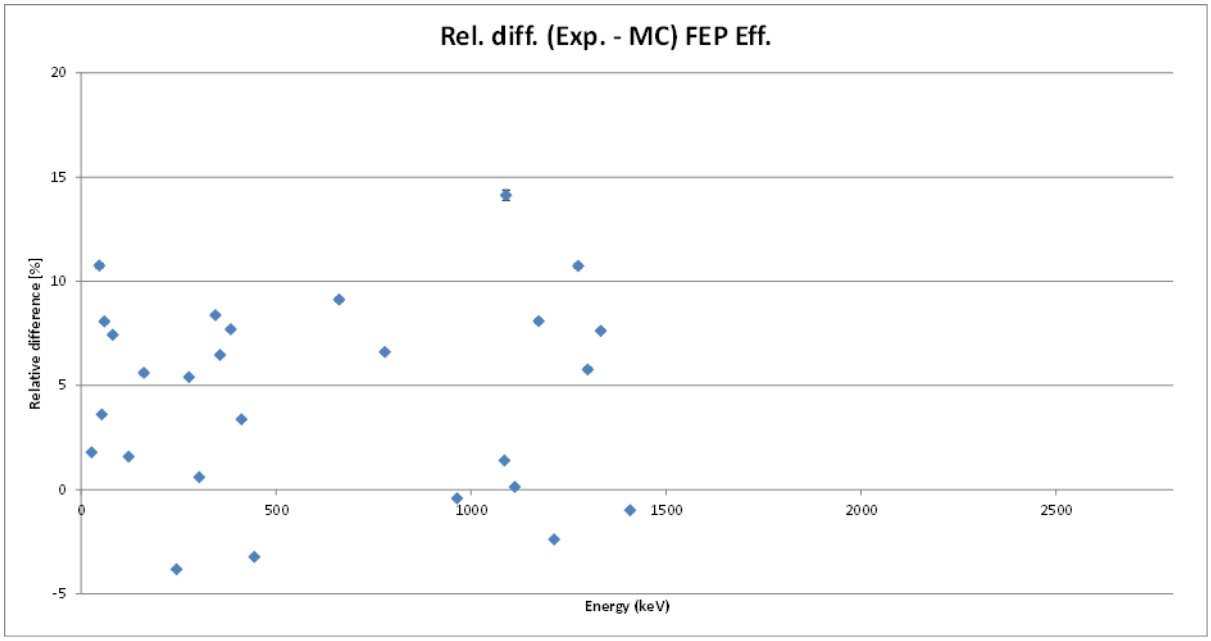

Crystal distance: -0.5 cm Top Deadlayer: 0.4 um Side Deadlayer: 0.05 cm

Mean dev.	7.16 [%]	Mean dev.	5.34 [%]	Mean dev.	9.28 [%]
Stdev of dev.	4.85 [%]	Stdev of dev.	5.33 [%]	Stdev of dev.	3.36 [%]

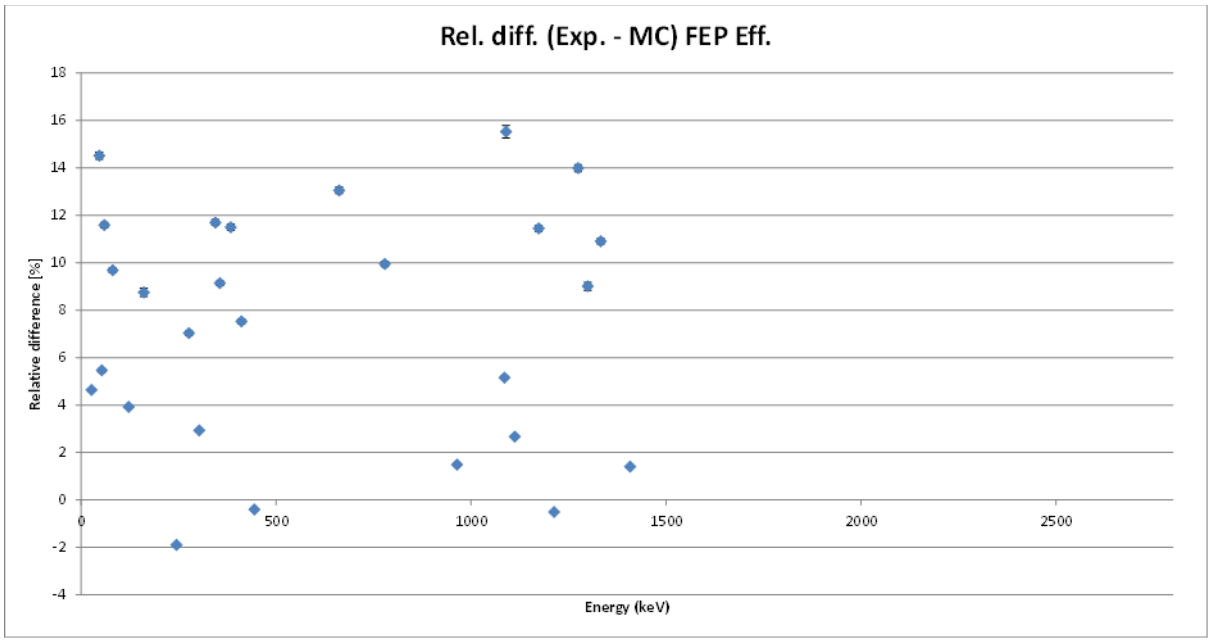

Top DeadLayer change

Crystal distance: 0 cm Top Deadlayer: 0 um Side Deadlayer: 0.05 cm

Mean dev.	-6.25 [%]	Mean dev.	-7.79 [%]	Mean dev.	-4.48 [%]
Stdev of dev.	3.38 [%]	Stdev of dev.	3.30 [%]	Stdev of dev.	2.45 [%]

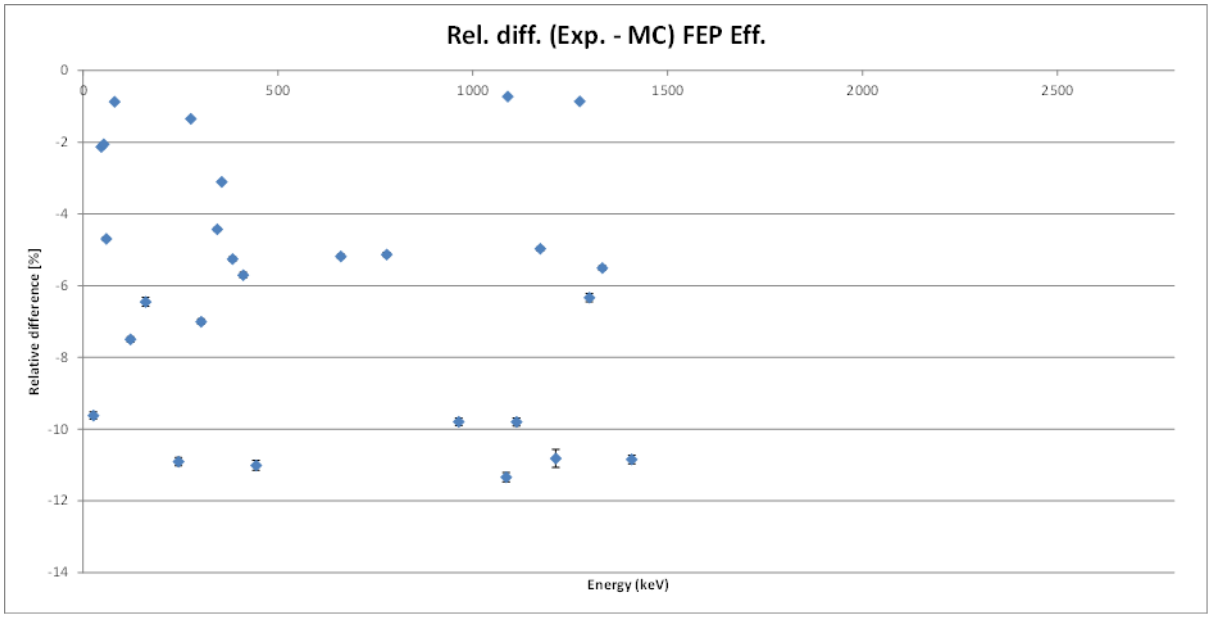

Original

Crystal distance: 0 cm Top Deadlayer: 0.4 um Side Deadlayer: 0.05 cm

Mean dev.	-6.79 [%]	Mean dev.	-7.73 [%]	Mean dev.	-4.94 [%]
Stdev of dev.	3.10 [%]	Stdev of dev.	3.09 [%]	Stdev of dev.	1.85 [%]

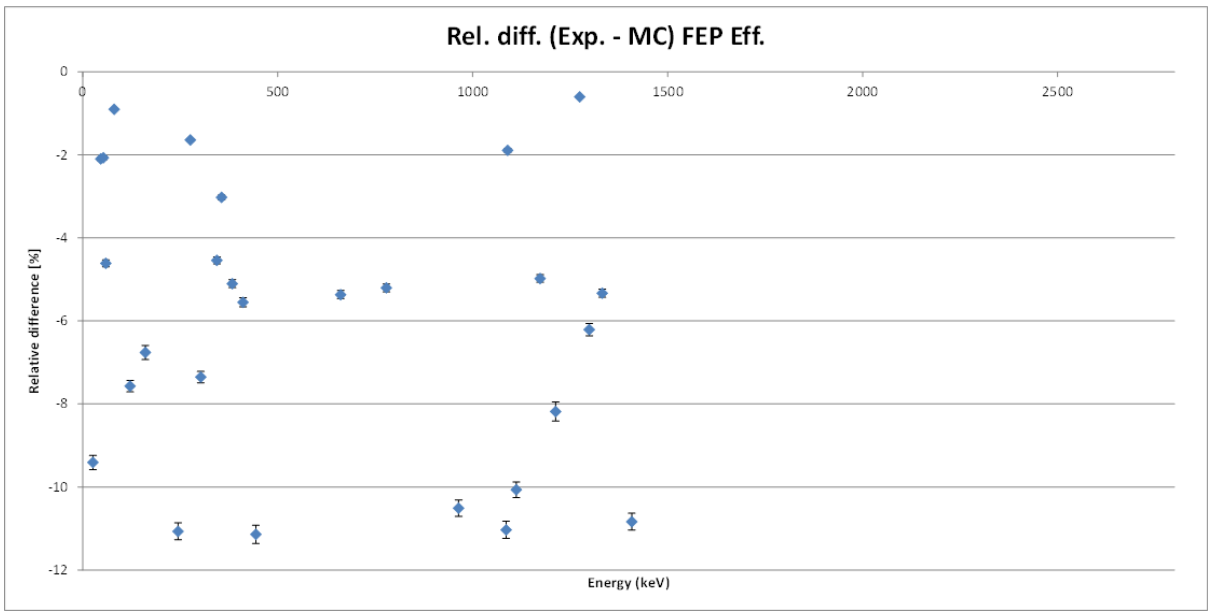

Crystal distance: 0 cm Top Deadlayer: 0.8 um Side Deadlayer: 0.05 cm

Mean dev.	-6.20 [%]	Mean dev.	-7.68 [%]	Mean dev.	-4.45 [%]
Stdev of dev.	3.27 [%]	Stdev of dev.	3.12 [%]	Stdev of dev.	2.36 [%]

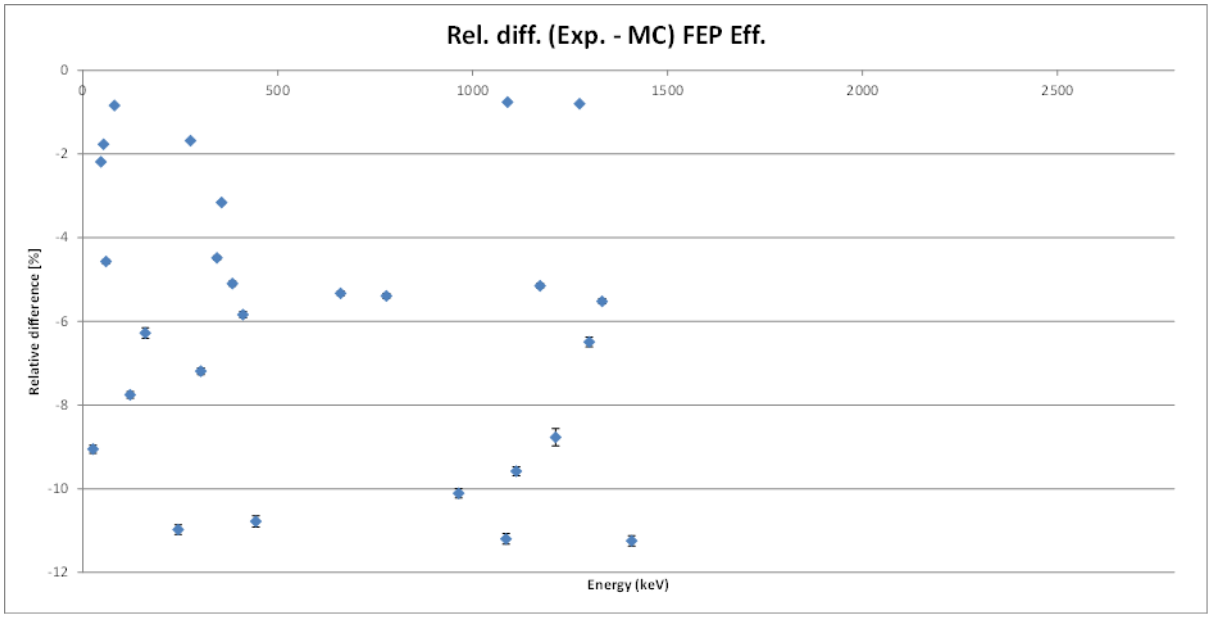

Side DeadLayer change

Crystal distance: 0 cm Top Deadlayer: 0.4 um Side Deadlayer: 0 cm

Mean dev.	-9.42 [%]	Mean dev.	-10.00 [%]	Mean dev.	-7.44 [%]
Stdev of dev.	3.08 [%]	Stdev of dev.	2.75 [%]	Stdev of dev.	2.58 [%]

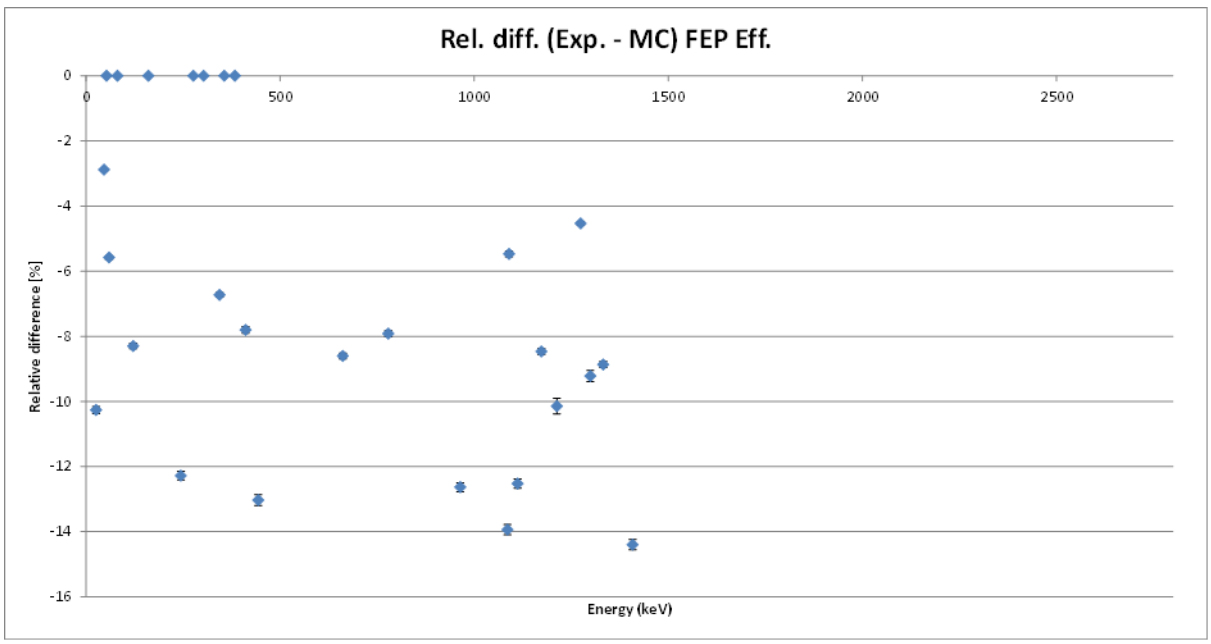

Original

Crystal distance: 0 cm Top Deadlayer: 0.4 um Side Deadlayer: 0.05 cm

Mean dev. -6.79 [%]	Mean dev. -7.73 [%]	Mean dev. -4.99 [%]
Stdev of dev. 3.10 [%]	Stdev of dev. 3.09 [%]	Stdev of dev. 1.85 [%]

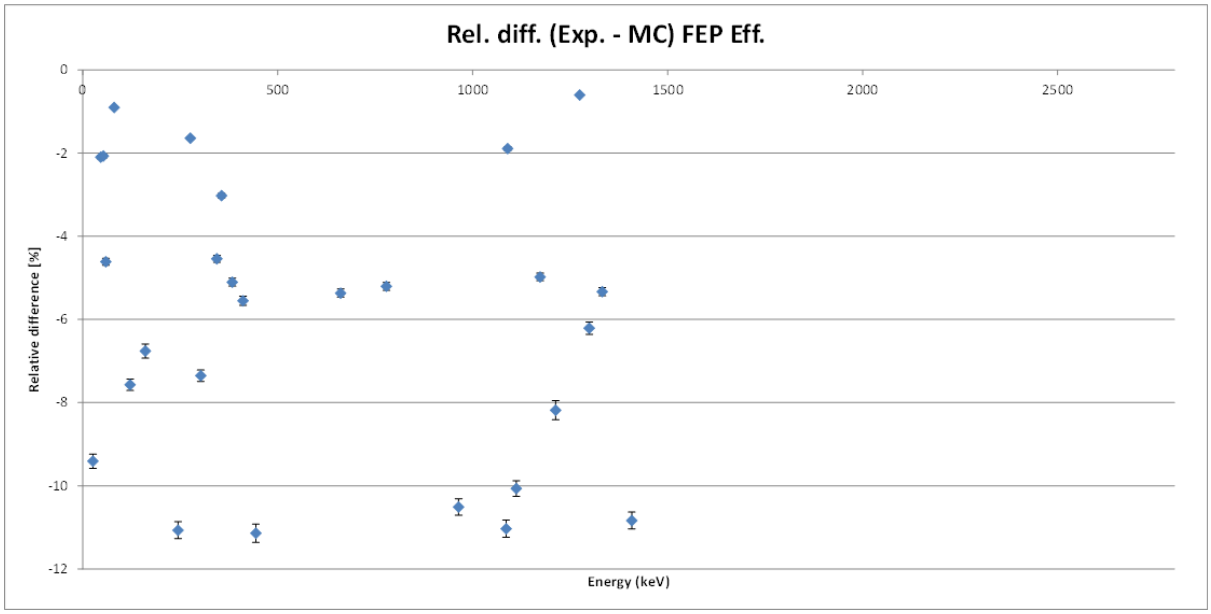

Crystal distance: 0 cm Top Deadlayer: 0.4 um Side Deadlayer: 0.075 cm

Mean dev. -5.11 [%]	Mead dev. -6.43 [%]	Mean dev. -3.59 [%]
Stdev of dev. 3.16 [%]	Stdev of dev. 3.20 [%]	Stdev of dev 2.39 [%]

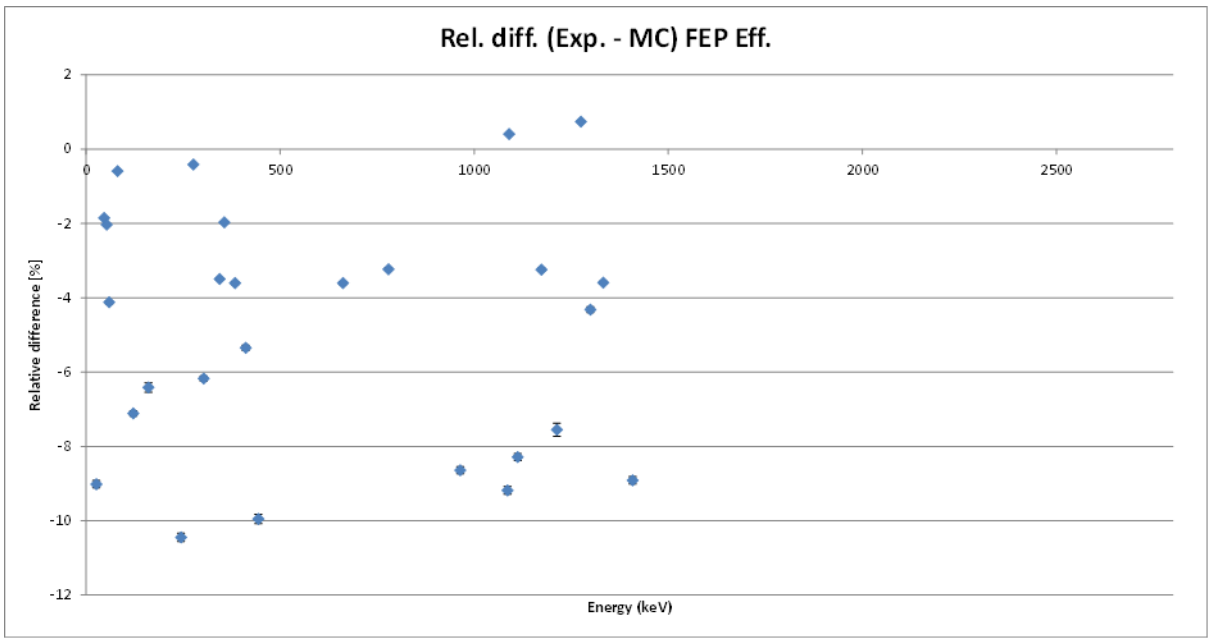

Crystal distance: 0 cm Top Deadlayer: 0.4 um Side Deadlayer: 0.1 cm

Mean dev.	-4.00 [%]	Mean dev.	-5.14 [%]	Mean dev.	-2.61 [%]
Stdev of dev.	3.25 [%]	Stdev of dev.	3.49 [%]	Stdev of dev.	2.35 [%]

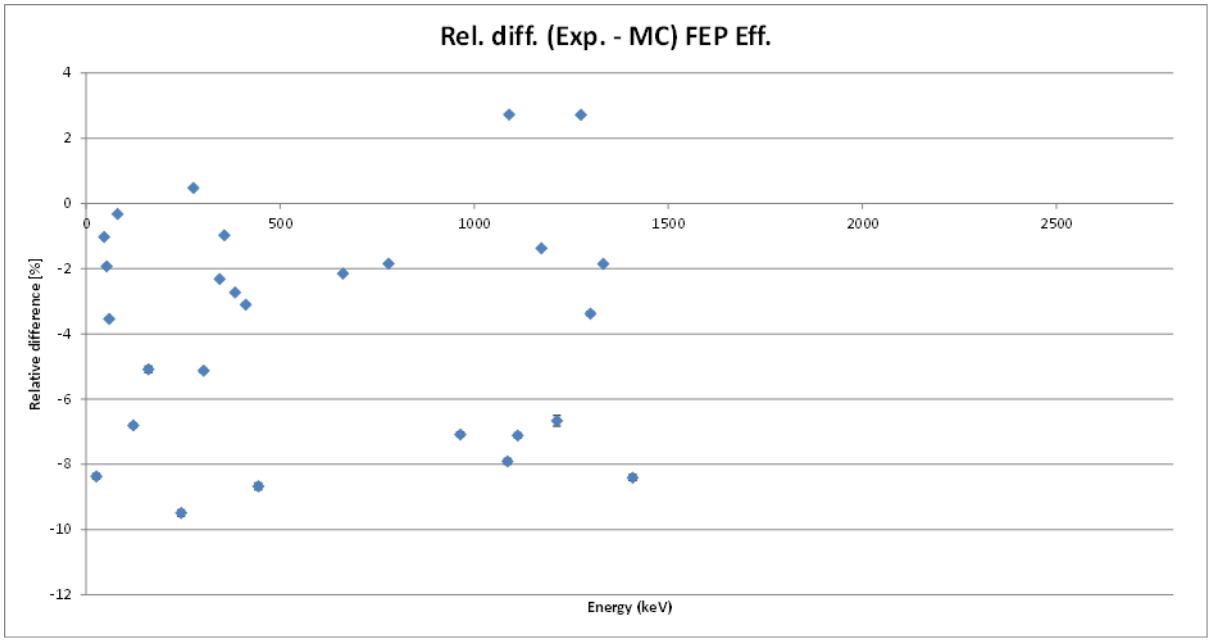

Europium discussion (Eu in red)

Crystal distance: -0.2 cm Top Deadlayer: 0.4 um Side Deadlayer: 0.05 cm

Mean dev.	-1.99 [%]	Mean dev.	-3.50 [%]	Mean dev.	0.47 [%]
Stdev of dev.	3.45 [%]	Stdev of dev.	3.34 [%]	Stdev of dev.	1.78 [%]

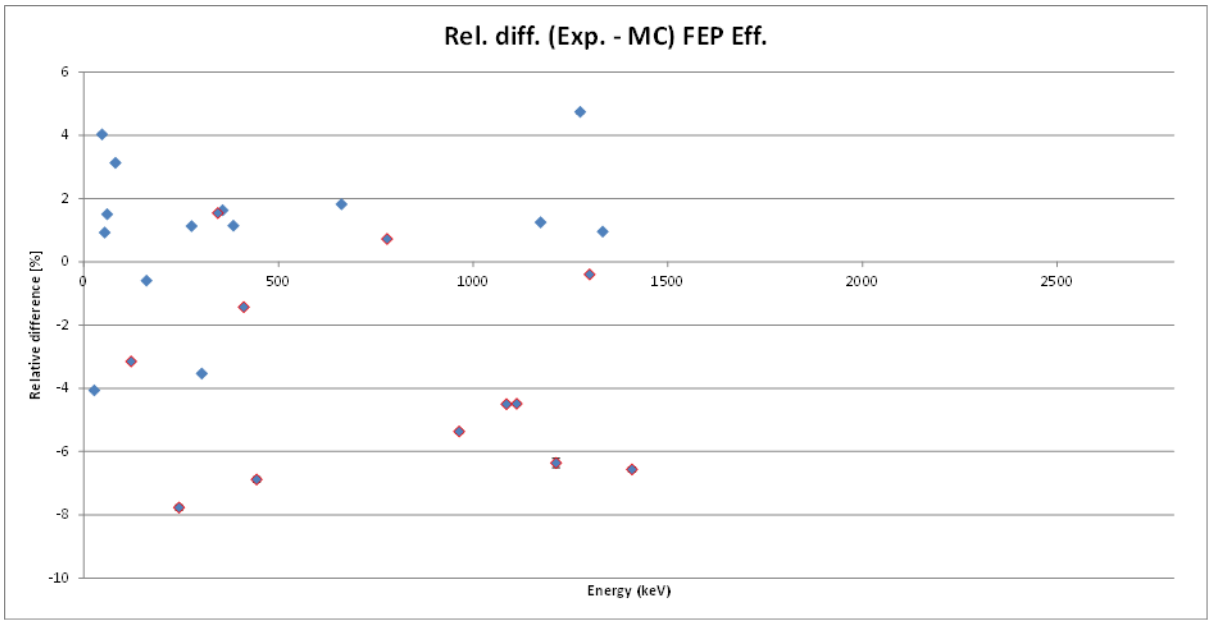

Crystal distance: -0.25 cm Top Deadlayer: 0.4 um Side Deadlayer: 0.05 cm

Mean dev. 0.26 [%] Mean dev. -1.29 [%] Mean dev. 2.11 [%]
Stdev of dev. 3.86 [%] Stdev of dev. 4.26 [%] Stdev of dev. 2.83 [%]

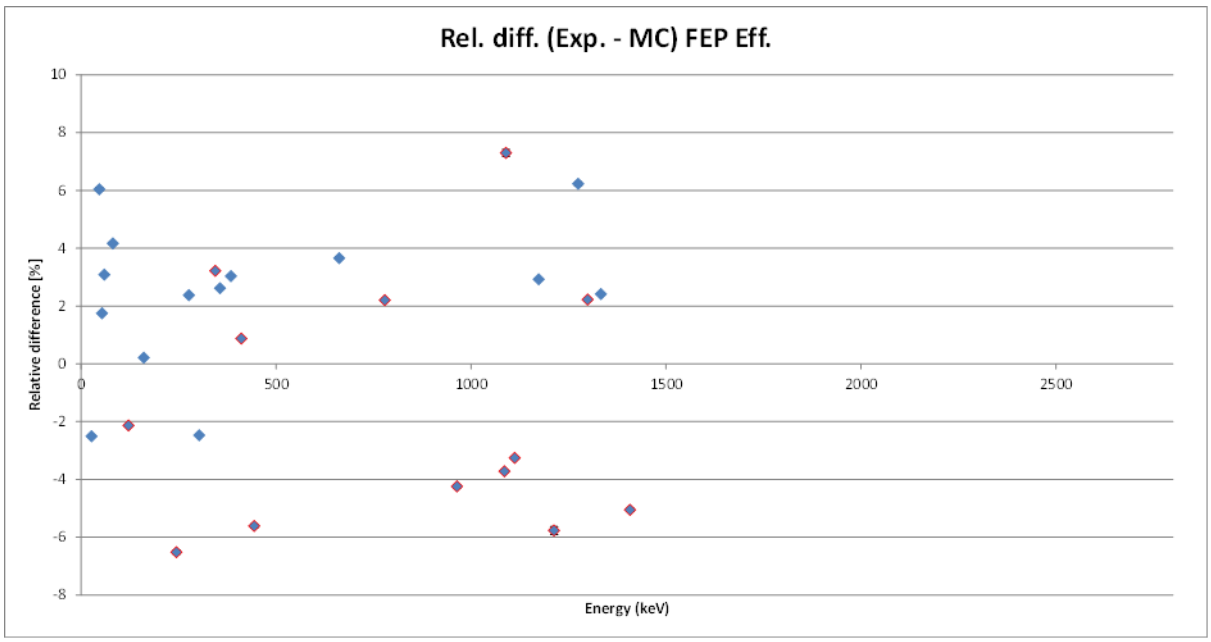

Crystal distance: -0.2 cm Top Deadlayer: 0.4 um Side Deadlayer: 0.05 cm (without Europium) → Als we hiervan uitgaan wrs 1.8-1.9 of met SD

Mean dev. 0.47 [%]
Stdev of dev. 2.83 [%]

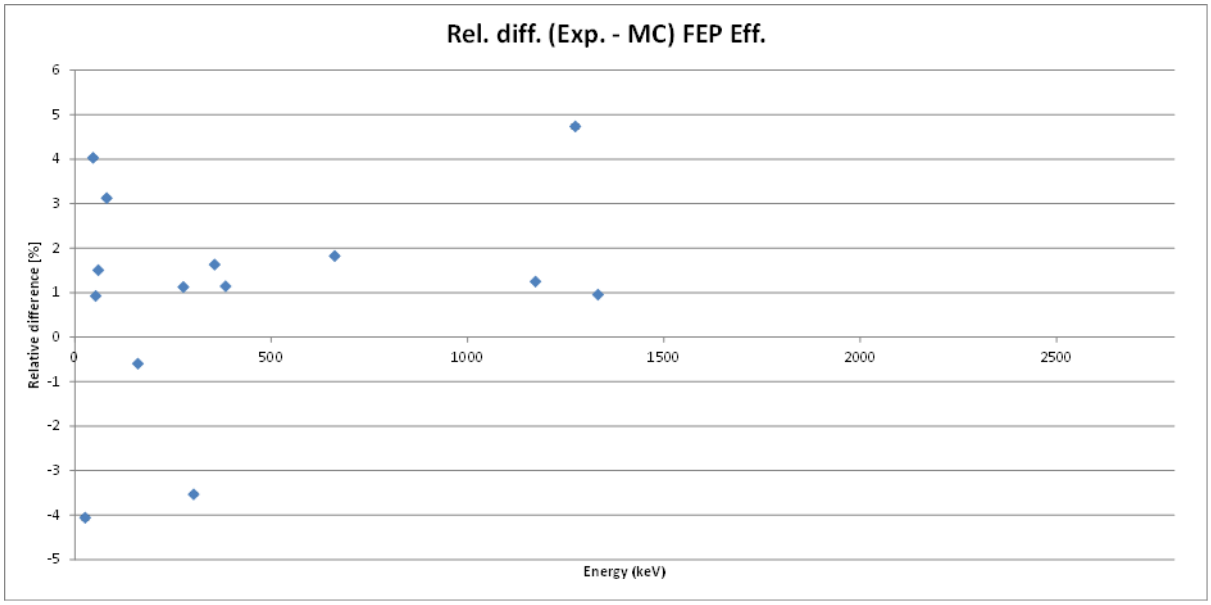

<u>Crystal distance:</u> -0.2 cm <u>Top Deadlayer:</u> 0.4 um <u>Side Deadlayer:</u> 0.05 cm (only Eu)

Mean dev. -3.50 [%]
Stdev of dev. 3.34 [%]

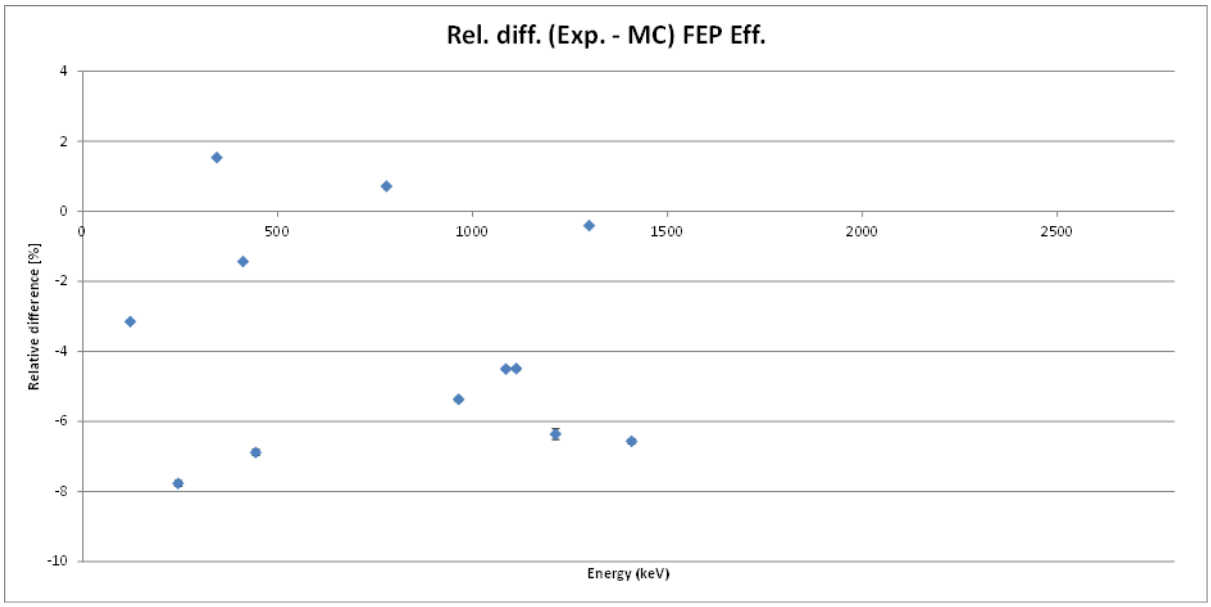

FINAL MODEL

<u>Crystal distance:</u> -0.15 cm <u>Top Deadlayer:</u> 0.4 um <u>Side Deadlayer:</u> 0.1 cm <u>Endcap</u>: 0.15 cm

Mean dev. 0.82%	Mean dev. -1.05%	Mean dev. 3.31%
Stdev of dev. 3.79%	Stdev of dev. 3.89%	Stdev of dev. 1.64%

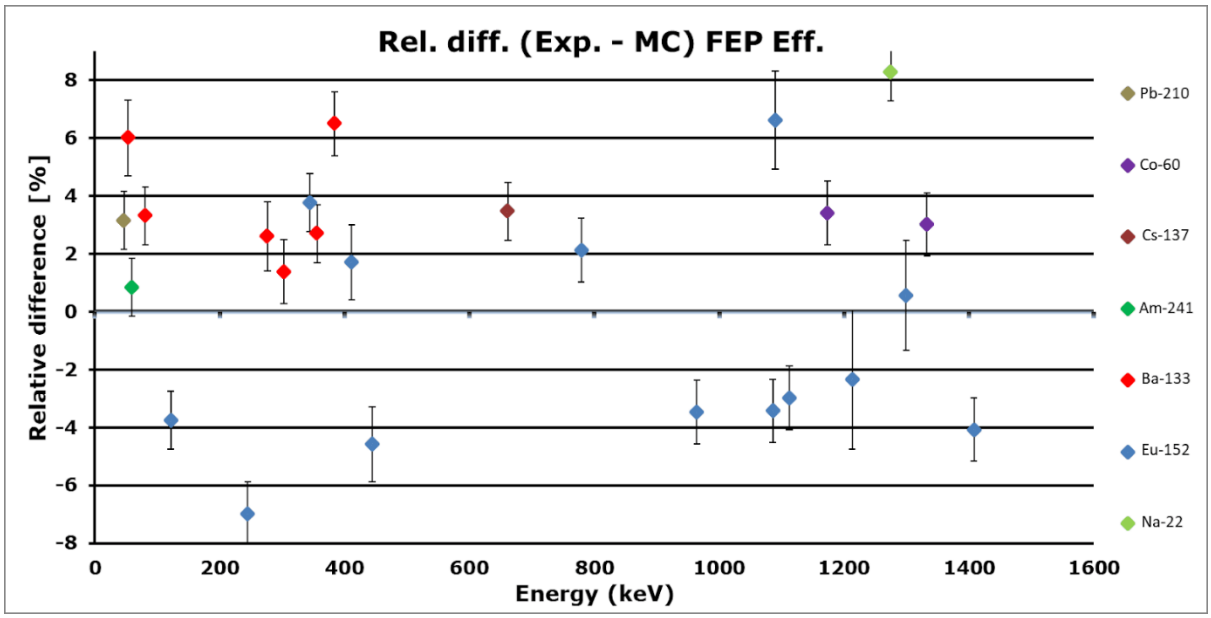

Validation: change in distance: holder 133 + 110 (4 cm)

Original

Crystal distance: 0 cm Top Deadlayer: 0.4 um Side Deadlayer: 0.05 cm

Mean dev. -5.73%	Mean dev. -6.96%	Mean dev. -4.41%
Stdev of dev. 2.66%	Stdev of dev. 2.82%	Stdev of dev. 1.83%

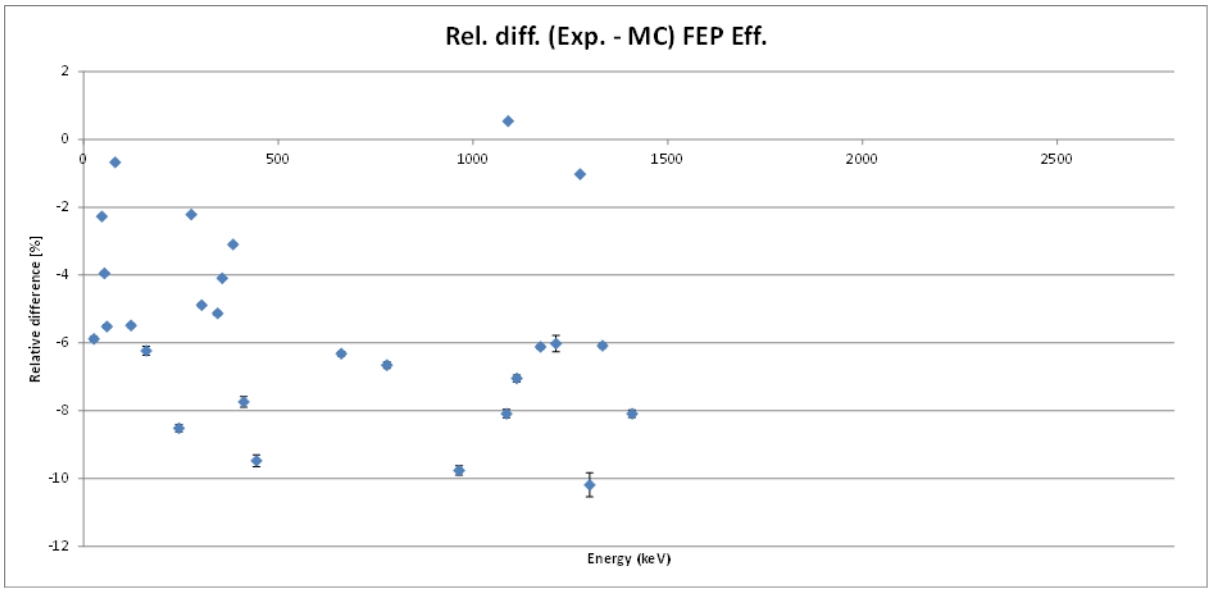

Crystal distance: -0.2 cm Top Deadlayer: 0.4 um Side Deadlayer: 0.05 cm

Mean dev. -1.59%	Mean dev. -3.06%	Mean dev. -0.08%
Stdev of dev. 2.65%	Stdev of dev. 2.52%	Stdev of dev. 1.92%

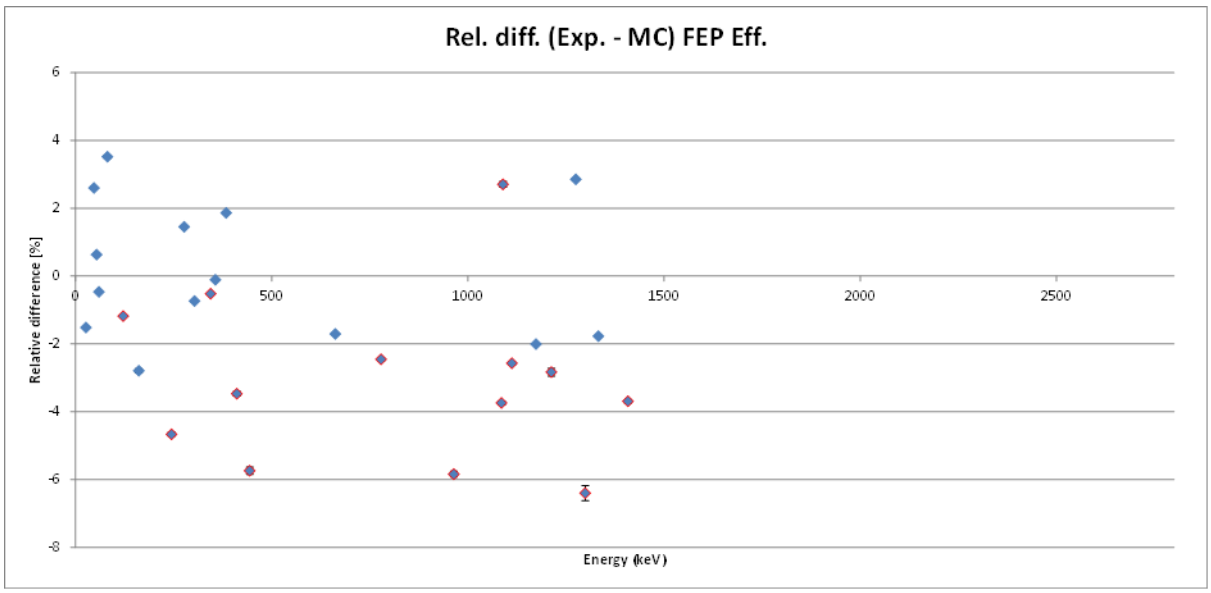

Crystal distance: -0.15 cm Top Deadlayer: 0.4 um Side Deadlayer: 0.1 cm

Mean dev.	-0.72%	Mean dev.	-0.12%	Mean dev.	-1.63%
Stdev of dev.	2.42%	Stdev of dev.	2.70%	Stdev of dev.	1.87%

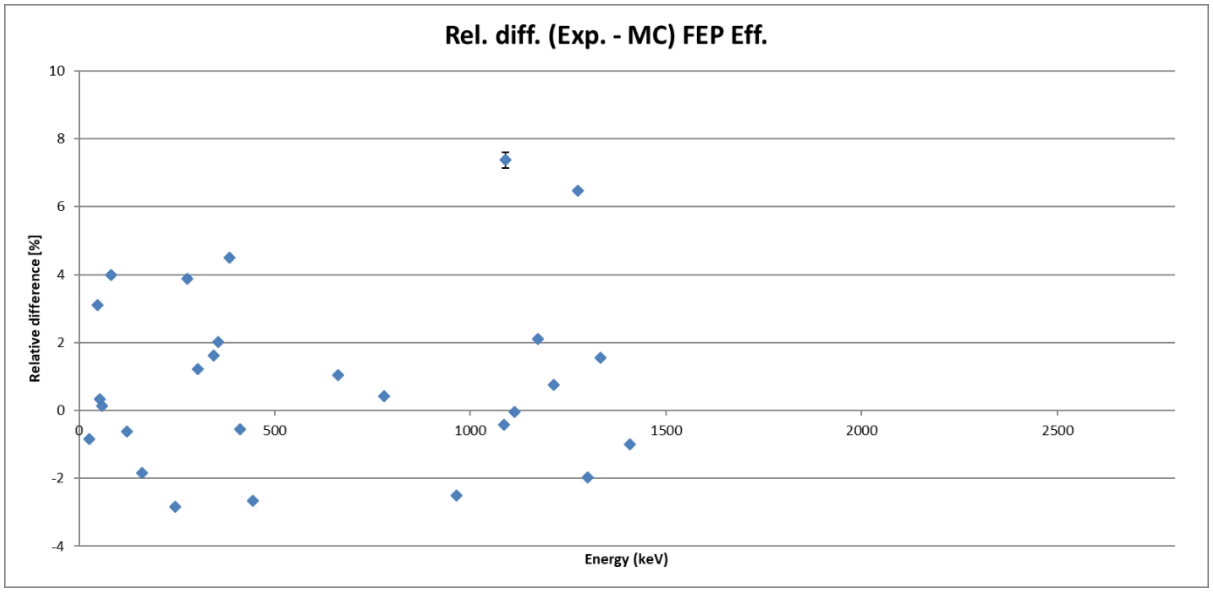

Crystal distance: -0.18 cm Top Deadlayer: 0.4 um Side Deadlayer: 0.1 cm

Mean dev.	-1.41%	Mean dev.	-0.43%	Mean dev.	2.40%
Stdev of dev.	2.41%	Stdev of dev.	2.73%	Stdev of dev.	1.72%

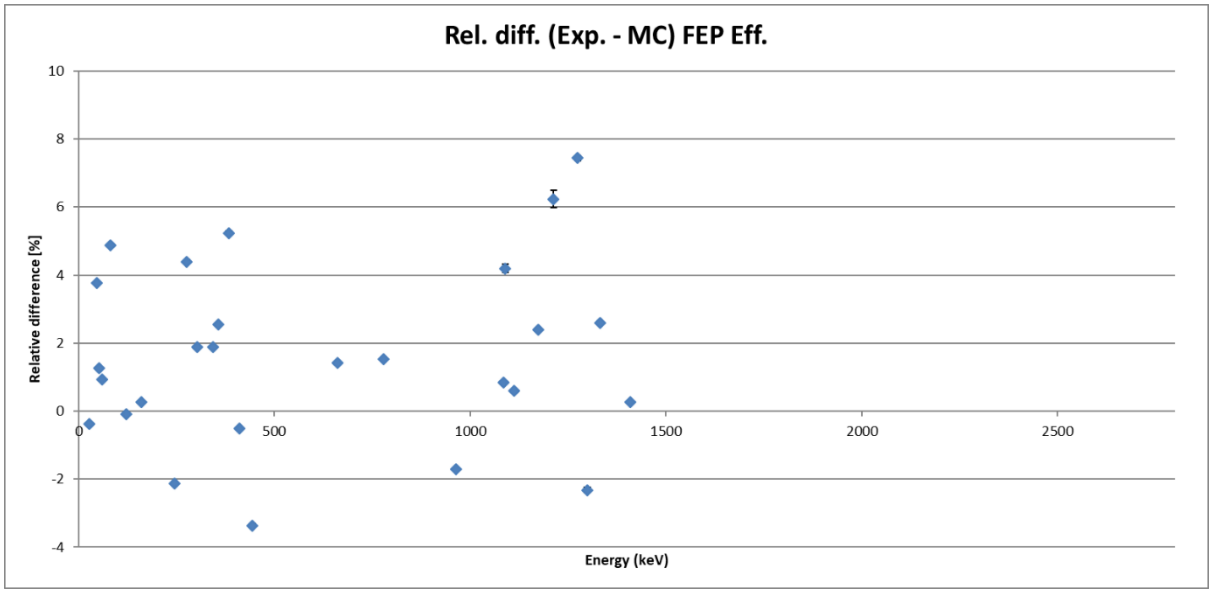

FINAL MODEL
Crystal distance: -0.15 cm Top Deadlayer: 0.4 um Side Deadlayer: 0.1 cm
Endcap: 0.15 cm

Mean dev.	0.50%	Mean dev.	-0.46%	Mean dev.	2.01%
Stdev of dev.	2.64%	Stdev of dev.	2.88%	Stdev of dev.	1.38%

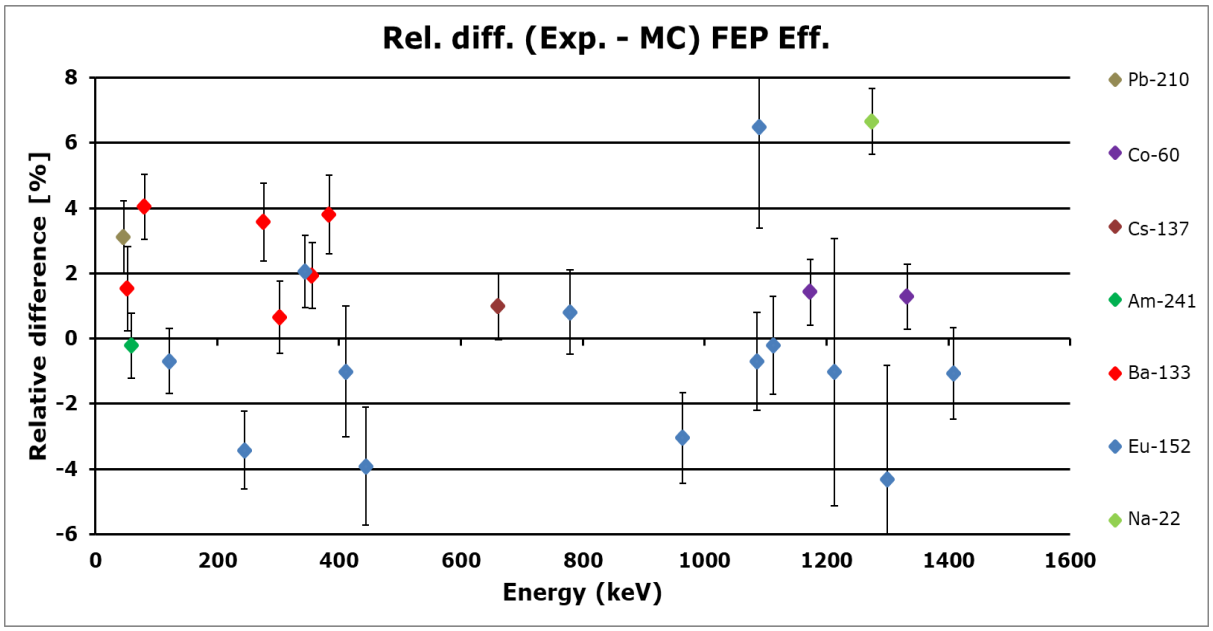

Validation: change in distance: 133 + 134 + 110 (10 cm)

Original Model
Crystal distance: 0 cm Top Deadlayer: 0.4 um Side Deadlayer: 0.05 cm

Mean dev.	-5.63%	Mean dev.	-6.82%	Mean dev.	-4.26%
Stdev of dev.	2.28%	Stdev of dev.	1.19%	Stdev of dev.	2.43%

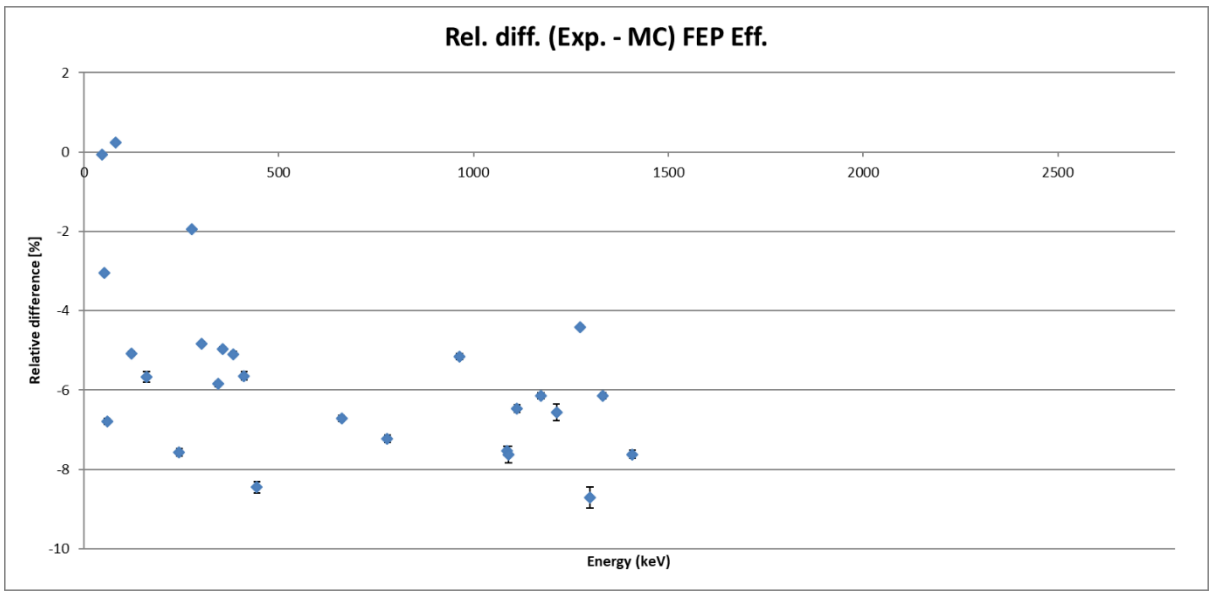

Crystal distance: -0.18 cm Top Deadlayer: 0.4 um Side Deadlayer: 0.05 cm

Mean dev.	-3.58%	Mean dev.	-4.82%	Mean dev.	-2.35%
Stdev of dev.	2.40%	Stdev of dev.	1.60%	Stdev of dev.	2.56%

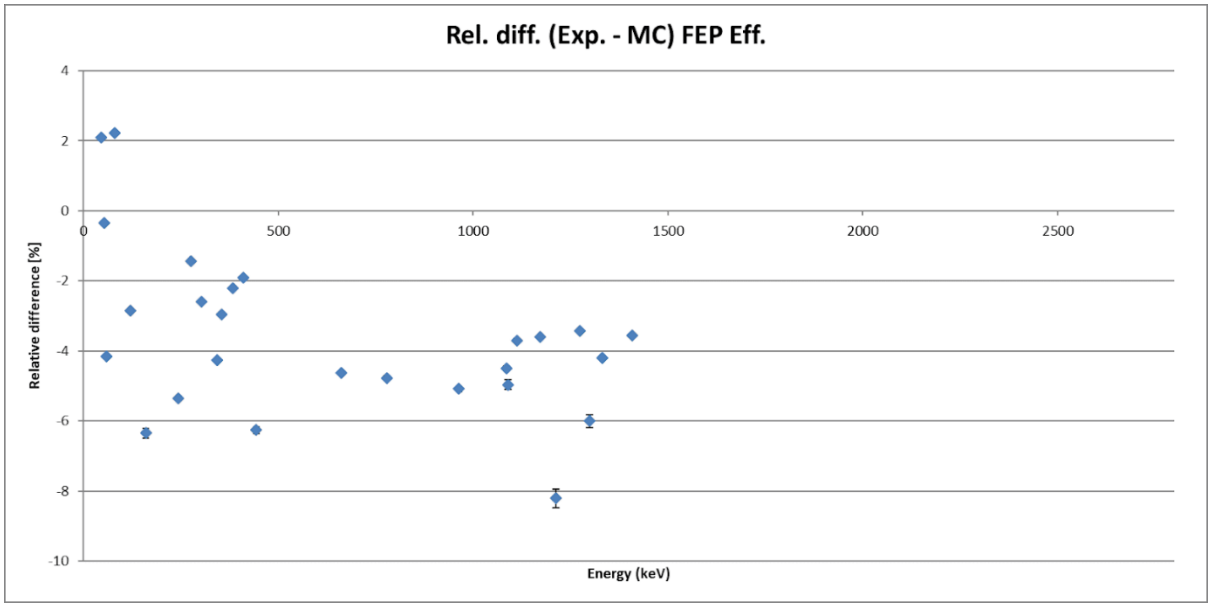

Crystal distance: -0.2 cm Top Deadlayer: 0.4 um Side Deadlayer: 0.05 cm

Mean dev.	-2.80%	Mean dev.	-3.58%	Mean dev.	-1.87%
Stdev of dev.	2.14%	Stdev of dev.	1.37%	Stdev of dev.	2.47%

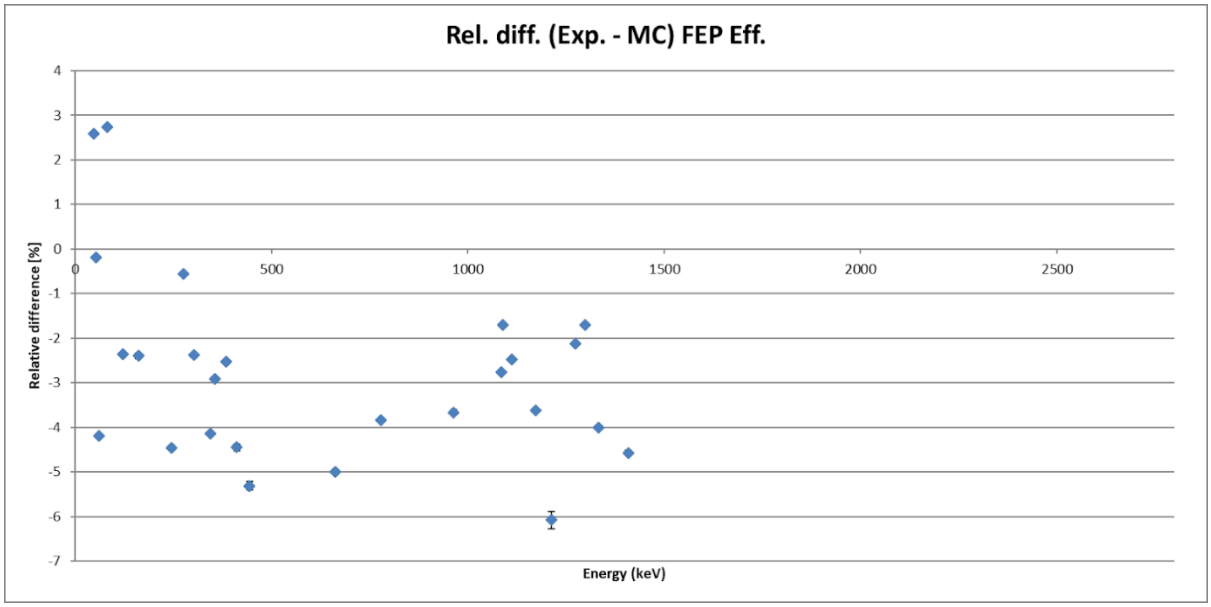

Crystal distance: -0.15 cm Top Deadlayer: 0.4 um Side Deadlayer: 0.1 cm

Mean dev.	-0.10%	Mean dev.	-0.72%	Mean dev.	-0.93%
Stdev of dev.	2.07%	Stdev of dev.	1.42%	Stdev of dev.	2.38%

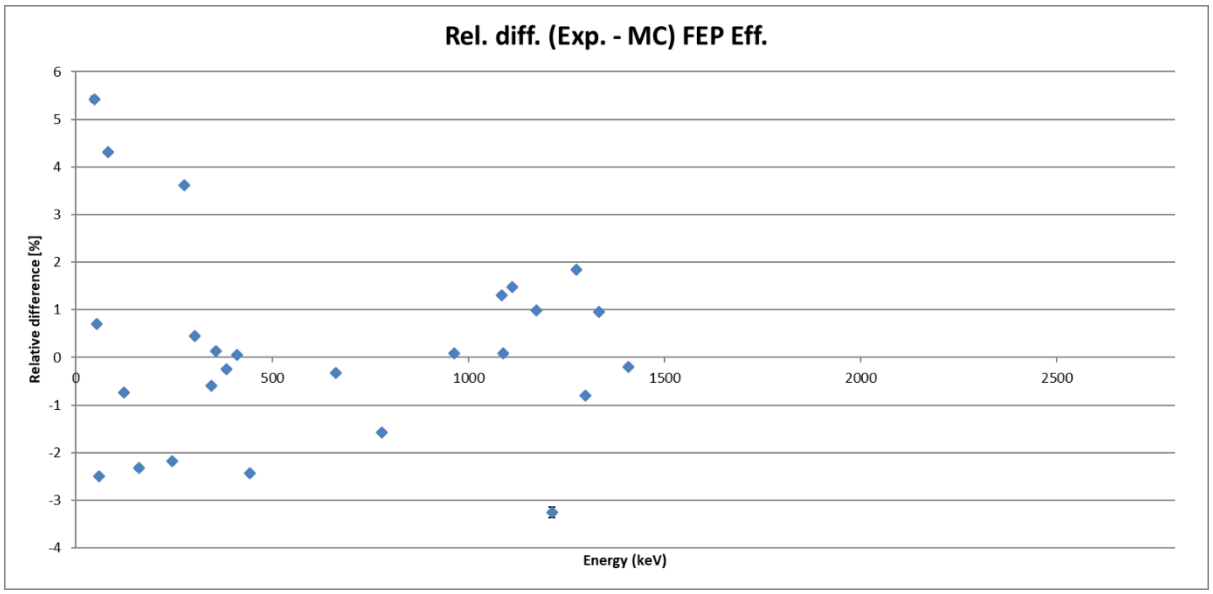

Crystal distance: -0.18 cm Top Deadlayer: 0.4 um Side Deadlayer: 0.1 cm

Mean dev.	0.91%	Mean dev.	0.65%	Mean dev.	1.12%
Stdev of dev.	2.15%	Stdev of dev.	1.81%	Stdev of dev.	2.53%

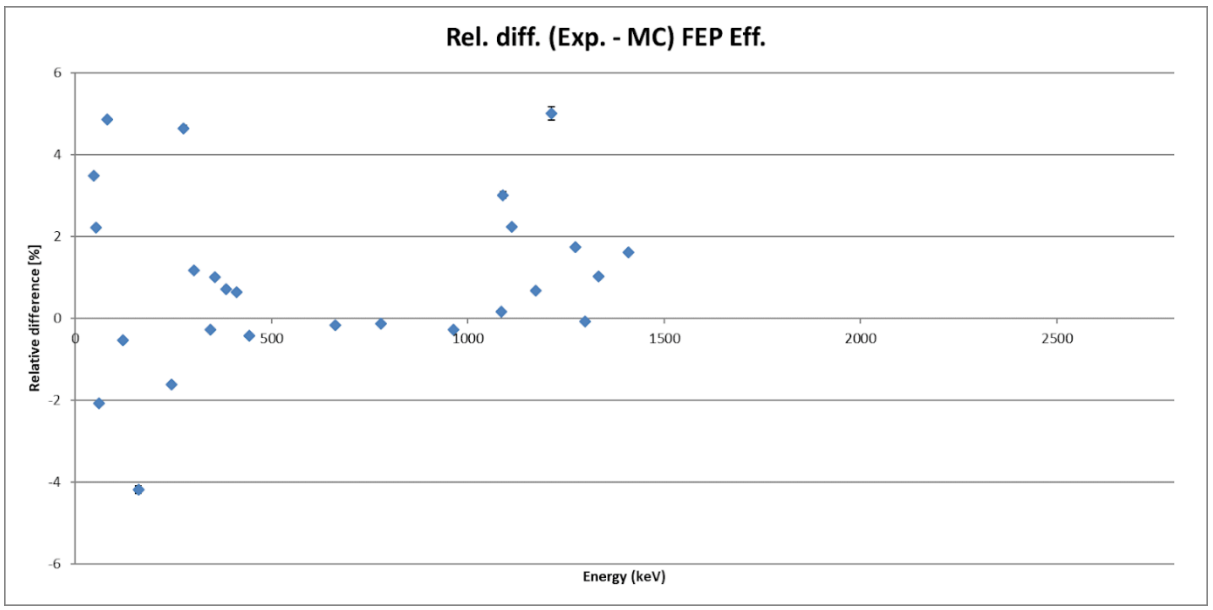

FINAL MODEL
Crystal distance: -0.15 cm Top Deadlayer: 0.4 um Side Deadlayer: 0.1 cm
Endcap: 0.15 cm

Mean dev.	-0.29%	Mean dev.	-0.92%	Mean dev.	0.49%
Stdev of dev.	1.49%	Stdev of dev.	1.34%	Stdev of dev.	1.37%

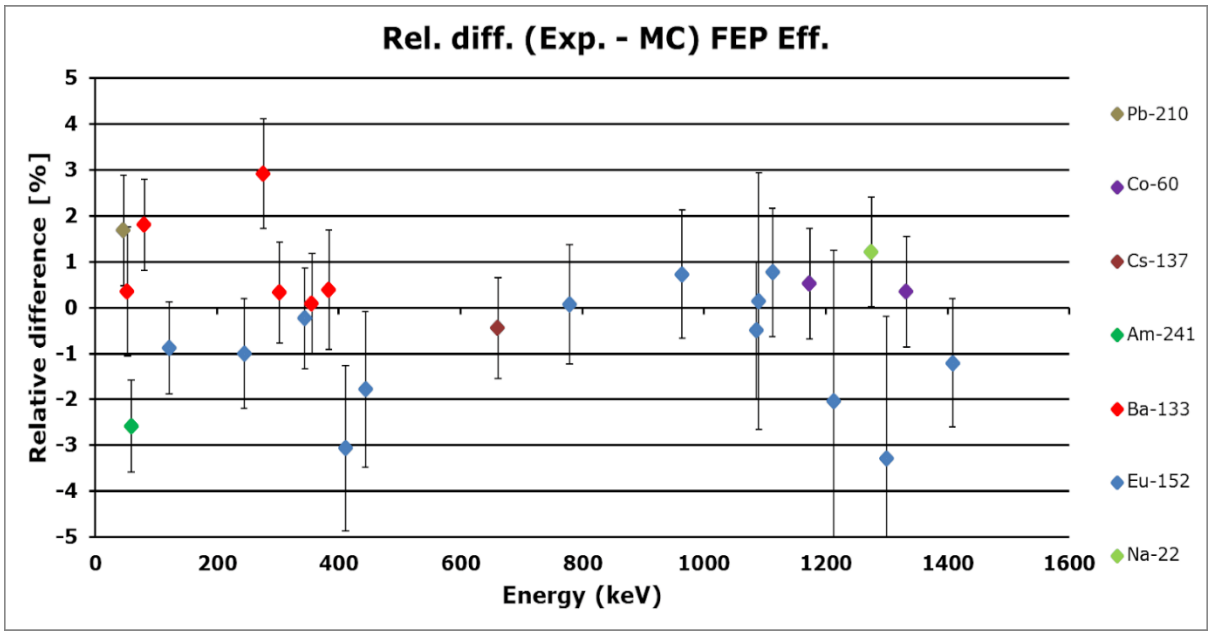

Validation: Volume sources

CMI-3

Mean dev. 1.40%
Stdev of dev. 2.32%

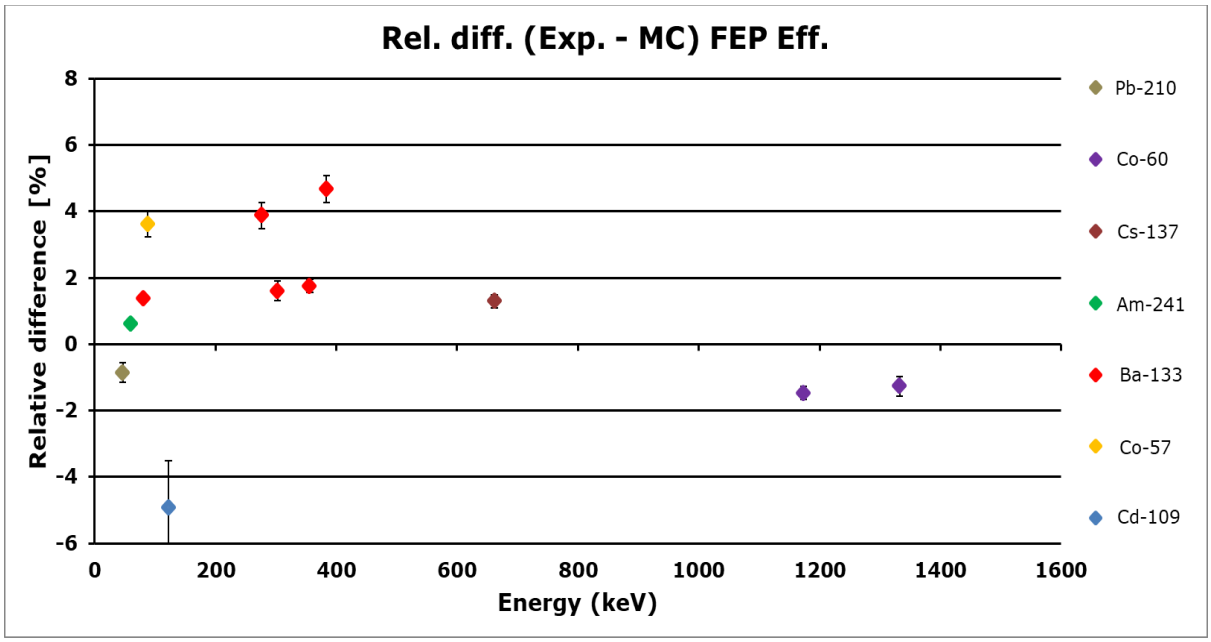

CMI-14

Mean dev. 1.09%
Stdev of dev. 3.63%

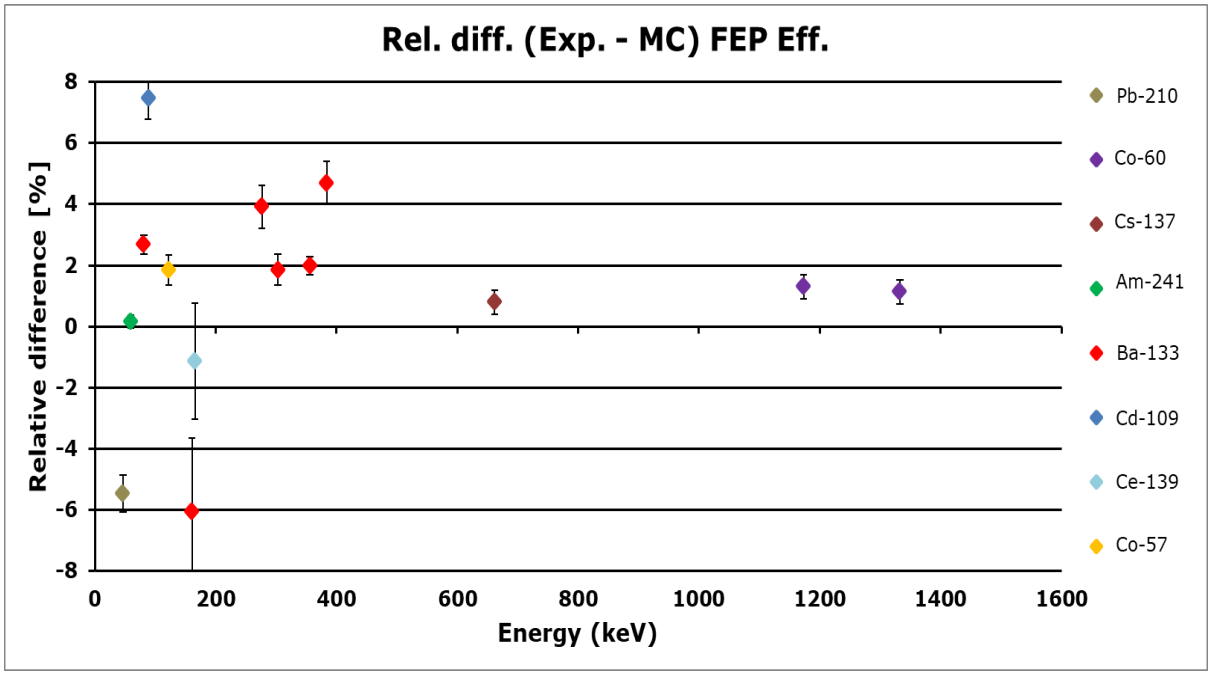

CMI-15

Mean dev. 0.42%
Stdev of dev. 3.15%

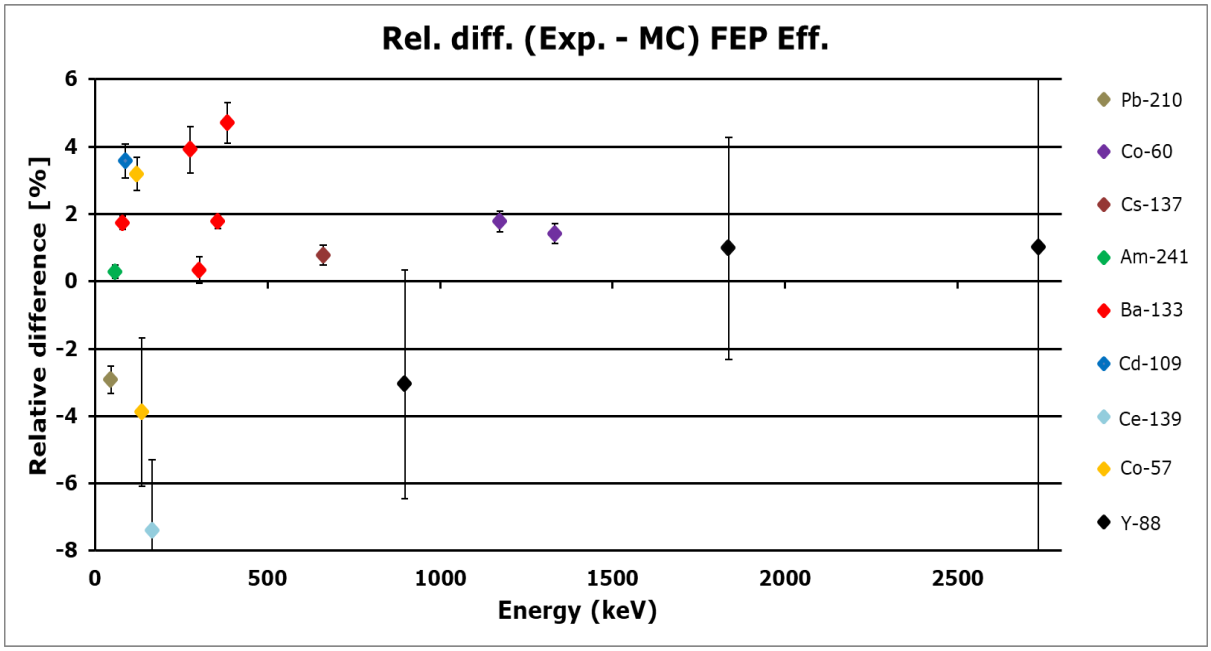

CMI-8

Mean dev. 0.11%

Stdev of dev. 1.64%

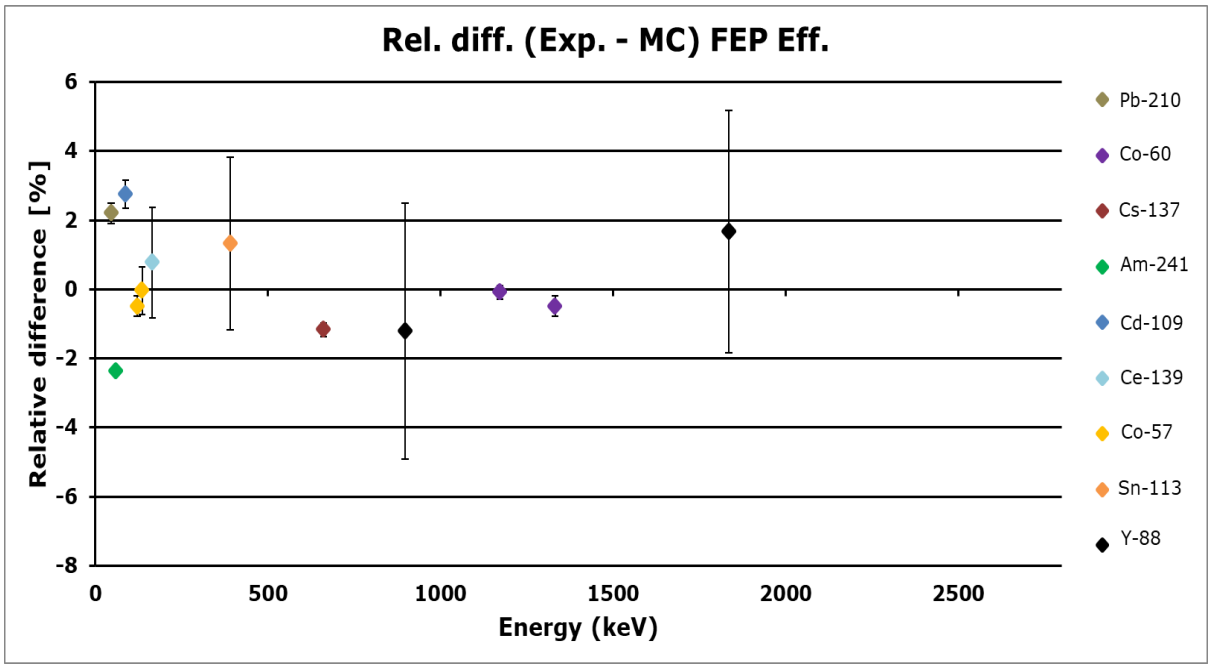

Appendix B: Relative efficiency difference graphs of Ge14

Original Model

<u>Crystal distance:</u> 0 cm <u>Outer deadlayer:</u> 0.05 cm <u>Well-Deadlayer:</u> 0.006 cm

Mean dev. -3.12%
Stdev of dev. 5.24%

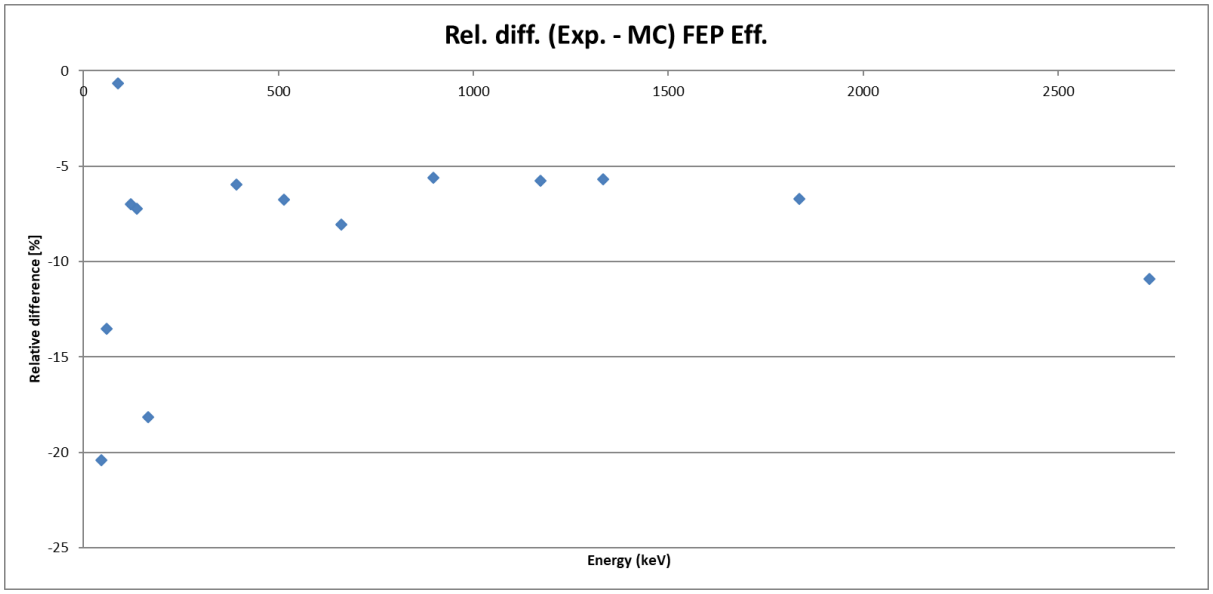

Change in crystal position

<u>Crystal distance:</u> -0.05 cm <u>Outer deadlayer:</u> 0.05 cm <u>Well-Deadlayer:</u> 0.006 cm

Mean dev. -7.82%
Stdev of dev. 4.24%

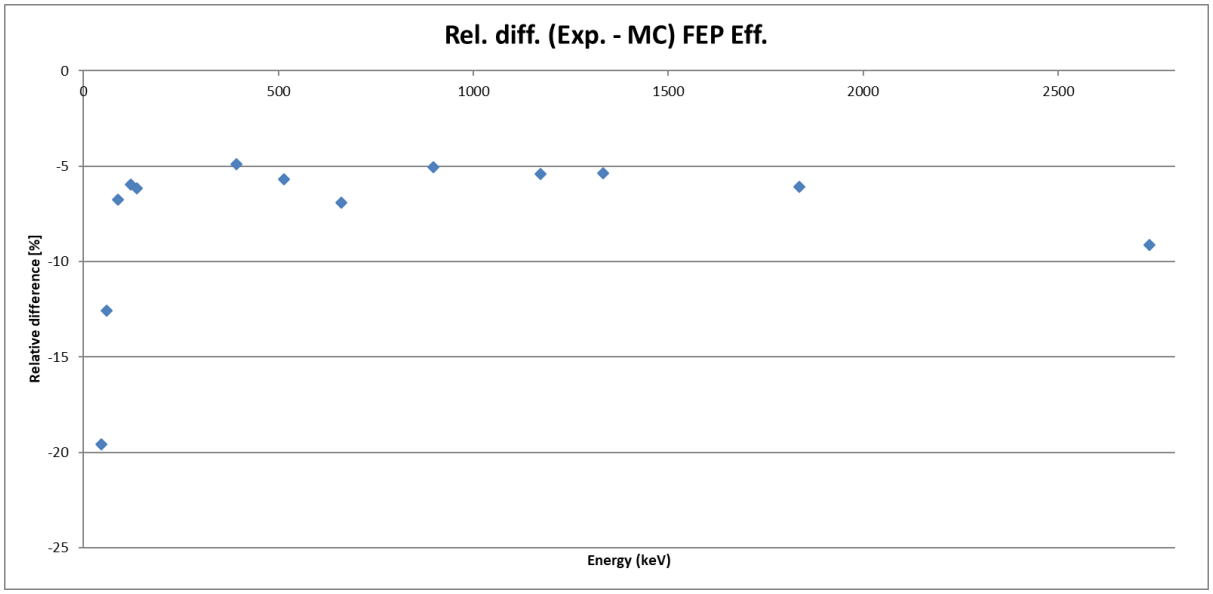

Crystal distance: -0.1 cm Outer deadlayer: 0.05 cm Well-Deadlayer: 0.006 cm

Mean dev. -7.32%
Stdev of dev. 4.14%

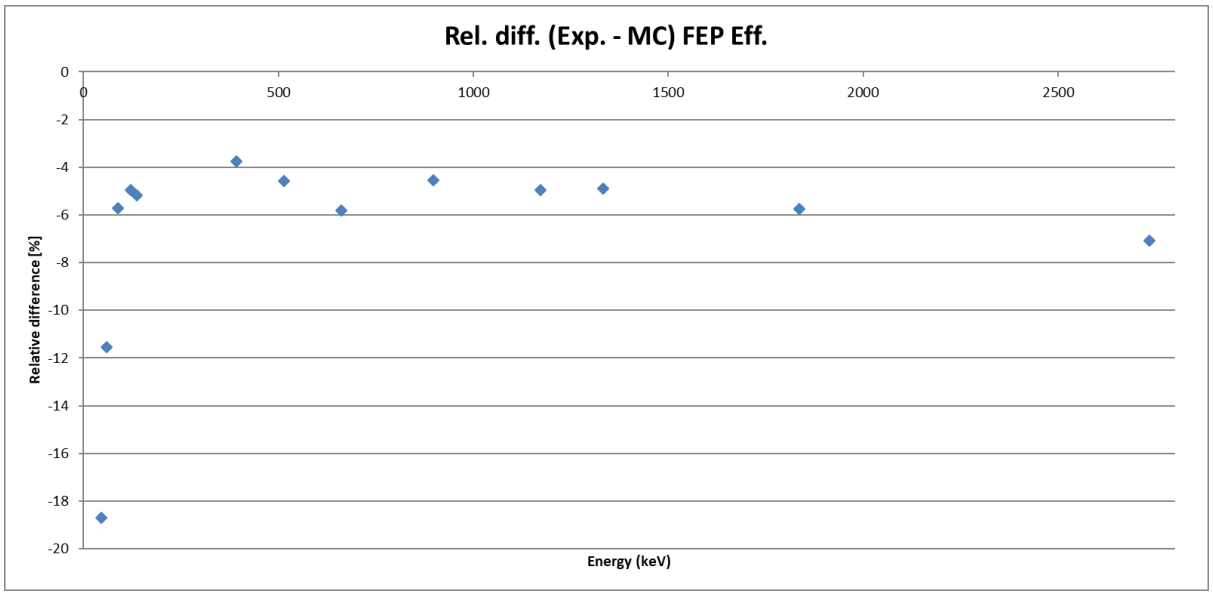

Crystal distance: -0.3 cm Outer deadlayer: 0.05 cm Well-Deadlayer: 0.006 cm

Mean dev. -3.64%
Stdev of dev. 4.89%

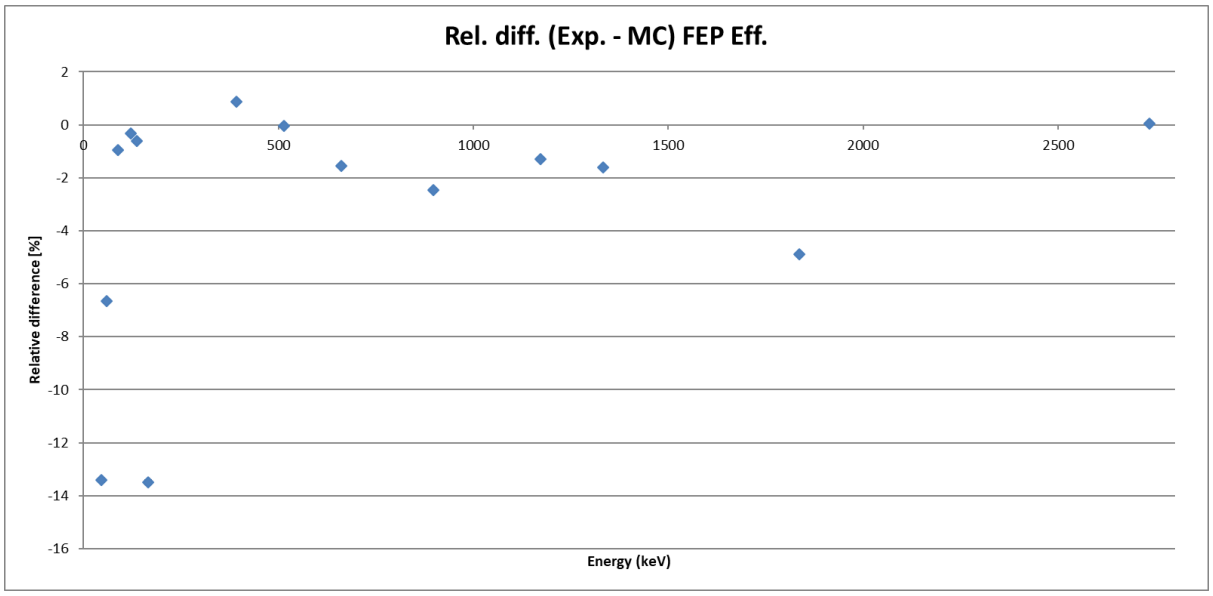

Crystal distance: -0.5 cm Outer deadlayer: 0.05 cm Well-Deadlayer: 0.006 cm

Mean dev. -0.22%
Stdev of dev. 5.01%

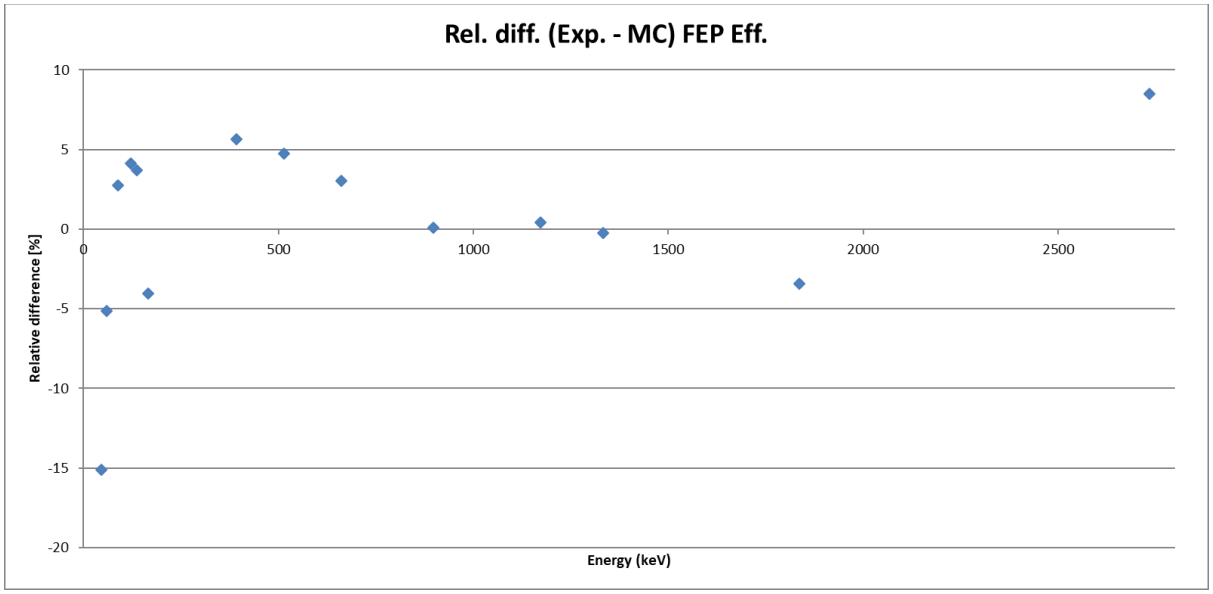

Change Well-Deadlayer

Crystal distance: 0 cm Outer deadlayer: 0.05 cm Well-Deadlayer: 0.012 cm

Mean dev. -5.41%
Stdev of dev. 1.14%

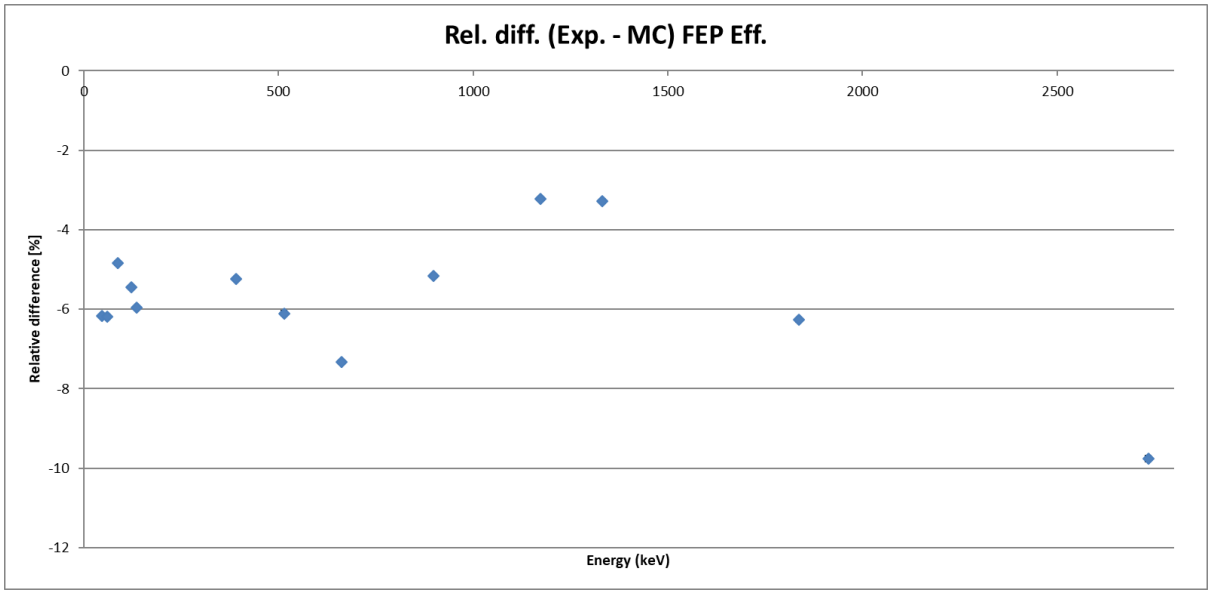

Crystal distance: 0 cm **Outer deadlayer:** 0.05 cm **Well-Deadlayer:** 0.050 cm

Mean dev. -34.41%
Stdev of dev. 41.14%

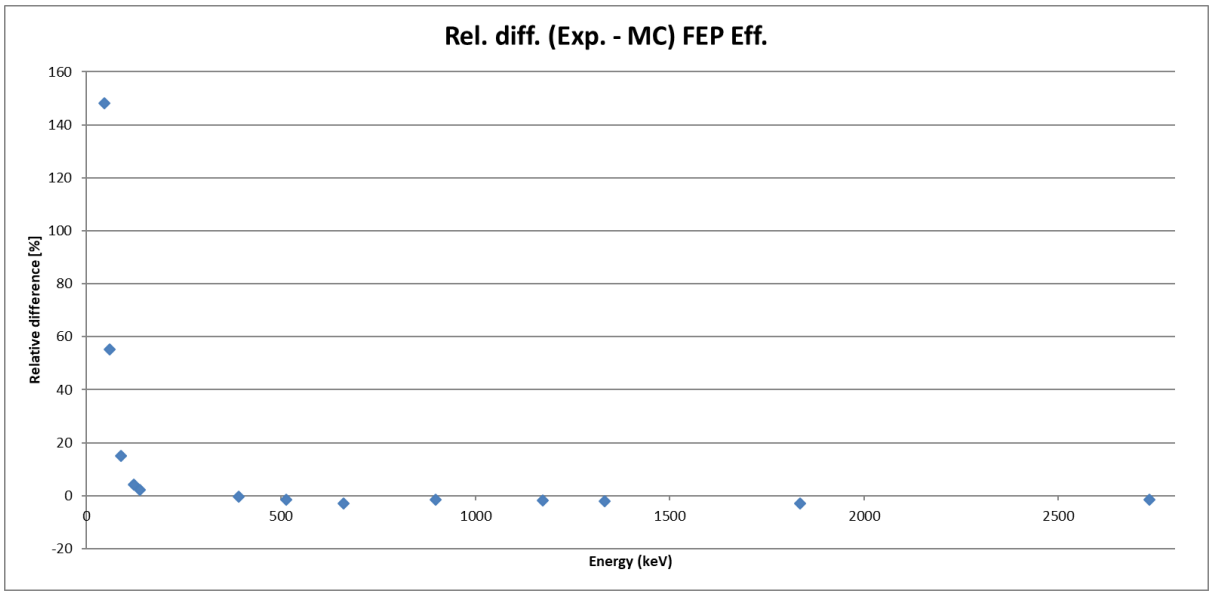

Combination

Change Well-Deadlayer and crystal position

Crystal position: -0.25 cm **Outer deadlayer:** 0.05 cm **Well-Deadlayer:** 0.012 cm

Mean dev. 0.59%
Stdev of dev. 1.34%

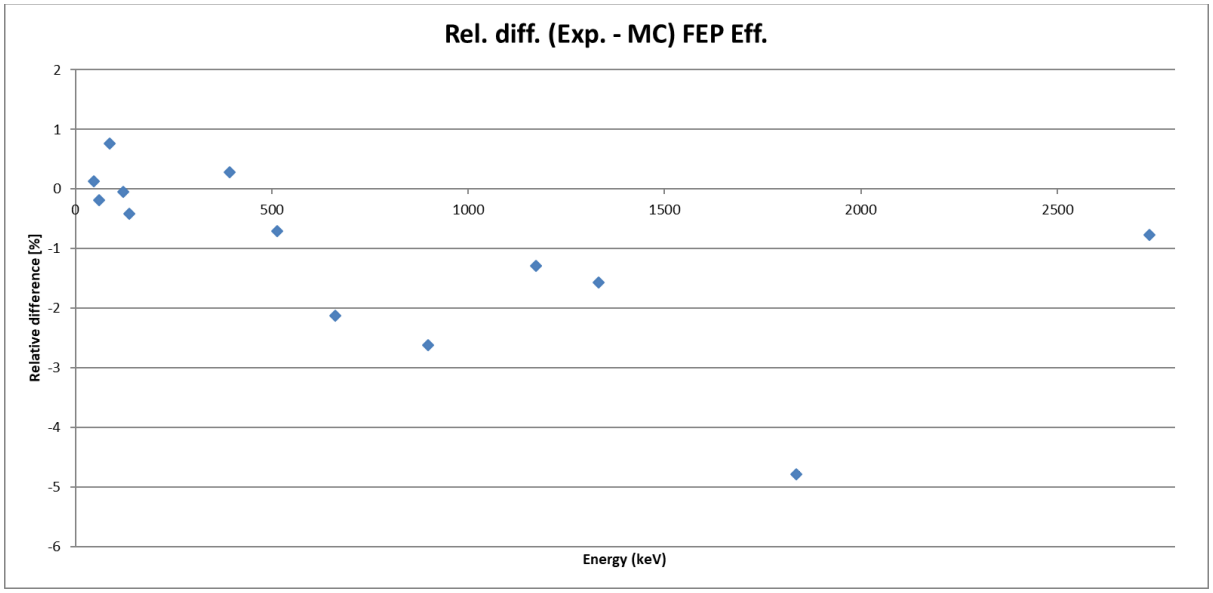

Combination
Change Well-Deadlayer and Outer deadlayer
<u>Crystal distance:</u> 0 cm <u>Outer deadlayer:</u> 0.15 cm <u>Well-Deadlayer:</u> 0.012 cm

Mean dev. -0.22%
Stdev of dev. 3.53%

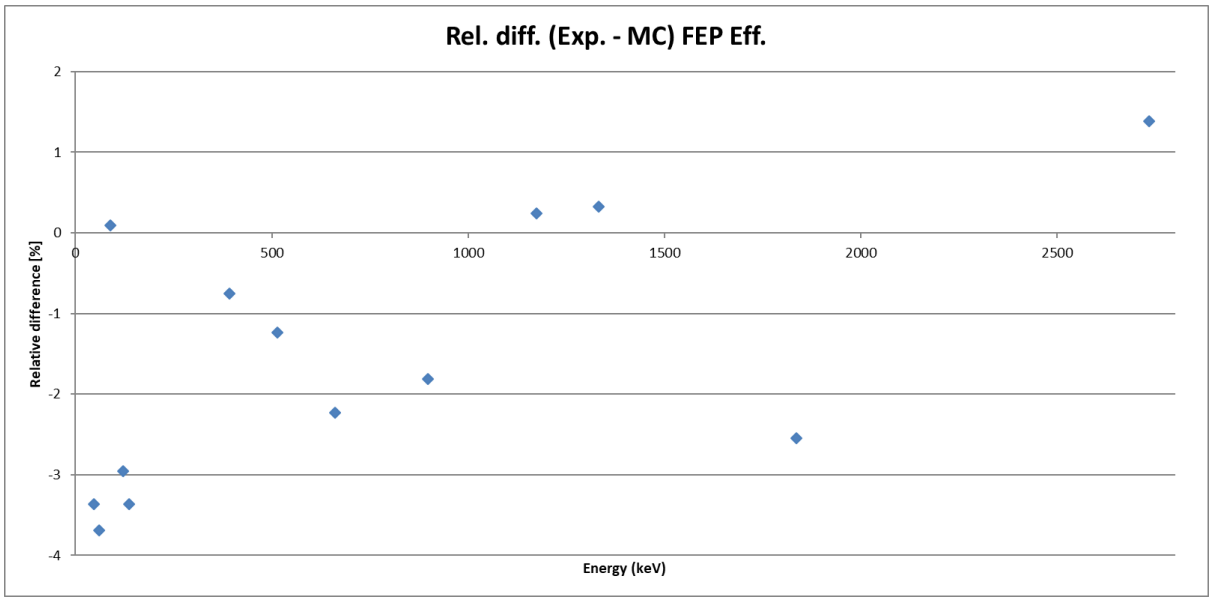

<u>Crystal distance:</u> 0 cm <u>Outer deadlayer:</u> 0.15 cm <u>Well-Deadlayer:</u> 0.015 cm

Mean dev. -0.83%
Stdev of dev. 1.53%

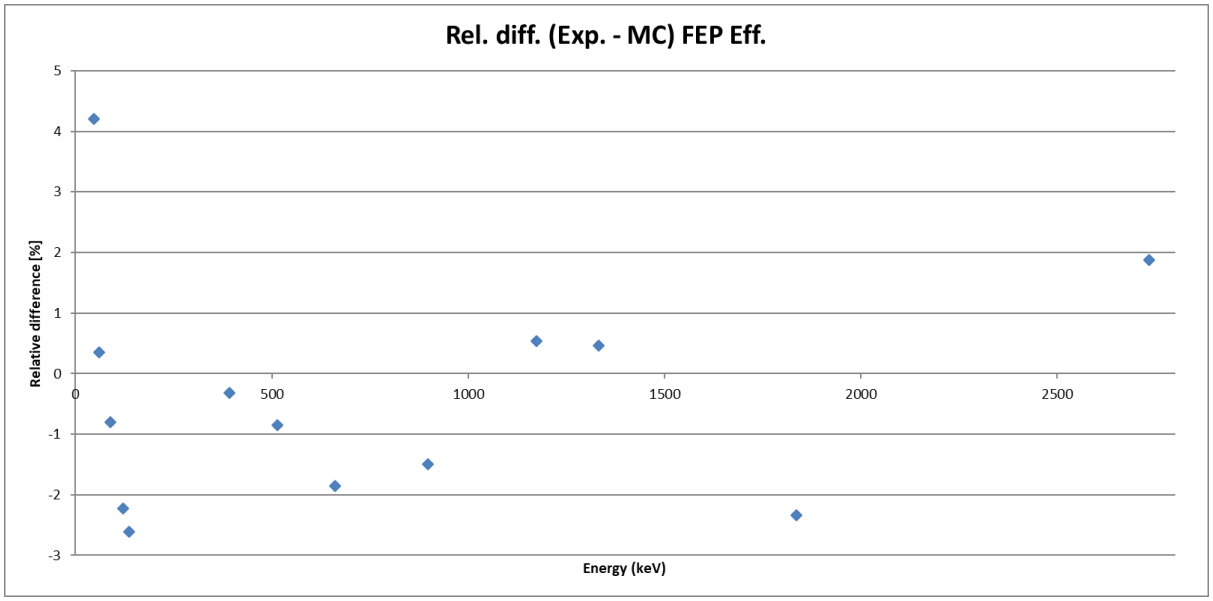

Crystal distance: 0 cm **Outer deadlayer:** 0.17 cm **Well-Deadlayer:** 0.014 cm

Mean dev. -0.71%
Stdev of dev. 1.31%

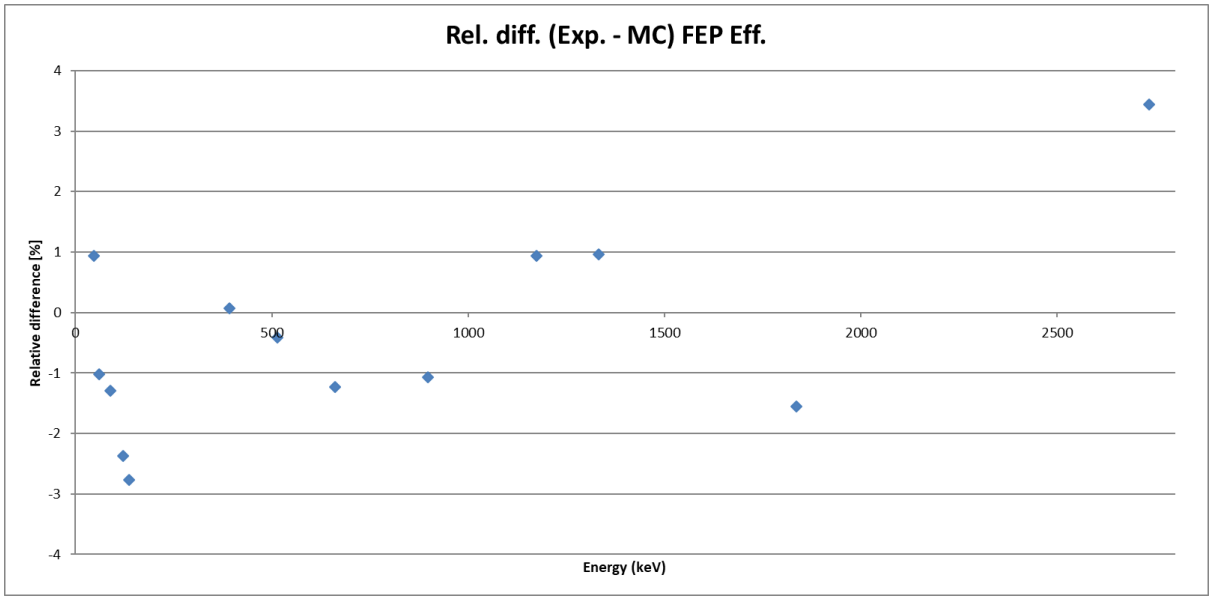

Combination
Change Well-Deadlayer and Outer deadlayer and crystal position

Crystal position: -0.25 cm **Outer deadlayer:** 0.07 cm **Well-Deadlayer:** 0.004 cm

Mean dev. -5.23%
Stdev of dev. 5.13%

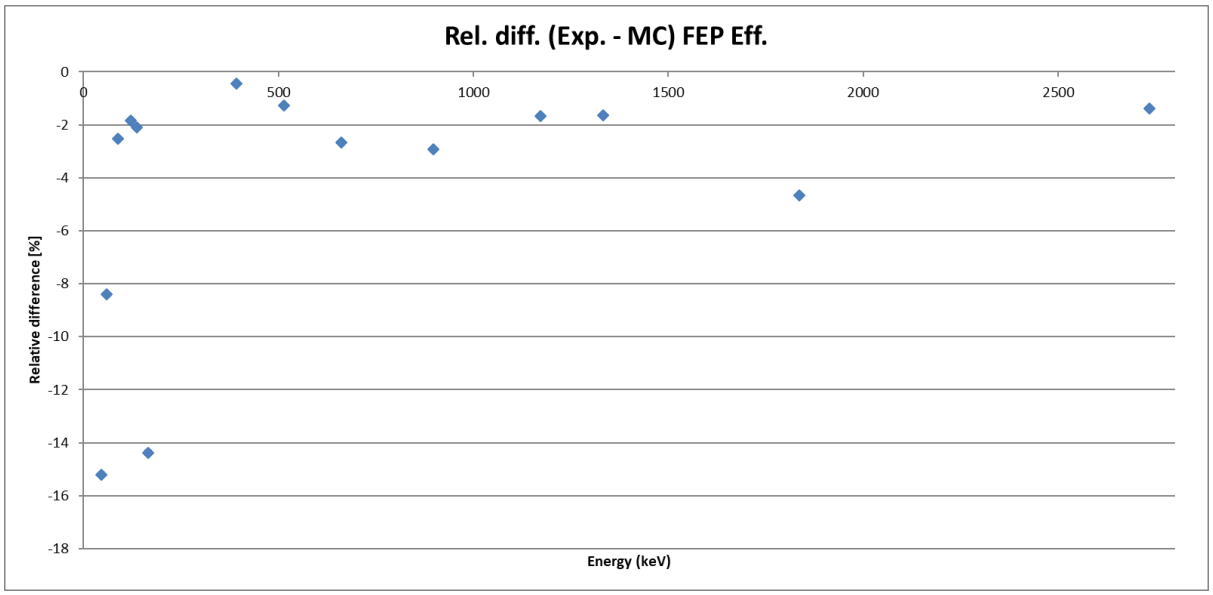

Crystal position: -0.25 cm Outer deadlayer: 0.1 cm Well-Deadlayer: 0.012 cm

Mean dev. -0.83%
Stdev of dev. 1.63%

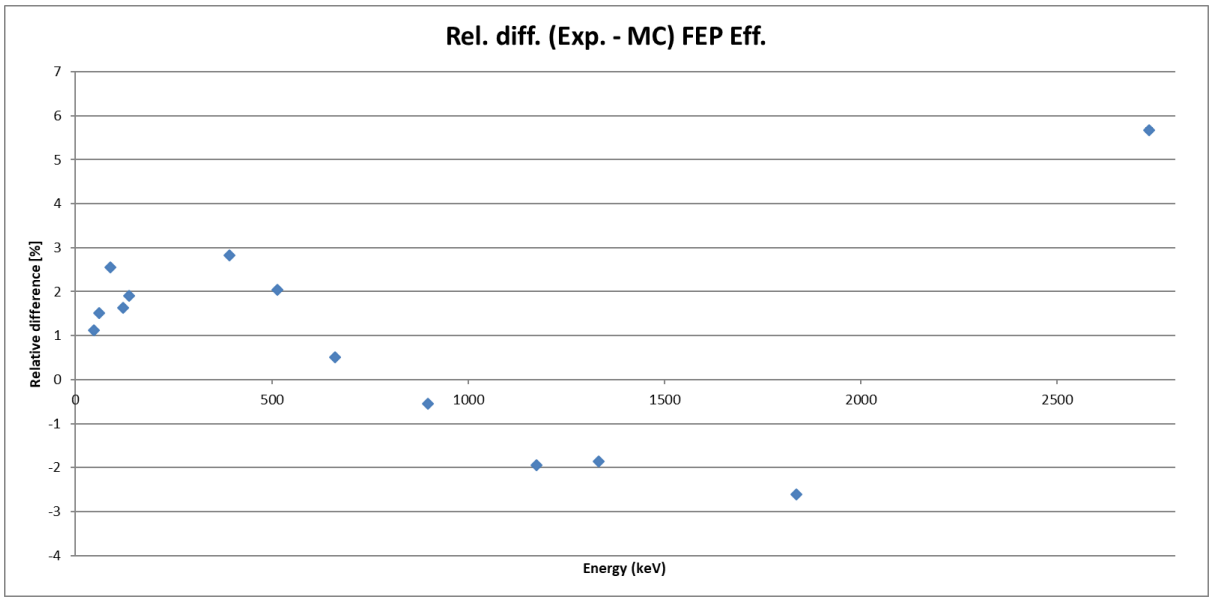

Crystal position: -0.25 cm Outer deadlayer: 0.08 cm Well-Deadlayer: 0.012 cm

Mean dev. -0.22%
Stdev of dev. 1.13%

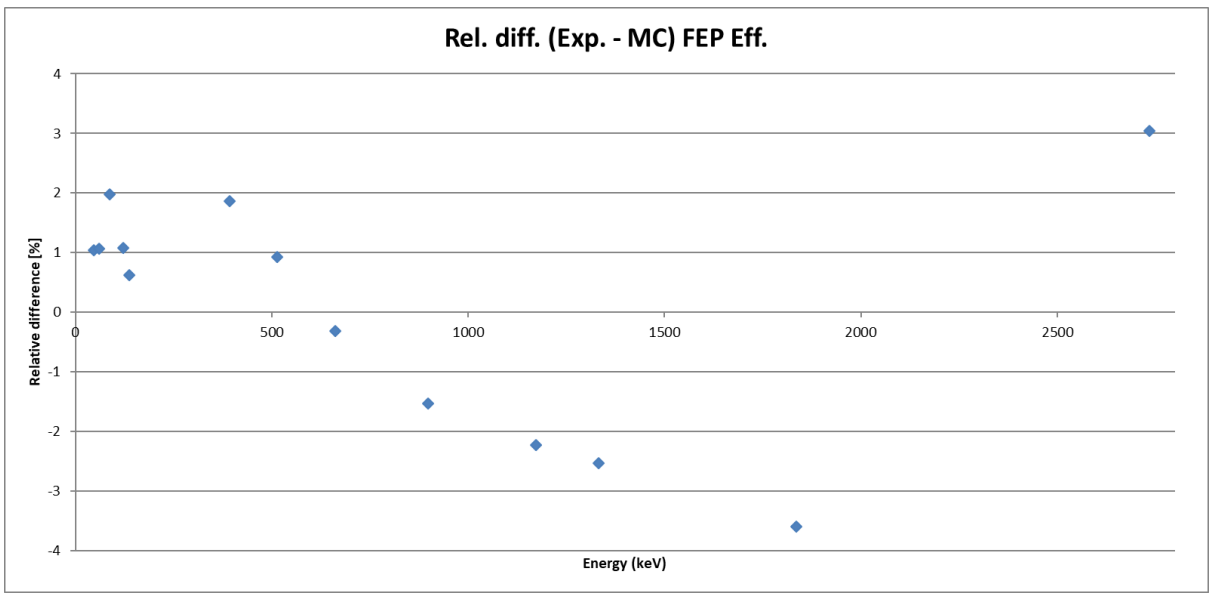

Crystal position: **-0.25 cm** **Outer deadlayer:** **0.08 cm** **Top deadlayer:** **0.05cm** **Well-Deadlayer:** **0.012 cm**

Mean dev. -1.11%
Stdev of dev. 1.43%

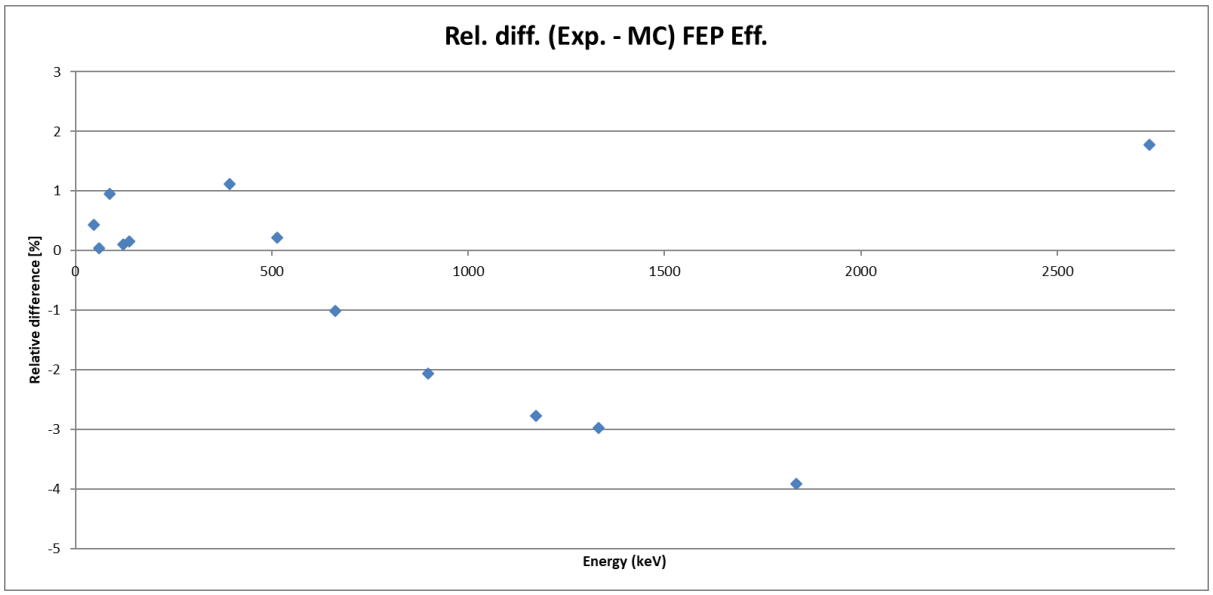

Crystal position: **-0.05 cm** **Outer deadlayer:** **0.17 cm** **Well-Deadlayer:** **0.014 cm**

Mean dev. -0.22%
Stdev of dev. 1.03%

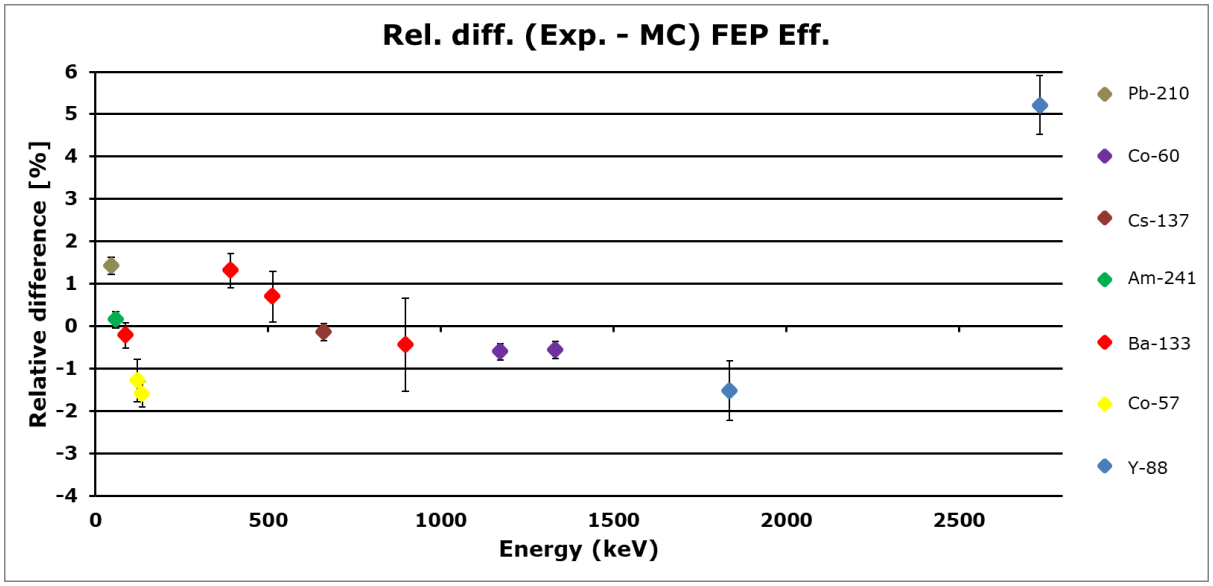

Validation: Volume sources

CMI4

Outer deadlayer: 0.17 cm Well-Deadlayer: 0.014 cm

Mean dev. -1.32%
Stdev of dev. 1.23%

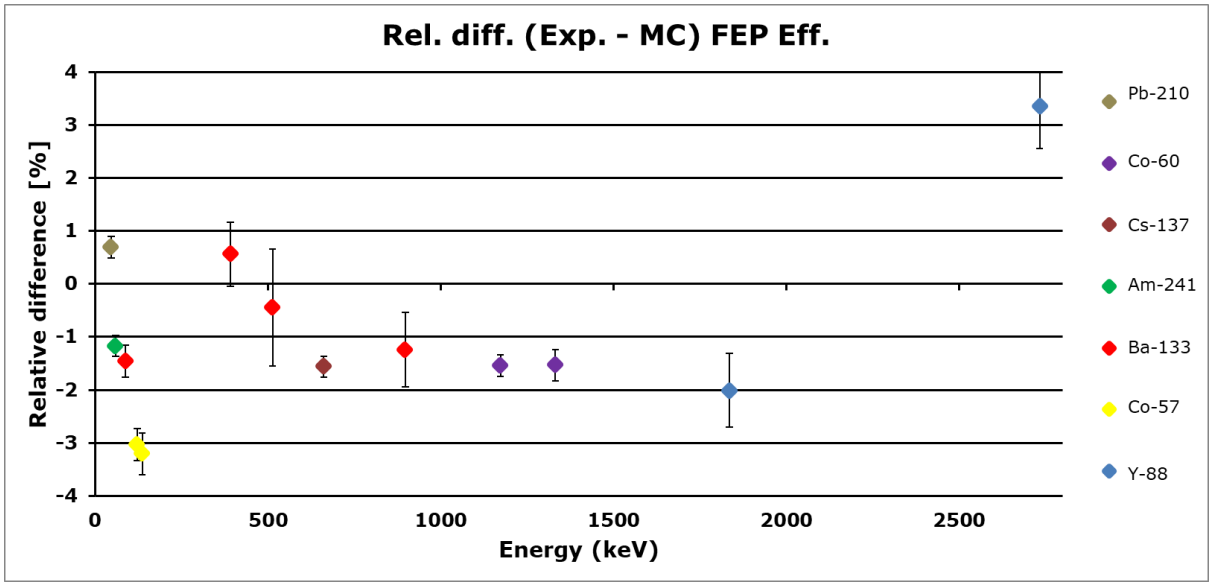

Final Model (CMI4)

Crystal position: -0.05 cm Outer deadlayer: 0.17 cm Well-Deadlayer: 0.014 cm

Mean dev. -0.42%
Stdev of dev. 1.30%

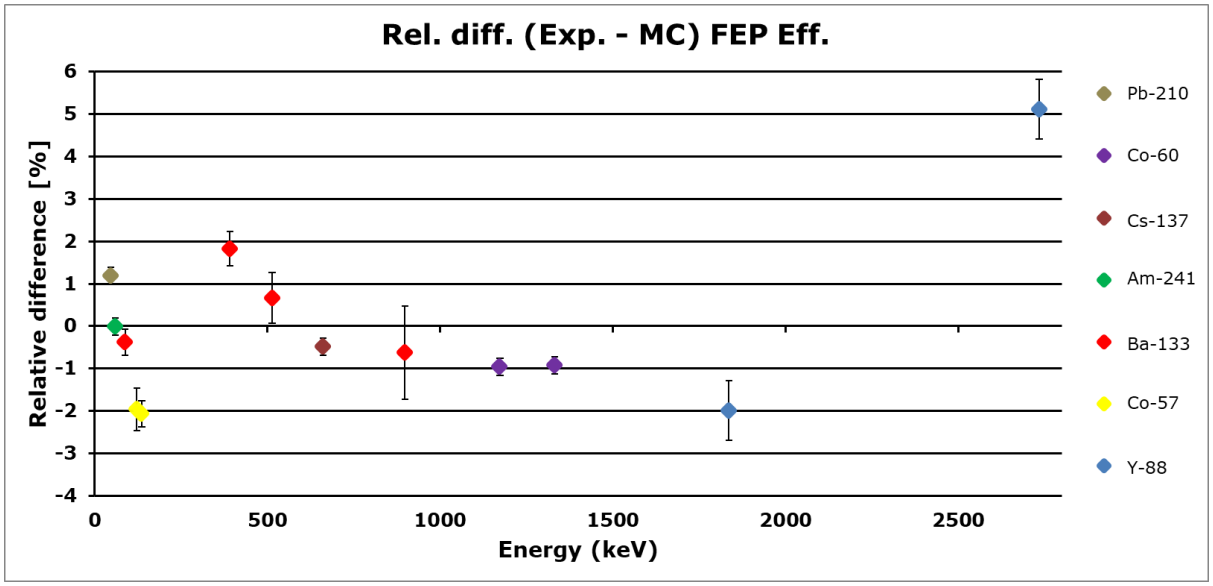

Final Model (CMI5, adaptation after validation)

<u>Crystal position:</u> -0.05 cm <u>Outer deadlayer:</u> 0.17 cm <u>Well-Deadlayer:</u> 0.014 cm

Mean dev. -0.22%
Stdev of dev. 1.05%